MSc-thesis

Characterizing coastal wind speed gradients using Scanning LiDAR data and mesoscale modeling

Haolin Liu

TU Delft & NUON/Vattenfall

TU Delft

MSc-thesis

by

Haolin Liu

to obtain the degree of Master of Science
at the Delft University of Technology,

Student number:	4892526	
Project duration:	Oct 1, 2019 – Aug 1, 2020	
Thesis committee:	Dr. Sukanta Basu,	TU Delft, supervisor
	Prof.dr.ir. B.J.H. (Bas) van de Wiel	TU Delft
	Prof. Simon Watson	TU Delft
	Jan Borràs Morales,	Vattenfall, supervisor

To be defended in public on Sep 18th 2020

TU Delft

Abstract

This research attempts to investigate the coastal flow structure horizontally. The flow cases with different flow directions, including perpendicular and parallel to the shoreline directions, are selected by analyzing the New Europe Wind Atlas (NEWA) reanalysis data. After the cases are determined, high-resolution Weather Research and Forecasting Model (WRF) are performed under Yonsei University (YSU) Planetary Boundary Layer (PBL) scheme with ERA5 forcing data. The results are validated against the measurements from long-range wind scanner WindCube 400S. The validated data is analyzed for quantifying the orthogonal wind speed gradient over the study domain.

As a result, the WRF, being a mesoscale modelling tool, it captures the orthogonal coastal wind speed gradients reasonably accurate within a 6km range compared with observations. Generally, WRF performs better in the alongshore flow cases, especially in the flow case 2018-10-08 when the stable condition occurs most frequently during the case. The Root Mean Square Error (RMSE) for this case is 0.9m/s. However, the simulation results lost correlations with the observational data in some epochs when the fluctuation of wind speed occurs frequently. To be concrete, during flow case 2018-12-10 when the flow direction is around 330° advecting onshore, the WRF simulation can predict the fluctuations correct in magnitude but with shifting in time.

For the coastal wind speed gradient, WRF predicts an absolute wind speed difference of 0.5 m/s daily averaged at the typical hub height over a 1.4km distance for the alongshore flow cases. This difference can enlarge to 1m/s or higher while the low-level jets take place. The long-range wind scanning LiDAR provides a great possibility for observing the flow condition over a wind farm sized domain. Especially for the nearshore wind farm, it compensates for lack of observations on the water.

Acknowledgement

First of all, I would like to express my deep and sincere gratitude to Sukanta Basu for supervising me with my MSc-thesis study throughout the year. My interests in atmospheric science and meteorology started from taking your creative lecture. Your frequently organized group meeting allows me to acquaint many excellent peers and to learn from them. Your patient guidance and constant encouragement to me is sincerely appreciated. I also want to deeply thank Jan Coelingh and Jan Borràs Morales for offering me the opportunity to work on the thesis with Vattenfall company. You provided me with not only valuable data and technical supports but also a comfortable working environment with adorable colleagues. I am grateful to meet you all and other partners in the office, for many friendly accompany during coffee and lunch breaks. I would also like to thank my committee for your participation, valuable comments, and assessment for my MSc-thesis study. Moreover, I want to thank Erwin de Beus for the technical support regarding Vrlab, which provides me with powerful computational support, your fast respond and detailed operating manul of the Vrlab machine is much appreciated.

I am extremely grateful to my parents for their love, caring, supporting, educating and preparing me for my future. Thanks to my fellows from the environmental science track for selfless accompanying and supporting during my maser study. Lastly, I want to thank my girlfriend for taking care of each other throughout the whole master journey, these moments we spent together in a foreign country will always be precious to me.

Haolin Liu
Delft, June 2020

Contents

List of Abbreviations

DOWA DUTCH OFFSHORE WIND ATLAS

ECMWF European Centre for Medium-Range Weather Forecasts

FLLJ Frontal Low Level Jet

FLS Floating LiDAR system

IBL Internal Boundary Layer

KAMM Karlsruhe Atmospheric Mesoscale Model

LES Large Eddy Simulation

LiDAR Light Detection and Ranging

LLJ Low Level Jet

MRF Medium-Range Forecast

MYJ Mellor-Yamada-Janjic

MYNN2 Mellor-Yamada-Nakanishi-Niino

NEWA NEW EUROPEAN WIND ATLAS

NWP Numerical weather prediction

PBL Planetary Boundary Layer

PPI Plan position indicators

RMSE Root Mean Square Error

SAR Synthetic-aperture radar

SCADAR Scanning system based LiDAR

TKE Turbulent kinetic energy

WAsP Wind Atlas Analysis and Application Program

WRF Weather Reasearch and Forcasting

YSU Yonsei University

1

Introduction

The global temperature has been rising at an average rate of (0.18 °C / 0.32 °F) per decade since 1981 in the combination of land and ocean [for Environmental Information, 2019]. The extensive usage of fossil fuel is one of the major human activities that primarily contribute to worldwide CO2 emissions, and in turn, the rising of global temperature. This rising global temperature is very likely to cause significant changes to global patterns such as precipitation distribution, extreme weather, as well as the melting of ice on the polar regions [Blunden et al., 2018]. These changes not only continuously affect our ecology by causing species

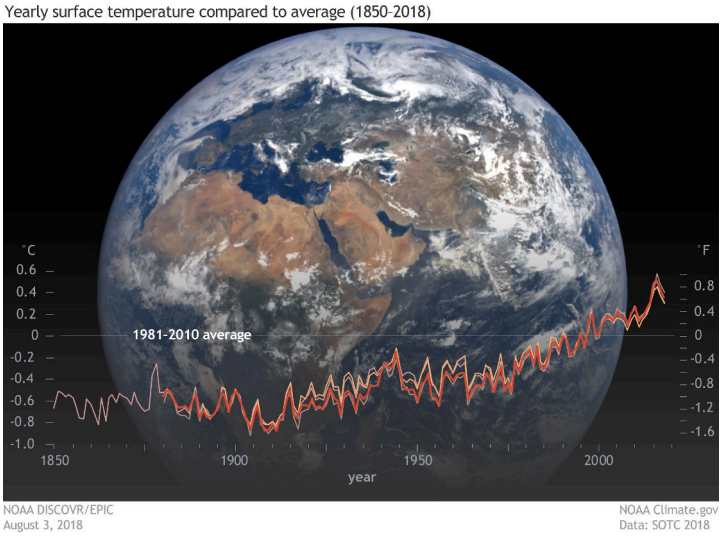

Figure 1.1: History of global temperature from four research organizations: NOAA (red), NASA (tan), University of east Anglia (pink), and the Japan Meteorological Agency (orange). The back ground is from NOAA's DSCOVER satellite on August 3, 2018.[Lindsey and Dahlman, 2020]

extinction and environmental degradation but also seriously threaten the safety of people 's lives and properties in coastal areas. Therefore, many authorities have started taking measures to minimize CO2 emissions by developing alternative renewable clean energy such as solar, wind, geothermal[Zuo and Liu, 2012]. Each of these technologies has its strengths and limitations. Producing energy using wind turbines can be a satisfying power generation source as it is environmentally friendly without any toxic gas release and also relatively little land area requirements. For the European energy market, a total wind power capacity of 15.4GW was reached in 2019, which accounted for 15% of the total electricity that EU-28 consumed in 2019 [WindEurope, 2019].

As the installation of wind turbines keep rising over the years, the power efficiency of each turbine is a critical consideration to make the investment more profitable. Therefore, the industries have been working on expanding the height and rotor size to enlarge the power production of a single wind turbine aiming at extracting the maximum wind energy via these turbines. Fig 1.2 [Ryan Wiser and Paulos, 2016] illustrates the

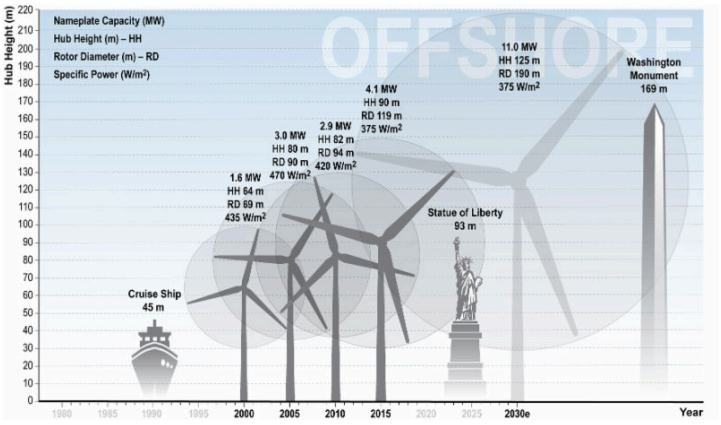

Figure 1.2: Growth in Offshore Turbine Size Globally [Ryan Wiser and Paulos, 2016]

growing trend of offshore wind turbine size and power generation, in terms of the hub height and the rotor diameter in the past decade. The rotor diameter doubled over fifteen years from 2000 to 2015, and its nameplate capacity also has grown more than twice fold from 1.6MW to 4.1MW. Studies, e.g.,[Enevoldsen and Xydis, 2019] have also analyzed extensive dataset on the wind turbine developments over recent decades (Fig1.3), a doubling of tower height and rotor diameters as well as eight times greater nameplate capacities has been revealed, and it is predicted to keep growing in height and size. Moreover, the scale of the wind farms is also expanding over the coastal region due to the rapidly decreasing cost of offshore wind power. It has recently reached $78/MWh in 2019, which is almost competitive with conventional power sources in terms of price [Lee, 2019].

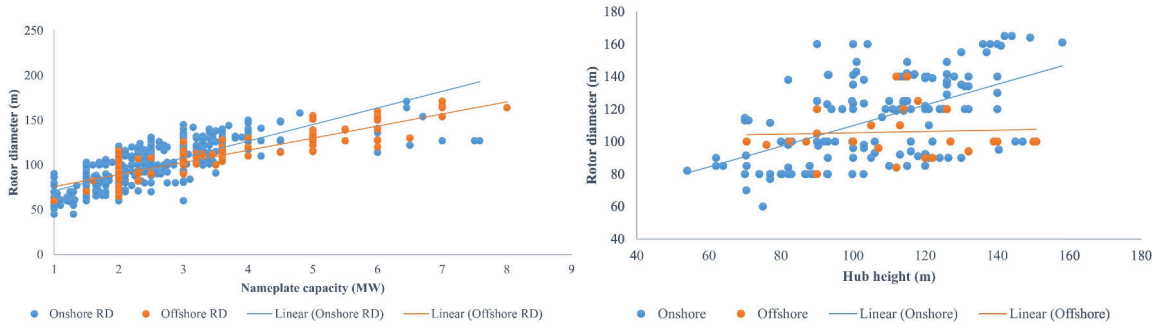

Figure 1.3: The development of hub height and nameplate capacity over time. [Enevoldsen and Xydis, 2019]

However, there will always exist a considerable amount of uncertainties as we are reaching higher layers of the atmosphere. There could be very localized phenomena occurring around the hub height, such as low-level jet, and the internal boundary layer, which significantly affects the energy production and fatigue load of wind turbines. Regarding those wind turbines constructed at a moderately short fetch from the coastline, the flow patterns are significantly affected both horizontally and vertically by the surface discontinuity at the land water interface depending on the atmospheric stability. Thus it is unrealistic to use the measurements from a few sites to represent the general flow condition among a wind farm located surrounding the coastal region.

In this research, several case studies will be carried on in order to obtain a better understanding of the flow structure both vertically and horizontally among the coastal regions. These cases thoroughly concentrate on a wind farm located on the southeast lake IJsselmeer the Netherlands. The determination of these flow cases is based on the wind direction sectors roughly described by the NEW EUROPEAN WIND ATLAS (NEWA) and DUTCH OFFSHORE WIND ATLAS (DOWA) reanalysis datasets. These studies will make use of the Scanning system based LiDAR (SCADAR) and vertical profilers as observations, and the high-resolution Weather Reasearch and Forcasting (WRF) model output. After a thorough analysis of the data sources, our research will attempt to fulfil the following research questions:

1. How well does the WRF model capture the orthogonal coastal wind gradients in comparison to SCADAR

observations?

2. To what extent the flow condition varies inside a coastal wind farm, and how well it can be simulated by mesoscale modelling?

After this introduction chapter, a concise review of the relevant literature on this subject will be presented in chapter 2. The methodology of this research regarding the data sources, model set-up, analysis approaches will be given in chapter 3. In Chapter 4, the base case scenario of the researching domain and synoptic condition for simulated cases will be described. Chapters 5 will contain a thorough description of the results both on the performance of WRF and on the wind speed gradient issue. In the end, some discussions, lessons learned, as well as recommendations for further research, will be presented in chapter 6, and conclusions will be drawn in chapter 7.

2

Literature Study

2.1. Wind technology

Wind energy has been directly used as mechanical power for various purposes such as pumping water, sailing, and grinding. The indirect usage of wind energy by converting the kinetic energy of wind into electrical energy was early performed in the USA, Ohio, in 1888. The kinetic energy for wind is contained in the moving air mass, and it can be determined as

$$E_{\mathrm{k}} = \frac{1}{2} m \bar{u}^2 \tag{2.1}$$

with the m is the air mass and $\bar{u}$ denotes the mean wind speed. The wind power is obtained by differentiating the kinetic energy in the wind with respect to time

$$P_{\mathrm{w}} = \frac{\mathrm{d}E_{\mathrm{k}}}{\mathrm{d}t} = \frac{1}{2} \dot{m} \bar{u}^2 \tag{2.2}$$

The wind turbines can extract a certain portion of wind power and converts it to electricity while the air mass passes the turbine and drives the blades to rotate. The flow rate of the air mass passes the blades is expressed as

$$\dot{m} = \rho A \bar{u} \tag{2.3}$$

where ρ is the density of air, and A is the swept area of blades. Hence, the available wind power P_w for a specific wind turbine is written as

$$P_{\mathrm{w}} = \frac{1}{2} \rho A \bar{u}^3 \tag{2.4}$$

Based on eq *2.4*, the amount of wind energy can be extracted by a wind turbine is determined by the air density, the rotor diameter, and most importantly, the mean wind speed, as wind power is proportional to the cubic power of the mean wind speed [Spera, 1994]. Thus the site selection for the wind farm is rather important that requires an accurate assessment of the wind resources and the possibility for installing large blade wind turbines.

There are two primary alternatives for wind energy such as onshore and offshore. A typical layout for both of them can be seen from fig 2.1. The offshore wind farms are generally constructed on the continental shelf area with the solid supporting structure which is on the seabed about 10 km away from the coast and 10s of meters deep [Bilgili et al., 2011]. The electric power generated from turbines is delivered to offshore substations and converted to high-voltage currents to minimize losses during the transport to the export cable. A noticeable difference is the elaborate foundation for the offshore wind turbines, usually a monopile (in shallow water) or a tripod or lattice construction for waters up to 40 m deep [Junginger et al., 2020].

Denmark was the pioneer to the development of offshore wind park [Kaldellis and Zafirakis, 2011]. 30 years ago in 1991, they constructed 11 turbines on the Vindeby which produces a total capacity of 4.95 MW. Since then, the vast techno-economical potential of offshore wind park has been noticed, and it started spreading exponentially across Europe. There are certain advantages for offshore wind parks, such as higher and more steady wind speed, and fewer restrictions from the local stakeholders as it makes no usage of the

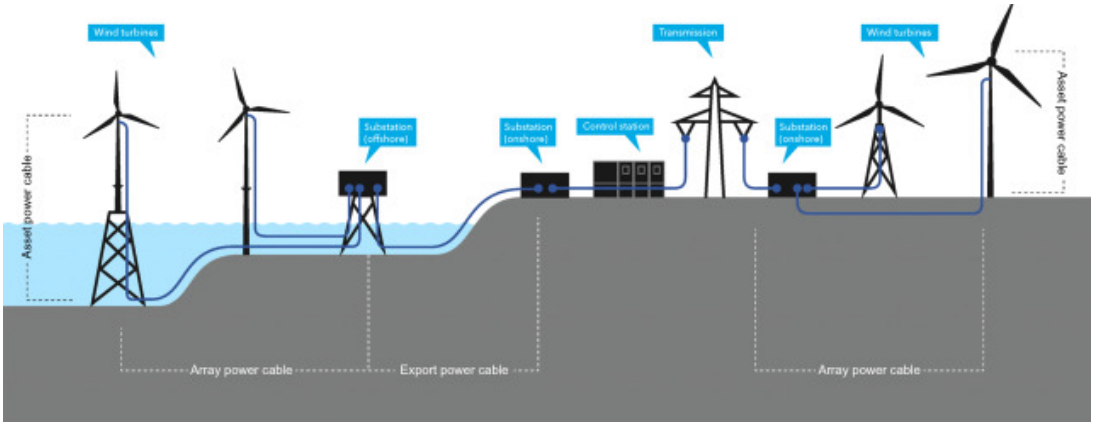

Figure 2.1: A schematic layout of offshore and onshore wind farm [Junginger et al., 2020].

land [Junginger et al., 2020]. As it is stated in the previous chapter, the construction cost could be massive compared with onshore wind parks, as it requires pre-foundation of the sites. Meanwhile, the maintenance and operation difficulties are essential considerations as the transportation lines are paved underwater, and the wind turbines are sited remotely.

Given the high cost of the traditional offshore wind farm, there is another alternative to expanding the wind farm to nearshore locations. The nearshore wind farm built in the shallow water is considered a cost-friendly option that significantly shrinks the cost gap between onshore and offshore wind farms. Studies, i.e., [Jacobsen et al., 2019; Gallagher et al., 2016; Wolsink, 2010], has been trying to evaluate the pros and cons of nearshore and offshore wind farm quantitively or ethically on their cost and competitive advantages. The cost advantages originate from the shorter distances of site deployment, power transportation, and maintenance at remote sites. However, it also regularly elicits higher resistance from the public as the local citizens might strongly disagree with the visual encumbrances, especially closer to the urbanized area. Meanwhile, the other stakeholders, such as farmers, fishermen, ships, may also be bothered, as they are relying on the coastal resources for life. In study [Jacobsen et al., 2019], the authors concluded that the nearshore water depth is the most critical consideration of the cost competitivity for a nearshore wind farm. They illustrated a calculation on the benefits that only 4% of the cost can be reduced if the water depth is not significantly lower than the offshore sites. If the water depth nearshore cannot reduce more than 10m while it moves 15km from shore, the nearshore wind farm is not socially attractive.

2.2. Coastal flow modification

The coastal wind flow will adjust both horizontally and vertically to reach the equilibrium of upstream conditions in the presence of the surface discontinuity concerning roughness and surface fluxes [Barthelmie et al., 2007]. Due to the difficulties of construction and massive economic cost for offshore wind resource measurements, a better understanding of this coastal flow modification is essential to access the high-quality assessment of actual wind energy production at the nearshore location.

The substantial wind speed gradients will significantly affect those wind farms located in the coastal region [Barthelmie et al., 2007]. The authors have argued that the spatial wind speed gradients at near-surface level (up to a height of 20m) within a relatively short distance of 1.2-1.7 km from the coast are significant for the offshore moving flows under all stability conditions. While the wind speed gradients at higher levels (38m and 48m) in the coastal zone are not fully adjusted to the discontinuities of surface roughness. These findings indicate that the wind speed distribution in the coastal zone depends on both the fetch from the coastline and stability condition [Pryor and Barthelmie, 1998]. This gradient at a typical hub height has been quantified to be 2 m/s over the horizontal extent of a large wind farm within the coastal region. Moreover, a suggestion has been made to use stability corrections to improve predictions of wind speed compared with the logarithmic profile.

A widely applied description of the atmospheric stability is the Monin-Obukhov length (L):

$$L = \frac{-u_*^3}{\kappa \frac{g}{\theta_0} \overline{w'\theta'}} \tag{2.5}$$

Where the numerator is the shear term with u_* denotes the friction velocity. The denominator is the buoyancy term with κ is the von Kármán constant and θ_0 is the reference potential temperature, and $\overline{w'\theta'}$ is the heat flux. The physical interpretation of it is the approximate height at which the turbulence is influenced more by buoyancy than shear. It is often derived from measurements of the ultrasonic anemometer, which measures the eddy-covariance.

$$u(z) = \frac{u_*}{\kappa}\left[\ln\left(\frac{z}{z_0}\right) - \Psi_m\left(\frac{z}{L}\right)\right] \tag{2.6}$$

It is frequently used to correct the wind speed profile with expression 2.6. Where the z_0 is the roughness length and the ψ_m is the universal stability function. If the wind speed at one height is given, the surface roughness and the Monin-Obukhov length L will determine the vertical wind profile. The wind speed offshore is often higher, as the surface roughness on the water is generally smaller than it is on the land. Moreover, some researchers Lange et al. [2003] have argued that the abrupt change of surface when the flow advecting cross the coastline might limit the Monin-Obukhov theory's applicability.

Table 2.1: Stability classed by Monin-Obukhov length [Van Wijk et al., 1990]

Stable	Neutral	Unstable
$0 \leqslant L \leqslant 1000$	$\lvert L\rvert \geqslant 1000$	$-1000 \leqslant L \leqslant 0$

In a research, Svensson et al. [2019] has studied flow field modification at the land-sea interaction for the high-latitude Baltic Sea. The authors using WRF simulated that the mean monthly increase in wind speed at hub height is up to approximately 1 m/s at typical hub heights. The large-scale low-level jet caused by surface property differences such as temperature will increase the wind speed and shear significantly. Moreover, the water surface roughness is unlike it on the land, usually remains constant over time, it is also related to wave field over the water surface, which, in turn, depends on the wind speed. The most widely used roughness model accounts for the effect of the atmospheric condition is the Charnock model [Charnock, 1955], which only depends on the friction velocity. Numerous numerical models [Lange et al., 2003; Taylor and Yelland, 2001] endeavor to improve the performance on resolving the wave fields by including other wave properties such as wave age and wave steepness. One of the essential consequences of these differences is the wind speed gradients over the offshore windfarm. Barthelmie et al. have analyzed the coastal wind speed gradient (Fig 2.2) located 13km from the coastline in the transect direction, mainly use the Synthetic-aperture radar (SAR) observation and the Wind Atlas Analysis and Application Program (WAsP) model. The authors calculated the averaged SAR dataset with more than 150 SAR images, and the absolute gradient is 0.8m/s, nearly doubled compared with the Karlsruhe Atmospheric Mesoscale Model (KAMM) and WAsP prediction at shorter fetch before it reached Horns Rev wind farm. The gradient fetch curves are smoother as the mesoscale

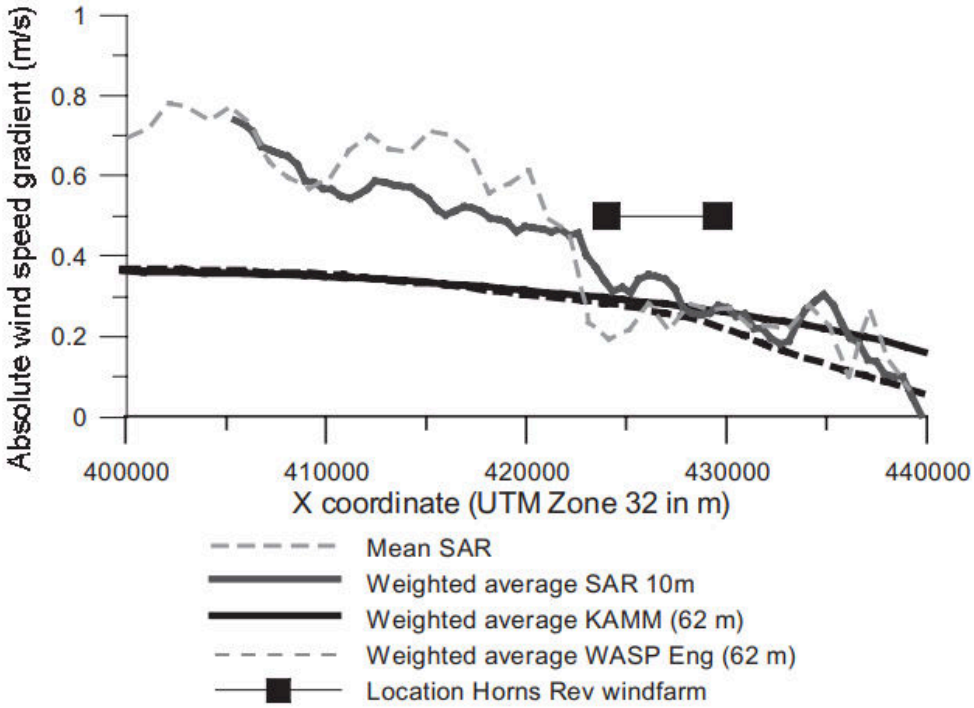

Figure 2.2: Wind speed gradient through the Horns Rev wind farm derived using remote sensing data and numerical models [Barthelmie et al., 2007]

thermal effects are not modelled in the WAsP engineering. Overall, The results of the difference in the absolute wind speeds within the range between UTM x coordinate 424000 m to UTM x coordinate 430000 m at Horns Rev wind farm is around 0.4 m/s on average over the transect for all the analyzed data sources. In a study of coastal flow using mesoscale modelling [Floors et al., 2013], the authors suggested that the roughness length default in the WRF model is much higher than that derived from observations at their study domain Høvsøre site, Denmark. The shear was frequently underpredicted especially at the lower levels. Thus less Low Level Jet (LLJ) events predicted by WRF compared with the measurements.

2.3. Internal boundary layer

According to the definition given by Glickman [2000], an internal boundary layer is a layer that develops within an existing atmospheric boundary layer due to horizontal flow advection across a transection with different surface properties, for instance, the aerodynamic roughness length, the surface temperature, or surface fluxes. This internal boundary layer will originate from the discontinuity and grow in depth along the downwind direction, until being homogenized with the existing boundary layer by ambient mixing. Almost without exception, this internal boundary layer always forms together with an inner equilibrium layer where the flow condition has entirely adjusted to the local boundary conditions[Garratt, 1990]. Moreover, above this equilibrium layer and within the internal boundary layer, there exists a blending layer (also referred as transition layer) where the flow condition is gradually adjusting from local boundary conditions to the downstream conditions [Plate, 1971] (see figure 2.3).

A variety of studies have been focusing on determining the internal boundary layer and formulating the internal boundary layer depth by using observational data and experiment results. Savelyev and Taylor has provided a useful review for the internal boundary layer both in the structure and formulation of it, several expressions are listed in the following table 2.2.

The concept of Internal Boundary Layer (IBL) involves the idea of flow characteristics modification at the lower boundary. Identifying the changing flow conditions requires tracking the flow from the downwind region to the upwind region. This makes the field studies challenging as the spatial distribution of large flow field could be considerably expensive to obtain. However, to simplify the measurement procedure, a limited number of profiles at downwind locations are commercially accessible in most cases. Therefore, the slab-mean wind profiles are the most common way to identify the IBL. The IBL height can be roughly deduced by looking at two wind speed profiles at downwind and upwind locations and find the height where the wind

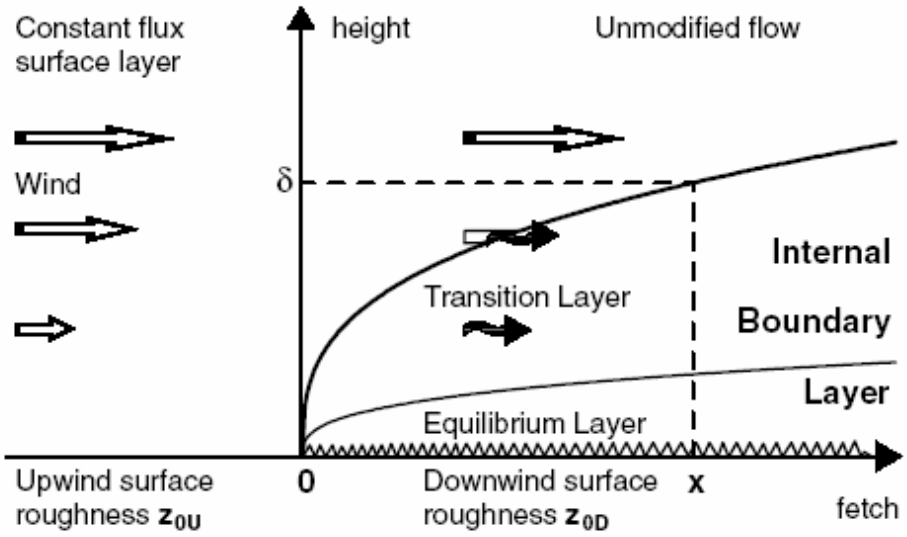

Figure 2.3: Schematic concept for internal boundary layer from Savelyev and Taylor [2005]

Table 2.2: Short fetch IBL height formulae (in chronological order). IBL height δ and distance from a leading edge x are in metres. [Savelyev and Taylor, 2005]

Formula	Author(s)	Notes
$1.25\kappa\frac{x}{z_{0D}} = \frac{\delta}{z_{0D}}\left(\ln\frac{\delta}{z_{0D}} - 1\right) + 1$	Pendergrass and Arya (1984)	
$\delta\left(\ln\frac{\delta}{z_{0U}} - 1\right) = 1.25\kappa(1 + 0.1M)x$	Savelyev and Taylor (2001)	$M = ln\frac{Z_{0D}}{Z_{0U}}$
$\frac{\delta}{z_0 D} = 10.56\left(\frac{x}{z_{0D}}\right)^{0.33}$	Cheng and Castro (2002)	

speed differs within a specified amount. If the measured wind speed profile is only accessible at one location, one can check if the lower part of the profile has a sign of the intersection for a new form of the log-law wind profile and the top portion reflecting the log-law shape from the old surface while the lower part represents the new-surface.

2.4. Numerical weather prediction & PBL parameterization

Numerical weather prediction (NWP) is an advanced scientific technology that makes use of mathematical models and physical principles to compute the future weather conditions [Brunet et al., 2015]. It requires immense information on atmospheric and oceanic circulation as the input forcing to tackle complex atmospheric problems. Parameterization is the essence of the NWP to replace the complex physical processes by simplified processes, such as solar radiation, moist process, the interaction of soil and water. As matter of fact that the simulation comprises constantly solving multiple sets of partial differential equations, the evolution of the NWP is closely associated with the development of computer hardware [Brunet et al., 2015], as it determines the computational power availability for complicated calculation. The basic numerical methods contain several governing equations written as the following expressions under the Cartesian coordinate system. For the conservation of momentum and mass (eq 2.7 and 2.8)

$$\frac{\mathrm{d}\vec{\mathrm{V}}}{\mathrm{dt}} = -\alpha\vec{\nabla}p - \vec{\nabla}\Phi + \vec{F} - 2\Omega \times \vec{V} \tag{2.7}$$

$$\frac{\partial\rho}{\partial t} = -\vec{\nabla}\cdot(\rho\vec{V}) \tag{2.8}$$

Where the $\vec{V} = (u, v, w)$ denotes the velocity of air, α is a specific volume, p and ρ is the pressure and the density of air, Φ is the geopotential height, F is the friction force, and Ω is the angular speed of the rotating earth. For conservation of energy and water mass, the first law of thermodynamics and the conservation equation for water mass is written as eq 2.9 and eq 2.10.

$$Q = C_p\frac{\mathrm{dT}}{\mathrm{dt}} - \alpha\frac{\mathrm{d}p}{\mathrm{dt}} \tag{2.9}$$

$$\frac{\partial\rho q}{\partial t} = -\vec{\nabla}\cdot(\rho\vec{\mathrm{V}}\mathrm{q}) + \rho(E - C) \tag{2.10}$$

where the Q is heat, q is the water vapor, E and C represent evaporation and condensation.

In spherical coordinates, λ, φ and r is introduced to represent the longitude, latitude and the radius of the earth. As the velocity of air $\vec{V}$ contains u, v, w three components, the conservation of momentum eq 2.7 is rewritten as eq 2.11, eq 2.12 and eq 2.13 for each component.

$$\frac{\partial u}{\partial t} = -u\frac{\partial u}{\partial x} - v\frac{\partial u}{\partial y} - w\frac{\partial u}{\partial z} + \frac{\mathrm{uv}\tan\varphi}{a} - \frac{\mathrm{uw}}{a} - \frac{1}{\rho}\frac{\partial p}{\partial x} - 2\Omega(w\cos\varphi - v\sin\varphi) + \mathrm{Fr}_x \tag{2.11}$$

$$\frac{\partial v}{\partial t} = -u\frac{\partial v}{\partial x} - v\frac{\partial v}{\partial y} - w\frac{\partial v}{\partial z} - \frac{u^2\tan\varphi}{a} - \frac{\mathrm{uw}}{a} - \frac{1}{\rho}\frac{\partial p}{\partial y} - 2\Omega u\sin\varphi + \mathrm{Fr}_y \tag{2.12}$$

$$\frac{\partial w}{\partial t} = -u\frac{\partial w}{\partial x} - v\frac{\partial w}{\partial y} - w\frac{\partial w}{\partial z} - \frac{u^2 + v^2}{a} - \frac{1}{\rho}\frac{\partial p}{\partial z} + 2\Omega u\cos\varphi - g + \mathrm{Fr}_z \tag{2.13}$$

Similarly, eq 2.8, 2.9 and 2.10 can be written as

$$\frac{\partial T}{\partial t} = -u\frac{\partial T}{\partial x} - v\frac{\partial T}{\partial y} + (\gamma - \gamma_d)\,w + \frac{1}{c_p}\frac{\mathrm{dH}}{\mathrm{dt}} \tag{2.14}$$

$$\frac{\partial\rho}{\partial t} = -u\frac{\partial\rho}{\partial x} + -v\frac{\partial\rho}{\partial y} - w\frac{\partial\rho}{\partial z} - \rho\left(\frac{\partial u}{\partial x} + \frac{\partial v}{\partial y} + \frac{\partial w}{\partial z}\right) \tag{2.15}$$

$$\frac{\partial q_v}{\partial t} = -u\frac{\partial q_v}{\partial x} - v\frac{\partial q_v}{\partial y} - w\frac{\partial q_v}{\partial z} + Q_v \tag{2.16}$$

Where the γ and γ_d represents the lapse rate and dry adiabatic lapse rate, c_p denotes the specific heat of air. Some other terms in the equations related to the diabatic effects (H), friction force (F_r), water gain and losses

through the phase change (Q_v), should also be defined within the model. With the additional equation for ideal gas law eq *2.17*, a full set of the primitive equations for NWP is defined.

$$p\alpha = \mathrm{RT} \tag{2.17}$$

These seven equations (eq *2.11* - *2.17*) with seven unknowns are the universal equations for NWP [Pu and Kalnay, 2018].

The simulations with sophisticated numerical models are performing for various purposes with different scales. The equations will be simplified with some assumptions to make it suitble for different coordinate systems and also to retain computational stability. As the NWP models are using numerical discretization to solve the equation sets, processes with a smaller scale than the grid space will not be explicitly resolved in the model, even though their contribution is not neglectable. One of the typical instances is the application of Reynolds decomposition and averaging [Stensrud, 2009] to resolve the turbulence motion, variables (e.g., u,v,w,T,p) will be separated into mean and turbulent parts denoted by the overbar and prime symbol respectively, for example

$$\begin{aligned} u &= \bar{u} + u' \\ T &= \bar{T} + T' \\ p &= \bar{p} + p' \end{aligned} \tag{2.18}$$

When these expressions are substituted into eqs *2.11* ~*2.16*, it produces the following expansions as an example

$$u\frac{\partial u}{\partial x} = \left(\bar{u}+u'\right)\frac{\partial}{\partial x}\left(\bar{u}+u'\right) = \bar{u}\frac{\partial \bar{u}}{\partial x} + \bar{u}\frac{\partial u'}{\partial x} + u'\frac{\partial \bar{u}}{\partial x} + u'\frac{\partial u'}{\partial x} \tag{2.19}$$

Taking average on both sides, it produces

$$\overline{u\frac{\partial u}{\partial x}} = \overline{\bar{u}\frac{\partial \bar{u}}{\partial x}} + \overline{\bar{u}\frac{\partial u'}{\partial x}} + \overline{u'\frac{\partial \bar{u}}{\partial x}} + \overline{u'\frac{\partial u'}{\partial x}} \tag{2.20}$$

As $\overline{\bar{a}b'} = \overline{\bar{a}}\,\overline{b'} = \bar{a}\overline{b'} = 0$, the second and the third term on the right side will end with 0, hence

$$\overline{\bar{u}\frac{\partial u}{\partial x}} = \bar{u}\frac{\partial \bar{u}}{\partial x} + \overline{u'\frac{\partial u'}{\partial x}} \tag{2.21}$$

Thus

$$\frac{\partial u}{\partial t} = -u\frac{\partial u}{\partial x} - v\frac{\partial u}{\partial y} - w\frac{\partial u}{\partial z} - \frac{1}{\rho}\frac{\partial p}{\partial x} + \mathrm{fv} + \frac{1}{\rho}\left(\frac{\partial \tau_{xx}}{\partial x} + \frac{\partial \tau_{yx}}{\partial y} + \frac{\partial \tau_{zx}}{\partial z}\right) \tag{2.22}$$

With $\tau_{zx} = \mu\frac{\partial u}{\partial z}$, and $T_{zx} = -\bar{\rho}\overline{\mathrm{u'w'}}$ and similarly for other components, it produces

$$\frac{\partial \bar{u}}{\partial t} = -\bar{u}\frac{\partial \bar{u}}{\partial x} - \bar{v}\frac{\partial \bar{u}}{\partial y} - \bar{w}\frac{\partial \bar{u}}{\partial z} - \frac{1}{\bar{\rho}}\frac{\partial \bar{p}}{\partial x} + \mathrm{f\bar{v}} + \frac{1}{\bar{\rho}}\left(\frac{\partial}{\partial x}\left(\tau_{xx}+T_{xx}\right) + \frac{\partial}{\partial y}\left(\tau_{yx}+T_{yx}\right) + \frac{\partial}{\partial z}\left(\tau_{zx}+T_{zx}\right)\right) \tag{2.23}$$

The first five mean value terms are represented by the model grid cell values, while the last part inside the parentheses cannot be explicitly resolved, and its contribution cannot be neglected. Therefore, closure schemes are needed to resolve these turbulent fluxes from the subgrid-scale mechanisms of the atmospheric physical processes.

There are several typical Planetary Boundary Layer (PBL) parameterization schemes employed in the WRF or other NWP models. These schemes are distinguished mainly considering two features of them. The first easier concept is the local/nonlocal parameterization schemes. It describes how many levels that the known variables will affect the perturbation quantities at a given point. In the local closure schemes, the variables at the given point are only determined by those vertical levels that directly adjacent to that given point. On the other hand, those nonlocal closure schemes will account for multiple vertical levels thus generally better represent the large scale mixing throughout the PBL. As a consequence, the computational cost is usually higher than the local closure schemes [Cohen et al., 2015].

Another essential feature is the order of the turbulence closure. As the theoretical background for the PBL parameterization is to divide variables into the mean and the perturbation components, the equations for characterizing perturbations will always have one more unknown terms than the known terms. Hence, to model these turbulent fluctuations, it requires formulating the unknown term to the existing known terms

to develop a turbulence closure. Generally, we have the first-order closure describes the turbulent fluxes as a proportional to the gradients of the mean variables [Wallace and Hobbs, 2006], to give an example

$$\overline{w'\theta'} = -K_h \frac{\partial \bar{\theta}}{dz} \tag{2.24}$$

in this case, K_h is the eddy diffusivity for heat. It is also applicable for expressing the momentum and moisture fluxes. Medium-Range Forecast (MRF) scheme is an example of early developed first-order closure. It introduced a counter gradient correction term into downgradient diffusion instead of solely considering the local mixing.

Later on, the closure schemes to solve the equations are developed with only a few second-order moments and parameterizing the rest of them to compromise between the simplicity of the first-order closure and the complexity of the full second-order closures [Holt and Raman, 1988]. Turbulent kinetic energy (TKE) is a second-order variable that quantifies the turbulent motion, it characterizes the magnitude of turbulence in the PBL due to the vertical wind shear, buoyancy, turbulent transport driving by molecular viscosity [Holton, 2004]. The first approach with 1.5-order closure Mellor-Yamada-Janjic (MYJ) prognostically solve for TKE, and it is tested to be comparable to those full second-order closure with only a small fraction of the computational cost [Mellor and Yamada, 1982]. Another 1.5-order closure scheme is Mellor-Yamada-Nakanishi-Niino (MYNN2) [Nakanishi and Niino, 2004]. In this approach, the stability and mixing length are expressed by the Large Eddy Simulation (LES) results instead of the observations. The eddy viscosity K_m in the $K-$theory is expressed as $K_m = lqS$ with a length scale l, a stability function S and q defined as $\sqrt{2TKE}$. This approach is proved to perform better in simulating the deeper mixed layer compared with conventional MYJ scheme. However, being as a local scheme, it still cannot fully resolve the large eddies throughout deep vertical mixing layers.

The closure scheme used in this study is the nonlocal Yonsei University (YSU) scheme with first-order closure. It is a similar approach to the MRF scheme, but in additional explicitly calculates entrainment at the top of the PBL. It is argued to perform better in simulating strong-wind regimes with shallower mixing compared to the MRF scheme [Hong et al., 2006]. The YSU scheme expresses the turbulent fluxes of momentum with a modified $K-$theory.

$$\begin{aligned} \overline{u'w'} &= -K_m \left(\frac{\partial U}{\partial z} - \gamma_c \right) - \overline{u'w'}_h \left(\frac{z}{h} \right)^3 \\ \overline{v'w'} &= -K_m \left(\frac{\partial V}{\partial z} - \gamma_c \right) - \overline{v'w'}_h \left(\frac{z}{h} \right)^3 \end{aligned} \tag{2.25}$$

where z is the height above the ground, γ_c is a correction term of the local gradient to include non-local mixing, and $\overline{v'w'_h}$ is the entrainment at the top of the boundary layer. The eddy diffusivity K_m is prescribed as

$$K_m = u_* \kappa z \phi_m^{-1} \left(1 - \frac{z}{h} \right)^2 \tag{2.26}$$

with the dimensionless wind shear $\phi_m = \left(\frac{\kappa z}{u_*} \right) \frac{\partial U_z}{\partial z}$ which is a function of z/L.

2.5. LiDAR Observation

A wind Light Detection and Ranging (LiDAR) system uses the optical Doppler effect to measure the atmospheric wind with high spatial and temporal resolution [Reitebuch, 2012]. It obtains information on the flow condition by sending out rapid and frequent pulses and receiving backscattered signals when the pulses encountered with particles, aerosols, or molecules within the air volume. Therefore, the data availability of a wind LiDAR depends on the weather condition. In other words, it relies on how many signals can return within the range of the cone air column. Different types of wind LiDAR devices are deployed for various purposes. The most commonly used wind LiDAR system is a ground-based wind profiler that transmits optics vertically and measures the full wind vector [Li and Yu, 2017]. It is much cheaper than building a metrological mast and can measure wind data up to 200m above ground level, and numerous studies, e.g., [Smith et al., 2006; Sun et al., 2005; Kim et al., 2016] has validated its accuracy at different sites under various meteorological and terrain conditions. For the offshore measurements, Floating LiDAR system (FLS) is a pre-commercial option [Gottschall et al., 2017] for the accuracy of the wind measurements regarding a suitable reference met mast. Another attractive technology is the Nacelle-based lidars that directly installed on the nacelle of wind turbines. This technique is favourable for consistently measuring the central transect of the wake, thus plays an essential role in the optimization of the turbine spacing. In the study of Aitken and Lundquist [2014], the authors used the Nacelle-based LiDAR concluded a 60% of turbine downwind velocity deficit at a distance of 1.8 rotor diameters to 40% at 6 rotor diameters. It is expected to be not very suitable for measurements in complex terrain as the terrain elevation is not constant around a turbine. One of the possible solutions is using computational fluid dynamics to correct the LiDAR measurements, which is also applied to ground-based LiDAR observations [Menke et al., 2018].

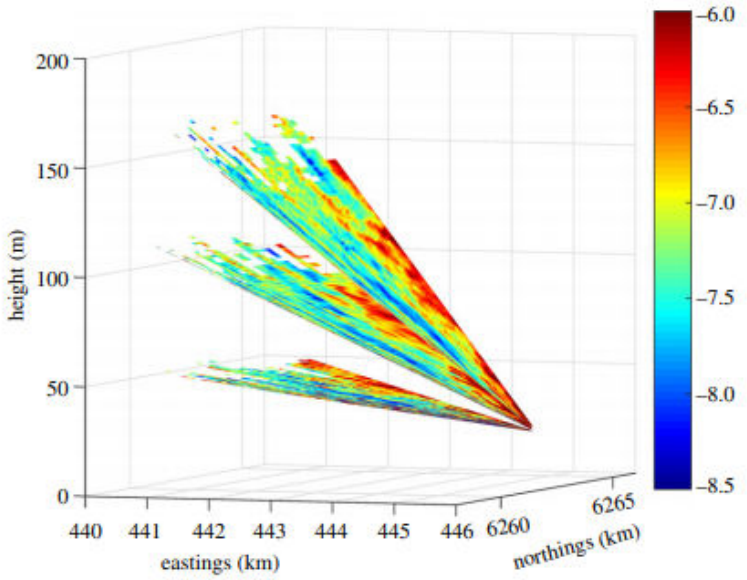

Figure 2.4: An example of SCADAR scanning poition at three elevations [Mann et al., 2017]

A state of the art technology is SCADAR that scans in a long-range up to 6km in this study. Therefore, it is also referred to as Long-Range Wind Scanner System. In an offshore measurements experiment, the WindCube 400S used in this study observed in the maximum range of 8km [Floors et al., 2016]. This wind scanner system was originally designed for 3D wind field and turbulence observation. It has two or more different sets of the scanner system for both the short-range and long-range observation controlled by the central master computer. This allows the WindScanner applicable in many wind engineering fields, such as study the flow pattern and dynamical loads on wind turbines, building structure and bridges [Mikkelsen et al., 2017].

In the scanning LiDAR system, the wind speed along the beam direction can be calculated via the observed Doppler frequency shift. This retrieved velocity is also known as the line of sight (LOS) velocity or the radial velocity u_r. With this LOS velocity, the wind speed vector u, v, w can be reconstructed with the additional scanning sector information, e.g., the azimuthal angle θ and the elevation angle ϕ. This WindCube 400S can have up to three elevations of Plan position indicators (PPI), which means at the same azimuthal

and range, the observations at three different heights are accessible using this technology. Hence the information of flow condition is extended both horizontally and vertically. An example of its scanning position can be found from the fllowing Fig 2.4. A systematic validation work of this device can be found from [Cameron,

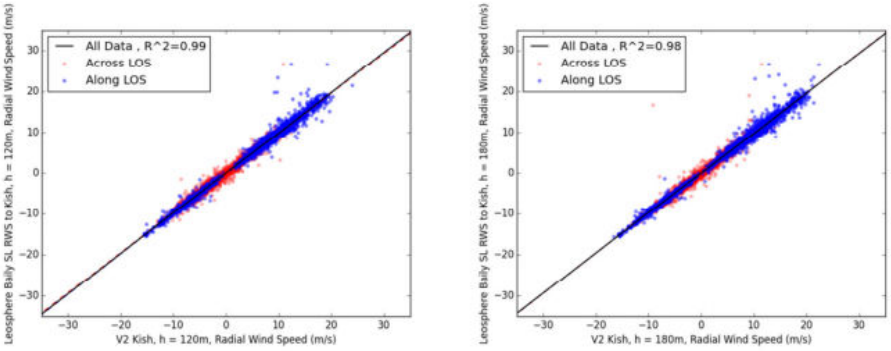

Figure 2.5: Validation of WindCube 400S at the Baily Lighthouse against the Vertical profiler at Kish Lighthouse for observed radial wind speed at 120m and 180m height.

2016]. In their study, the long-range scanning LiDAR WindCube 400s and the vertical profiler are deployed at East Pier and Baily lighthouse and Kish lighthouse at Anholt Wind Farm Dublin Bay. The validation results show sufficiently well coherent for observed radial wind speed with the R^2 values are 0.985 and 0.981 for 120m and 180m height respectively (Fig 2.5). This excellent measurements further indicated that the inaccuracies are more likely to be introduced via assumptions from the post-processing stage, rather than originated from the raw measurements.

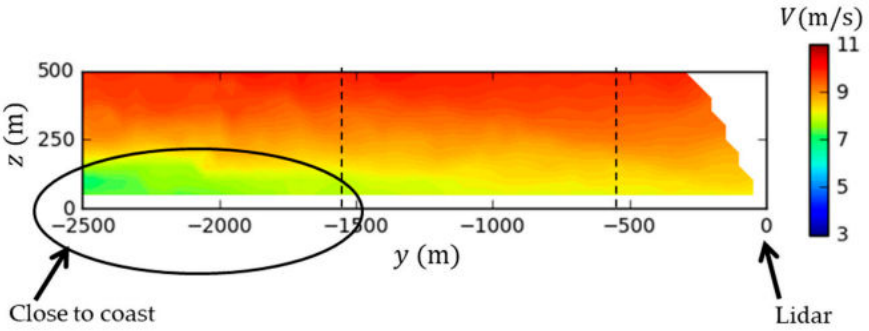

Figure 2.6: SCADAR observed wind field during 28^{th} Nov 2016 from 12:00 to 15:00. [Goit et al., 2020]

Given the long-range of the scanning LiDAR technique, it has been used to investigate the coastal flow field in various studies, as the lack of obstacles and topography allows the light propagation smoothly. In the study of Goit et al. [2020], the offshore wind fields at Choshi city of Chiba prefecture, Japan, are analyzed by the SCADAR measurements against WRF simulation. The IBL with strong shear is observed developing from the coastline (Fig 2.8). Moreover, the differences between their WRF simulation and SCADAR observation are around 10% up to 500m. The errors are much lower below 300m and increased substantially to nearly 20% from 300m height to 500m 2.7.

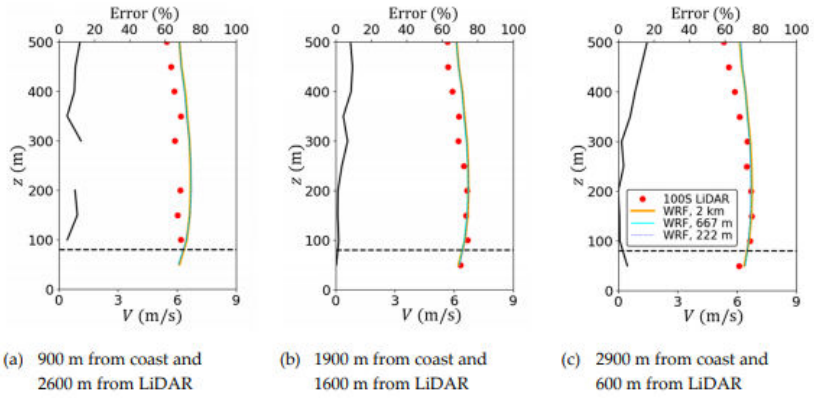

Figure 2.7: Vertical profile of WRF versus the SCADAR at three different distance from the coast during 28^{th} Nov 2016 from 12:00 to 15:00, the black unlabeled curve is the error of simulation in (%)[Goit et al., 2020].

In Misaki et al. study, the authors investigated the WRF simulated horizontal wind speed gradient against the SCADAR measurements at the coast of Kamisu, Japan. Their results show that the WRF model frequently underestimated the gradients while the wind blows from the land sectors, and it cannot be significantly improved by merely changing the PBL schemes. This underestimation exists for most of the wind direction but especially noticeable for the alongshore wind direction. The author concluded that the underestimation is originated from the large positive bias at the shorter distance from the coast simulated by WRF. Overall, the wind LiDAR is proved to have no bias compared to the cup anemometers observation in many studies. Thus, it is highly useful for evaluating the performance of mesoscale modelling and different PBL schemes.

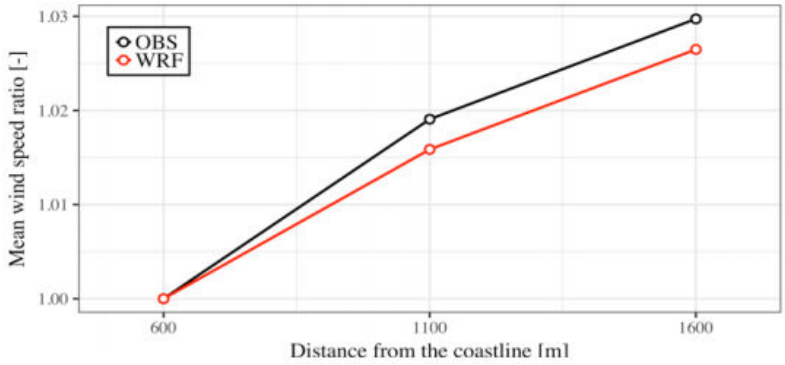

Figure 2.8: Mean horizontal wind speed gradient ratio agianst the distancce from the coastline [Misaki et al., 2018].

.

3

Methodology

This study aims to quantify the coastal wind speed gradients present at the wind plant Blauw on the lake IJsselmeer and evaluate the performance of WRF simulation against the SCADAR measurements. The detailed usage of observation, reanalysis data, the model set up, and the case selection will be described in this chapter. As the study involves various sources of data, the data usage information is listed in the following table 3.1. The NEWA and the DOWA data was pre-analyzed for several purposes. Firstly to have an overview of the climatology over the study area as ten years of data is available from them. Besides, by visually investigating the predicted vertical wind profile from both of them, several unrealistic behaviors are revealed from the NEWA wind profile, as the 10m height wind speed regularly exceeded the 50m height wind speed at 12 UTC. Moreover, the case selection is based on the NEWA dataset as it has the largest overlap on timespan with the SCADAR observations. It is also convenient in terms of processing data compared with running WRF simulation with a coarse resolution to identify the simulation cases.

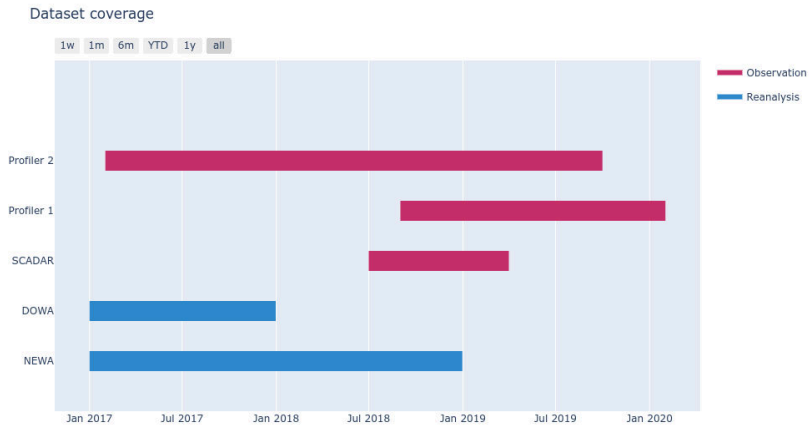

Figure 3.1: The time span of each dataset. The red bars represent the observational data from two wind profilers and a SCADAR, the blue bars represent the reanalysis data from DOWA and NEWA.

Table 3.1: Description of data use

Data	Type	Sampling rate	Spatial resolution	Temporal	Vertical range
NEWA	Reanalysis	30min	3km	1989-2018	10-500m
DOWA	Reanalysis	1h	2.5km	2008-2017	10-600m
SCADAR (WindCube 400S)	Observation	10min	(6 km range)	2018-07 to 2019-04	90-440m
Profiler 1 (ZP583)	Observation	10min		2018-09 to 2020-02	38-220m
Profiler 2 (ZP581)	Observation	10min		2017-02 to 2019-10	38-220m

The wind profilers can provide measurements in a vertical array that is not accessible via the SCADAR. However, it did not cover most of the SCADAR operating period. Therefore, only a portion of profiler observations is used to compare with the vertical profile of WRF at the mast location as it is deployed next to the met mast.

3.1. Scaning LiDAR Measurements

Table 3.2: Details of scanning LiDAR installation and operating.

Installation		Scan scenarios	
Site Name	Windplan Blauw	Scan Azimuth	296.6° - 359.6°
Install date	03/07/2018	Scan Elevations	5.60° , 6.25°
Install elevation	3.5m	Azimuth Resolution	$3°/s$
Install location	Irene Vorrink Windfarm, Flevoland	Spatial Resolution	100m
Install Coordinates	672806E , 5829472N	Range	200m - 6000m

The measurement instrument WindCUBE 400S scanning LiDAR operates at Irene Vorrink windfarm in Flevoland, Netherlands, as part of project Blauw. Monthly data is obtained by applying the reconstruction algorithm and validated with the wind profilers. Table 3.2 presents the details of LiDAR installation and the programmed scan scenarios.

The SCADAR performs sector scans over a 90 ° arc at two elevations. This two elevations will give two sets of changing heights depending on the position of the reconstruction point, in other words, the distance from the SCADAR. The height of the lower level used in this study is 138.7m at the Mast location (can be seen from Figure 3.2) 1800m away from the SCADAR, and it increases linearly to 441.1m at the BU24 5800m away.

The LiDAR data is post-processed by the third-party Oldbaum Services. Hence only 10min resolution time-series at reconstruction points available instead of the spatial image.

Figure 3.2 shows the layout of windplan Blauw with all the relevant elements marked out. They are all the selected reconstruction points that will be measured directly as time-series. As the LiDAR system fires rapid pulses and measures the backscattering signal, the information of wind is retrieved based on the doppler effect. The problem arises if the signals could not be received by the SCADAR when the adverse weather occurs, such as raining heavily or foggy. Hence the data availability, which represents the exact number of valid signals, is varying among seasons and also decreases with the distance from the base location. Some data gaps reported in the results chapter are caused either by the maintenance of the devices or the low transmittance weather. It can be checked from the local weather forecast website as the LiDAR devices have no indicator of the weather conditions.

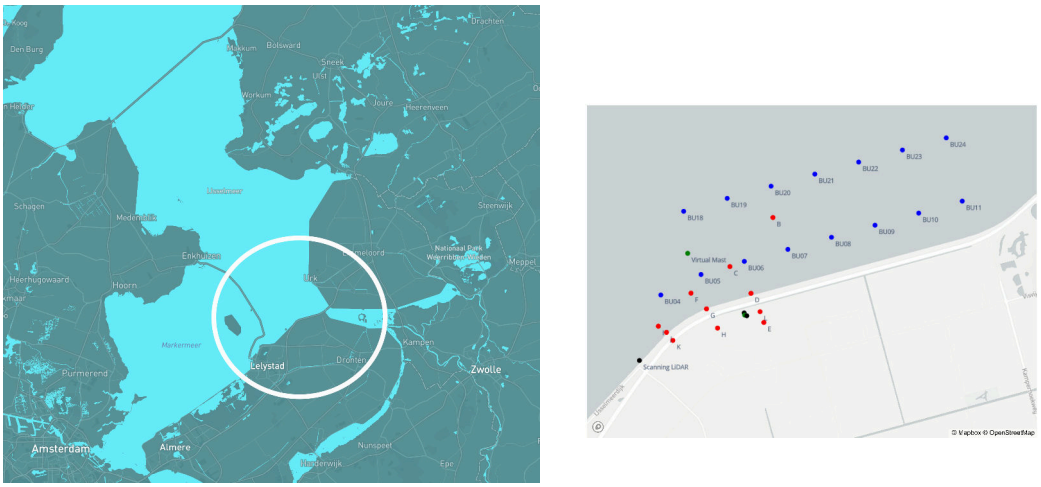

Figure 3.2: The layout of the Windplan Blauw with scanning LiDAR and its reconstruction points marked out. The black dot at the bottom left is the position of scanning LiDAR, the other two black dots overlapped together with the green dot (position of the met mast) are one of the grid points of WRF and the position of the ground-based LiDAR respectively. The blue dots are the wind turbine locations, and the green dots represent the met mast location and a virtual mast location on the water.

3.2. Modeling

In this study, the WRF version 4.0.0 was performed with three nested domains of 9/3/1 km resolutions respectively. The data from the innermost domain is used for this research. There are 65 vertical grid points prescribed with an increased resolution closer to the surface in order to capture processes in and close to the boundary layer. The domain setup can be seen from Fig 3.3. The PBL parameterization scheme used here is the YSU PBL scheme. The land surface scheme used in these simulations is the Noah scheme as it needs to capture the mesoscale circulations forced by surface variabilities such as albedo, soil moisture, soil temperature, snow, and landuse. Moreover, other parameterization schemes used in this study are RRTMG scheme for the radiation, Tiedtke scheme for cumulus and Thompson scheme for microphysics.

The European Centre for Medium-Range Weather Forecasts (ECMWF) ERA5 data is forced as the initial condition and boundary condition of WRF simulations. Each simulation covers a 24h period with 6s per time step, it records the history results every 10mins for all interested variables. Unlike the measurements are presenting the 10mins average for each time step, the WRF results are recording the instantaneous atmospheric conditions calculated at that time step.

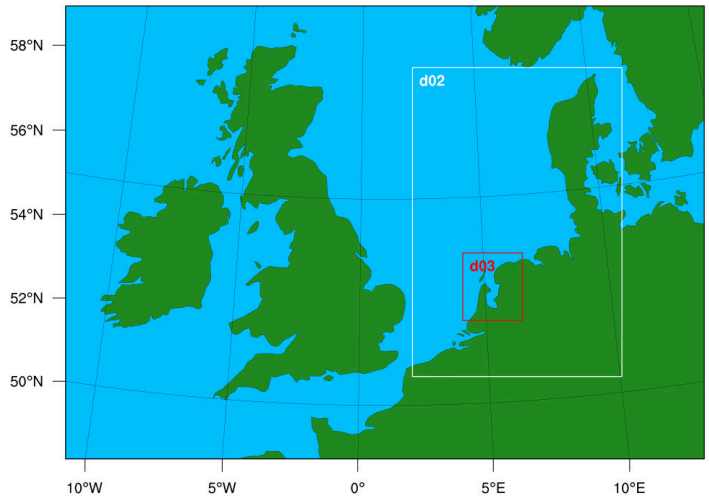

Figure 3.3: WRF domain configuration.

3.3. Case selection

This study is mainly interested in three flow sectors. These cases are selected by investigating the NEWA instead of running WRF at coarse resolution. As the wind direction frequently shifts over time, the selection of flow cases follows two criteria. Firstly, the overall wind direction should range within the desired flow direction sector with less than 40° differences. Secondly, the wind direction should hold steadily for periods longer than 24 hours with none or least fluctuations exceeding the range of the desired direction ±20°. The first flow category is the prevailing wind direction about 240° parallel to the coastline directly to the SW direction. It generally shows the largest orthogonal horizontal wind speed gradient due to the presence of different surfaces while looking from the NEWA data. The other two are those flow cases across the coastline for both onshore and offshore direction, which is approximately 160° and 340° respectively . As it is advecting across the coastline, it shows the largest possibility of causing the decoupling of the atmospheric boundary layer and forming the internal boundary layer.

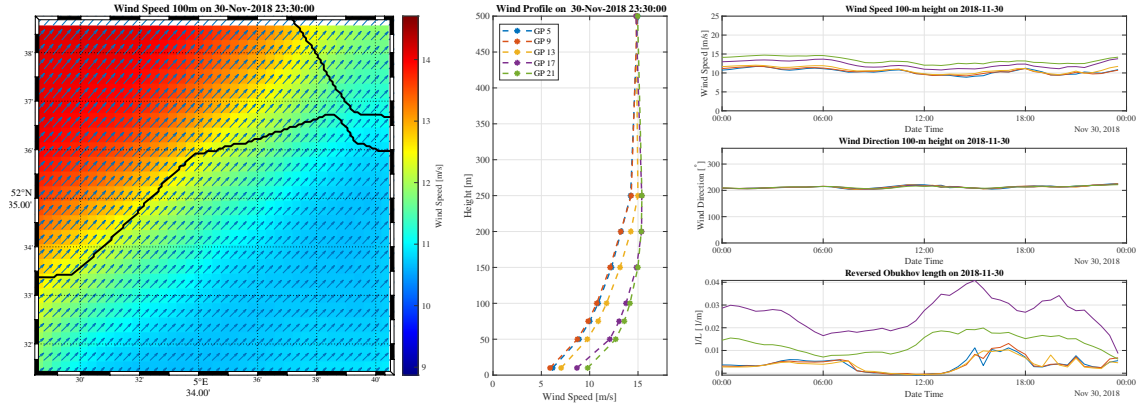

Figure 3.4: An example of processing the NEWA data for case selection, the extracted 5 sites are grid points 5, 9, 13, 17, 21 which can be checked from Fig 4.1.

An example of analyzed NEWA data is shown in Fig 3.4, cases with selected wind direction, and lasted long enough to cover the whole simulation will be selected for further study. The substantial wind speed gradient also contributes to the acceptance of the cases.

A rough comparison of the NEWA and SCADAR fully overlapped timespan is presented to obtain overall reliability of the NEWA data (Fig 3.5).

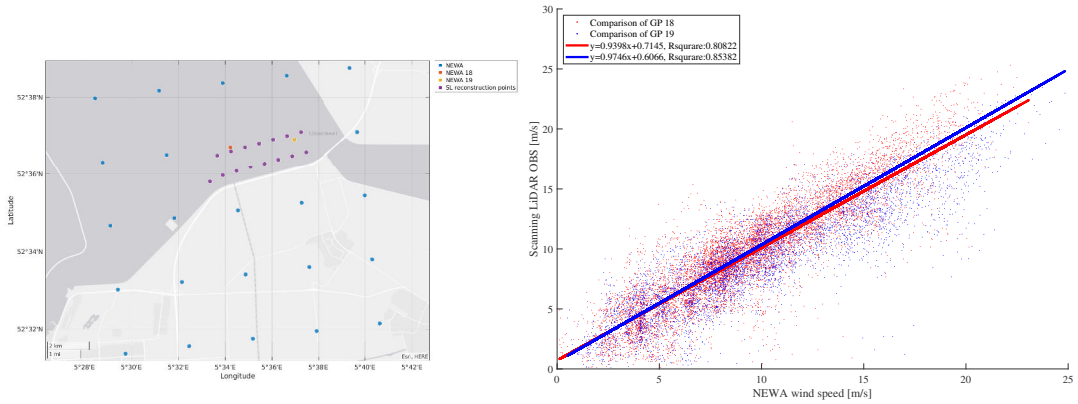

Figure 3.5: Comparison between fully overlapped period (from July 2018 to Dec 2018) of NEWA and SCADAR data.

Horizontally, the spatial resolution of NEWA is 3km, which cannot resolve all the reconstruction points from the SCADAR. Hence only the grid point 18 and 19 of NEWA are selected to compare with its surrounded measurement locations. As the vertical array of NEWA only contains few heights of data that not the same height with the SCADAR inclinations height, the spline interpolation is applied vertically to make these two datasets comparable.

After examining all the flow cases within the SCADAR covered period, three major sectors of 7 cases are selected depending on the wind direction sectors described before. Detail of selected cases can be found from the following table 3.3.

Table 3.3: Case selected for WRF simulation

Flow case ID	Date	Flow direction
1	2018-08-18	Alongshore - 240°
2	2018-09-11	Alongshore - 240°
3	2018-10-08	Alongshore - 240°
4	2018-10-11	offshore - 160°
5	2018-11-30	Alongshore - 240°
6	2018-12-10	onshore - 320°
7	2018-12-26	Alongshore - 240°

4

Base Case Scenario & Synoptic Maps

4.1. Base Case Scenario from NEWA & DOWA reanalysis data

According to the map layout Fig 4.1, the grid points of NEWA & DOWA datasets can be classified into different categories by their locations and the distances between the grid points from NEWA & DOWA with the same grid points number. Few features of the grid points will be emphasized for the robustness of the statistical results. Grid points from the first four rows, including grid points number 11,12,16,17,18,19,21,22,23,24, are located on the ocean. The rest of them are located on the land while the grid points 20 of NEWA & DOWA are separated by the land edge, which should be considered as less comparable. The relative position should also be taken into consideration. For instance, site 12 of NEWA & DOWA is located with an obstacle in between which might cause flow detachment and change the flow condition significantly. Site 10 for the NEWA & DOWA datasets are coincidentally intersected very well, which is predicted to have the closest statistical results among all the grid points located on land. However, for the grid points on the ocean, the results are predicted to be very close due to the lack of land-surface effects and geographic obstacles, even the distances between DOWA grid points and NEWA grid points vary quite a lot among them. When the horizontal gradient is interested, it is recommended to look at grid points 5, 9, 13, 17, 21, which lined diagonally over the layout map. The horizontal gradient can be derived by differentiating the wind speed over these grid points. Note that the general statistics give an overview of the flow condition among this windplan Blauw domain. Several interesting features of wind, such as the profile, are averaged over year by the selected period within a day, which could be less comprehensive while the wind flow condition varies not only following the diurnal cycle but also strongly depends on the season and general climate cycle.

4.1.1. Wind speed PDF statistic

In order to have an overview of the wind speed over the study domain, the wind speed time series over 2017 were plotted at the beginning to see if the datasets of DOWA and NEWA follow the same trend. However, the time series of a whole year datasets with 30 min / 1-hour min temporal resolution is too noisy to read. After the basic trend of time series is confirmed to be similar for all pairs of the DOWA and NEWA grid points, the time series plots were replaced by the probability density function curves created by fitting it to Weibull distribution with a scale parameter λ and a shape parameter k. The height is selected over all the options from NEWA datasets including 10m, 50m, 100m, 150m, 200m and 500m, mentioning that the DOWA data of 60m was selected in comparison of the NEWA datasets from 50m height due to the inconsistency of vertical levels between DOWA and NEWA data. Few general conclusions are revealed from the figures shown in the appendix chapter (Fig A.1,A.2,A.3,A.4,A.5).

1. **The PDF curves for both DOWA and NEWA datasets corresponded very well for all the heights except the 10m height.**
   By looking at all the heights, differences can barely be seen for the higher elevations. However, for the 10m height, the peaks of the PDF curve are generally shifting to the left side (lower wind speed) as the location moving towards land and further away from the intersection between land and lake. The discrepancies between DOWA data and NEWA data at 10m height are pronounced for almost all the grid points on the land, even site ten where the grid points of NEWA and DOWA intersect very well. On the other hand, the PDF curves corresponded much better for the grid points on the ocean

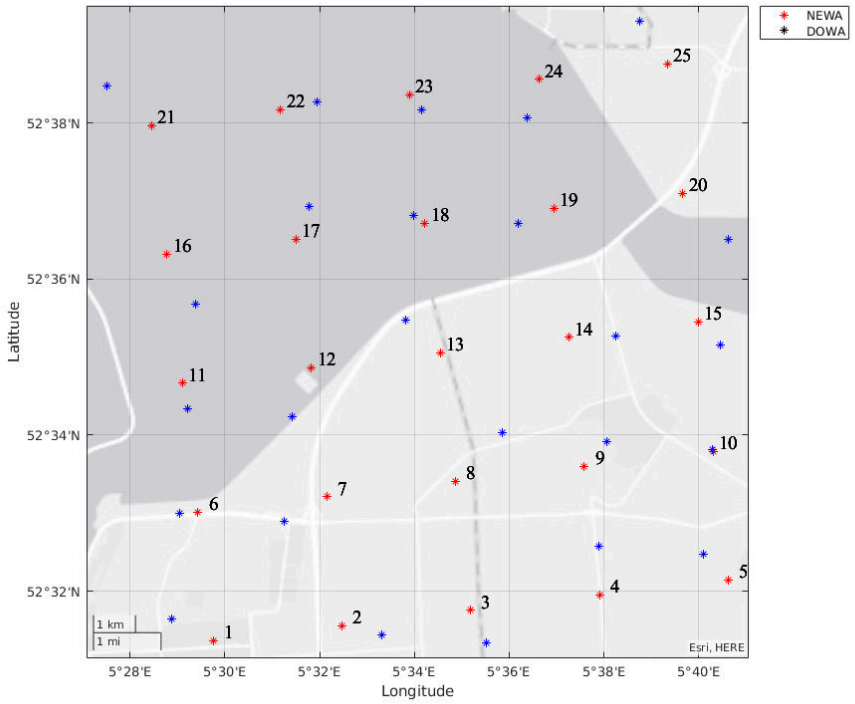

Figure 4.1: DOWA & NEWA grid points layout within the intersted domain.

(grid points 11,12,16,17,18,19,21,22,23,24). The largest differences between NEWA and DOWA show up among the grid points located close to the coastline. These discrepancies could be caused by different parameterization for the surface level of the models used by DOWA and the NEWA datasets.

2. **The peak probabilities are lowering with the increases of elevation, which indicates a slightly more evenly distributed wind speed at higher elevations.**
   As it is a common consensus, the wind speed will be higher with rising elevation within the same boundary layer while the decoupling of the boundary layer is out of consideration, the general statistic results show the same pattern that the higher wind speed (larger than $15 m/s$) is more commonly to be seen at the level above 200m, and the peaks are generally smaller which means a more even distribution among all different wind speeds.

3. **Spatial differences are worth investigating below 200m since the higher elevation tends to have a homogeneous flow over the whole domain.**
   The wind speeds are generally found larger with smaller peak probabilities at lower wind speeds when the location moves towards the ocean and further away from the land. This trend mainly applied to the lower elevation where the flow field is strongly affected by the land surface and geography obstacles. As the height rising (above 200m or higher), the spatial variability is less likely to be seen, at least a smaller gradient horizontally.

4.1.2. Vertical profiles at 0Z,6Z,12Z,18Z

According to the vertical profiles (Fig A.6,A.7,A.8,A.9) over the different timesteps in a day, the models used by DOWA and NEWA perform very differently in different stability condition, which reflected by the periods selected for the profiles. Assuming the atmospheric boundary layer will experience a relatively stable condition during the night, which is interpreted by 0Z, while the day time condition selected as 12Z is more likely to be the unstable condition in which the heat flux is going upwards, and the boundary layer height will grow. At 6Z and 18Z, there will be a transition period in which the neutral condition is the domain stability stratification, which is also the most frequent cases in the general statistic. For this 0Z night time stable condition, the NEWA data shows a generally larger wind speed at the higher elevation (above 100m) and lower wind speed at a lower level (below). There are intersections of DOWA and NEWA datasets at around

100m denotes a similar prediction at this level. It is good to have similar results at this level since the accurate prediction of the hub height is crucial for the estimation of energy production. However, the shear predicted by NEWA and DOWA datasets differs notably. As the same pattern revealed in the PDF curves, profiles also show that the wind speed at 10m height is substantially affected by the surface land cover, the 10m wind speed is generally higher at the ocean grid points and move towards to the right side (lower speed) while the grid points move towards to land and further away from the coastline. Moreover, the shear is considered to be larger overland due to the stable stratification at 0Z. For the 6Z time period, DOWA and NEWA datasets overlap much better than the stable night case. However, the lower part still has quite a large discrepancy. The shifting of the profile to the right side is still very obvious, which denotes a larger wind speed over the wide-open water rather than on the land, which significantly restricted by geography and obstacles. The most interesting part is the 12Z vertical profiles. Most of the grid points on land from the NEWA dataset show a local maximum at the lowest level, which cannot be seen from the DOWA dataset.

4.2. Observations from Scanning LiDAR

This section gives an overview of windplan Blauw climatology based on SCADAR observation. Data are categorized by months to see the seasonal effect on the flow pattern over the wind farm. Fig 4.2 shows the wind frequency in the study area. The most frequent flow cases are those wind directions within the range of 180° to 270°, it dominates the spring flow condition. During summer, it is prevalent to have sea breezes as the surface temperature of the water could be much cooler than the land, thus a higher pressure and onshore breeze occur frequently. On the contrary, during the winter, the temperature on land tends to be cooler, thus a higher pressure drawing the air mass moving offshore. As for the wind speed, the highest wind speed generally coupled with the dominant flow sector, which is the alongshore flow direction if the long term flow condition described by the NEWA is considered (Fig A.10 - A.17). The high wind speed over 20m/s usually takes place in the winter, and it rarely captures the low wind speed below 4m/s. The low wind speeds generally happen in the summertime.

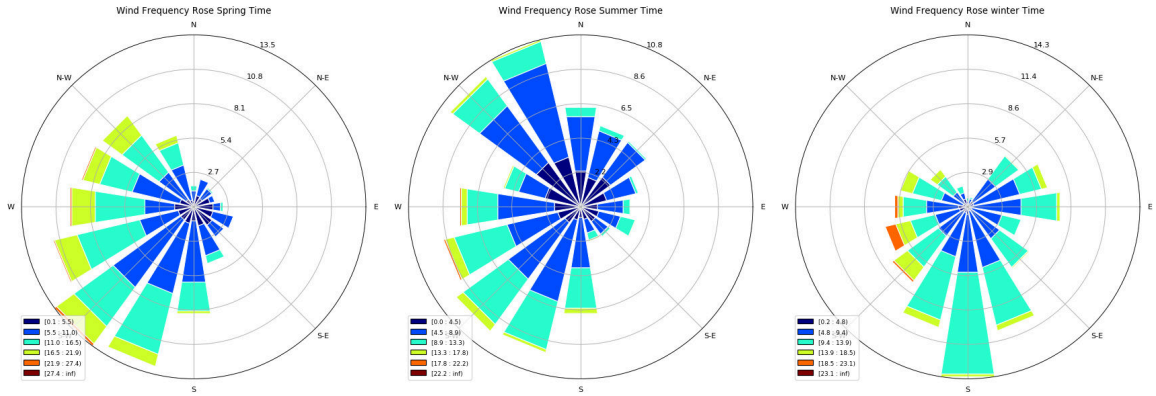

Figure 4.2: Wind rose for spring, summer and winter three seasons from SCADAR observation.

4.3. Synoptic condition of each Case Study modeled in WRF

In this section, the synoptic conditions for the simulated flow cases are presented to have an overview of the weather patterns during the selected epochs. This will help to better read the wind condition time series and analysis in the next chapter.

4.3.1. Synoptic condition 2018-08-18, Flow Case 1: 240°-Summer

By looking at the synoptic maps (Fig 4.3) of case 2018-08-18, a warm front can be observed moving towards to the Netherlands from the English Channel during the morning transition time (since 6:00 UTC). This is very likely to be the reason for wind speed ramp down around 9:00 UTC since a similar situation also exists at the case 2018-10-08.

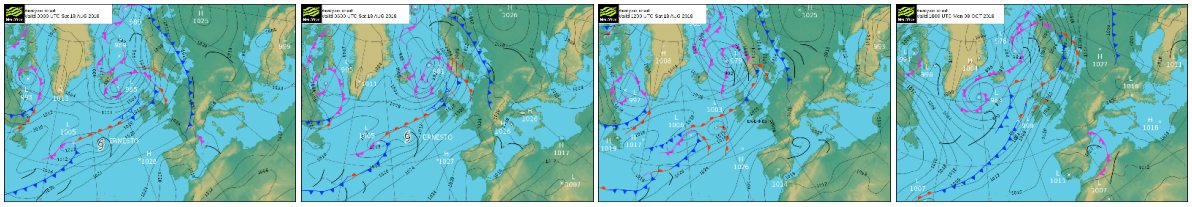

Figure 4.3: Synoptic maps for Case study 2018-08-18.

4.3.2. Synoptic condition 2018-09-11, Flow Case 2: 240°-Autumn

As it is shown on the synoptic maps of 2018 Sep 11st, there is a wide range of cold front continuously moving from British island towards mainland Europe. In the early morning around 6:00 UTC, a warm front was passing by the lake Ijsselmeer with this cold front chasing behind. This cold front reached the Dutch coast at midday around 12:00 (UTC). During this period, we have the highest wind speed of that day. Meanwhile, a distinct local maxima wind speed around 500m can be readily identified from the time-height plot of that day.

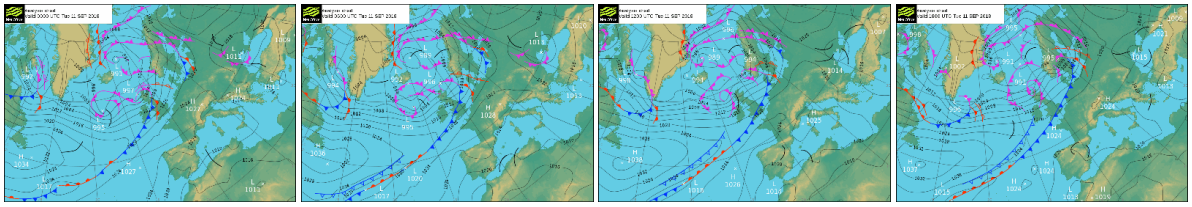

Figure 4.4: Synoptic maps for Case study 2018-09-11.

4.3.3. Synoptic condition 2018-10-08, Flow Case 3: 240°-Autumn

For the flow case 2018 Oct 8th, we have a very similar pattern of synoptic maps with the flow case 2018 Aug 18th, a warm front is moving towards to Dutch coast during the early morning with a cold front chasing behind, thus forming of an occluded front at the north part of Europe. It seems that the wind speed ramp down happened around 9:00 UTC is due to the passing warm front.

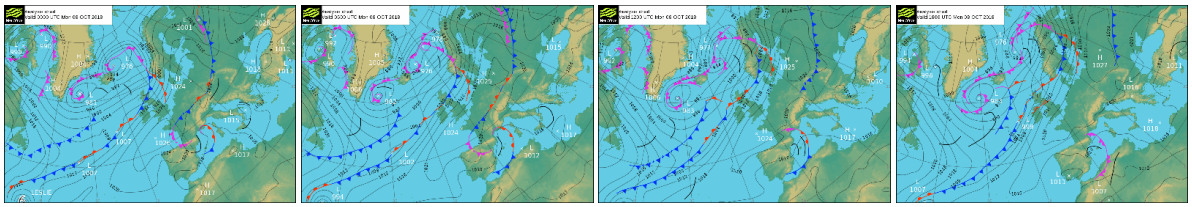

Figure 4.5: Synoptic maps for Case study 2018-10-08.

4.3.4. Synoptic condition 2018-10-11, Flow Case 4: 160°-Autumn

During the case 2018 Oct 11st, the dominant wind direction is around 160 degrees originally from the southeast towards the North sea. An occluded front is gradually moving Northward, and it passed our research domain after the midday. In correspondence, a substantial fluctuation of wind speed can be observed before the midday. It peaked at around 9:00 UTC in the morning with a 20m/s speed on the water site location.

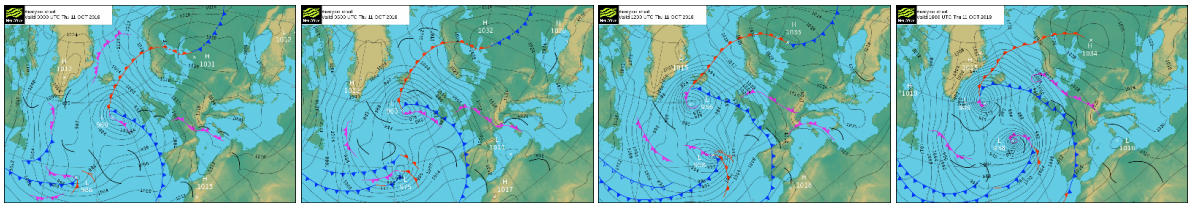

Figure 4.6: Synoptic maps for Case study 2018-10-11.

4.3.5. Synoptic condition 2018-11-30, Flow Case 5: 240°-Winter

A typical Icelandic low developed between Iceland and southern Greenland. It is a relatively common synoptic condition during the North Hemisphere winter. During this period, a vigorous area of low pressure is pushing the cloud and rain into the UK. As for our researching domain, there were not many places covered with fronts. Thus a clear sky with minor cover of clouds are reported.

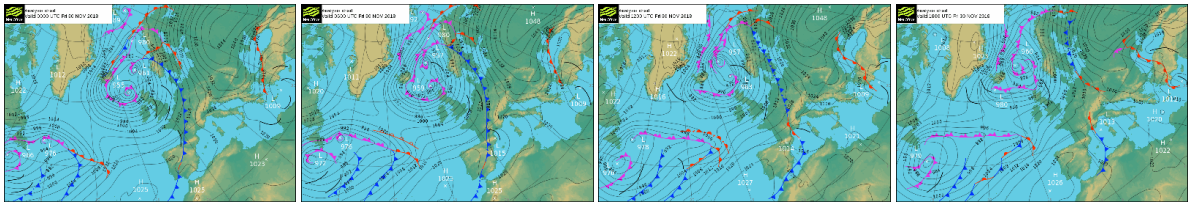

Figure 4.7: Synoptic maps for Case study 2018-11-30.

4.3.6. Synoptic condition 2018-12-10, Flow Case 6: 320°-Winter

A high-pressure zone developed around the Greenland Sea and relatively low pressure among the European continent resulted in the sea breeze to Dutch coastal. The wind direction during this flow case is around 330 degrees from the North Sea to the southeast. As it passes a spacious ocean, extremely wet air is carried with the flow and occlude fronts formed when it reached the land. A typical windy and rainy Dutch winter weather are experienced according to the historical weather of that day.

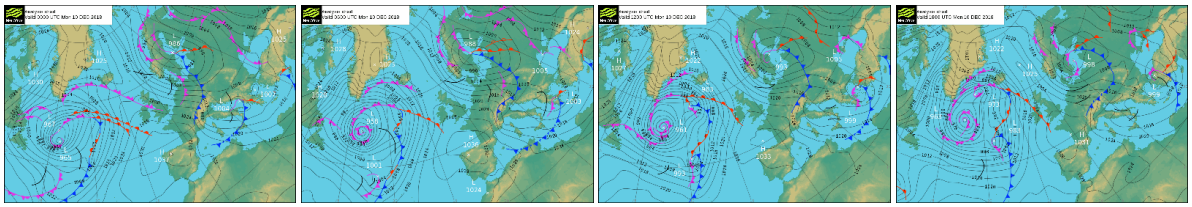

Figure 4.8: Synoptic maps for Case study 2018-12-10.

4.3.7. Synoptic condition 2018-12-26, Flow Case 7: 240°-Winter

The synoptic map is quite chaotic in the flow case 2018-12-26, with different fronts meandering all around the dutch coast. Cascaded cold fronts and warm fronts moving towards opposite directions and occluded fronts formed up the synoptic map of that day. A distinct indication of the weather condition over our study domain is the warm front moving northeasterly, which resembles the wind direction observed that day.

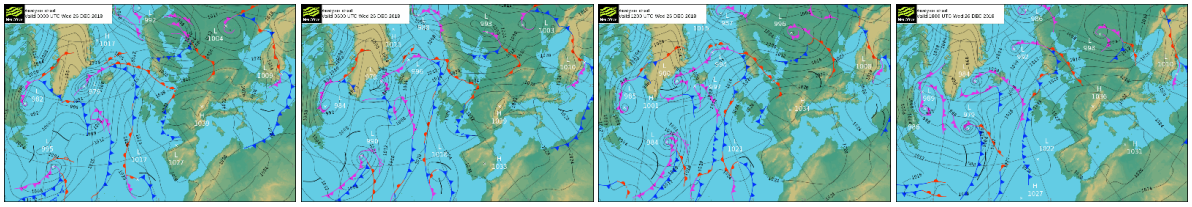

Figure 4.9: Synoptic maps for Case study 2018-12-26.

5

Results

5.1. General statistics

In this chapter, the WRF performance, as well as NEWA reanalysis data, are evaluated against the SCADAR observations. The timestamp of SCADAR is converted to UTC. Meanwhile, it is corrected depending on whether Daylight Saving Time is used during the selected epochs. In each flow case, the time series of wind speed and wind direction from models (WRF, NEWA) and observations (SCADAR) is shown in combined panels to detect the deviation visually, and correlation coefficient R as well as the root mean square errors $RMSE$ will also be reported in the figures. The time height plots are selected from the mast and virtual mast locations (fig 5.1) as a representative of an overall flow condition for that epoch. To better understand the chosen cases, interpretations are drawn combined with the synoptic conditions described in the previous chapter. A closure is induced from error analysis of normalized wind speed scatter plots with reported of RMSE for each site and all the flow cases.

5.1.1. Site layout

In order to make the SCADAR observations and WRF model results comparable, the WRF grid points are selected to be the closest grid points to the SCADAR reconstruction points. Filtering is applied to avoid considerable distances between the pair of WRF grid points and reconstruction points due to the usage of 1km resolution of WRF is not subtle enough. The site layout and cup information will be shown in the following figure 5.1 and table 5.1.

Table 5.1: Cup information

SCADAR RS position	Coordinates (LON,LAT)	WRF GP (I,J)	AGL Height (m)
Mast (low)	(5.5748 , 52.5940)	(97 , 66)	138.74
Virtual Mast (low)	(5.5619 , 52.6025)	(96 , 67)	138.74
BU06	(5.5747 , 52.6014)	(97 , 67)	168.87
BU11	(5.6242 , 52.6097)	(100 , 68)	418.34
BU20	(5.5808 , 52.6117)	(97 , 68)	251.83
BU21	(5.5907 , 52.6134)	(98 , 68)	297.17
BU24	(5.6206 , 52.6184)	(100 , 69)	441.10

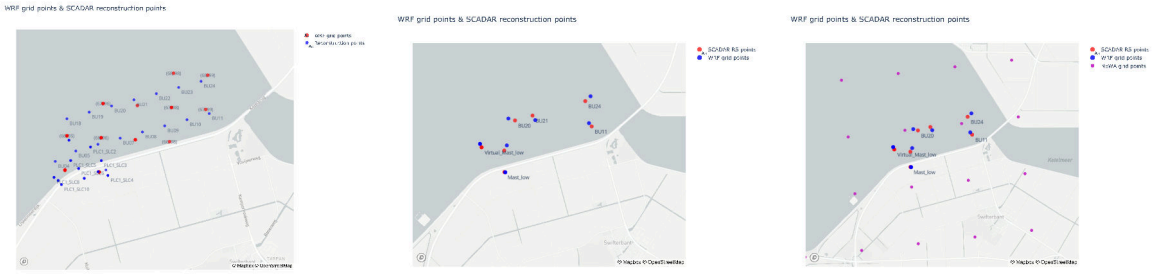

Figure 5.1: Left: Original site layout of WRF gird points and SCADAR reconstruction points. Center: Site layout after filtered out considerable distances. Right: Site layout after NEWA grid points are added.

5.1.2. Time series for wind speed & wind direction

Case study 2018-08-18

On the morning of flow case 2018-08-18, mainly three locations from the southwest part of the researching domain experienced a sudden drop of wind speed around 9:00 UTC (fig 5.3). The wind speed decresed from 12m/s to 6m/s in less than 1 hour and maintained a low wind speed around 8m/s with minimal fluctuations for the rest of that day. The WRF simulation results roughly agree with the SCADAR observations with a little bit overestimation at the morning peak time, while the NEWA underestimates the peak wind speed in the early morning at the closest grid point. The SCADAR observation has also captured a small fluctuation around evening transition time (19:00 UTC), the wind speed drops about 2m/s from the SCADAR observations, while the WRF prediction shows an opposite uptick with a bit smaller magnitude during that time.

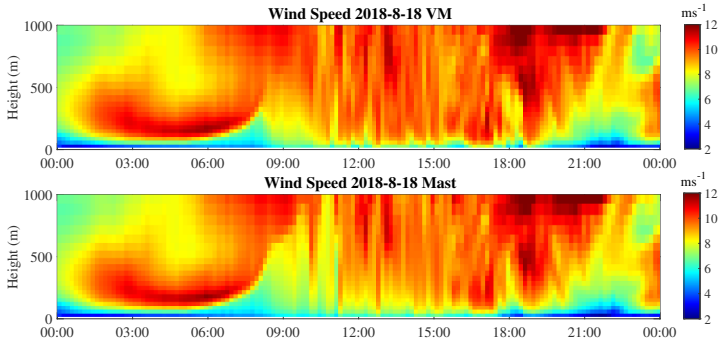

Figure 5.2: WRF prediction of wind speed during flow case 2018-08-18.

Before the morning transition, a Low-level jet can be observed around 100m above ground (Fig 5.2). After sunrise, the boundary layer started mixing and growing during the daytime. The SCADAR observation has also captured an around 30° slight anti-clockwise shifting of wind direction around 7:00 AM, which roughly agrees with the synoptic map as the shifting of wind direction is commonly observed with the passage of a warm front. However, the WRF model somehow also predicted this wind speed drop-down but without realizing the wind direction adjustment. Moreover, the effect of coastal orographic is noticeable if we investigate those traces with grouping them by distance from our anchor point, in this case, the mast location. We can see that the top three kernels, which representing the Mast, Virtual Mast, and BU06 locations (site map see Fig 5.1), are showing a similar overall trend. As it moves further from the anchor point, the next two sites, BU20 and BU21, show a more flattened wind speed than the former three sites with a much lower high wind speed before 6:00 AM (approximately 2 m/s lower than mast location). As for the two positions closest to the funnel-shaped junction of the land, NEWA incorrectly predicted to have spurts for BU11 and BU24 at that time (Fig 5.3).

Overall, the LiDAR observation agrees well with the WRF simulation results in flow case 2018-08-18. The most significant deviation occurs at the evening transition time (around 6:00 PM). For the results from NEWA, discrepancies are considerably higher since the spatial resolution is too coarse, which cannot reflect a decent comparison between the SCADAR reconstruction points and the NEWA grid points. However, it can be referred to as a datum line to make the performance of WRF readily examined.

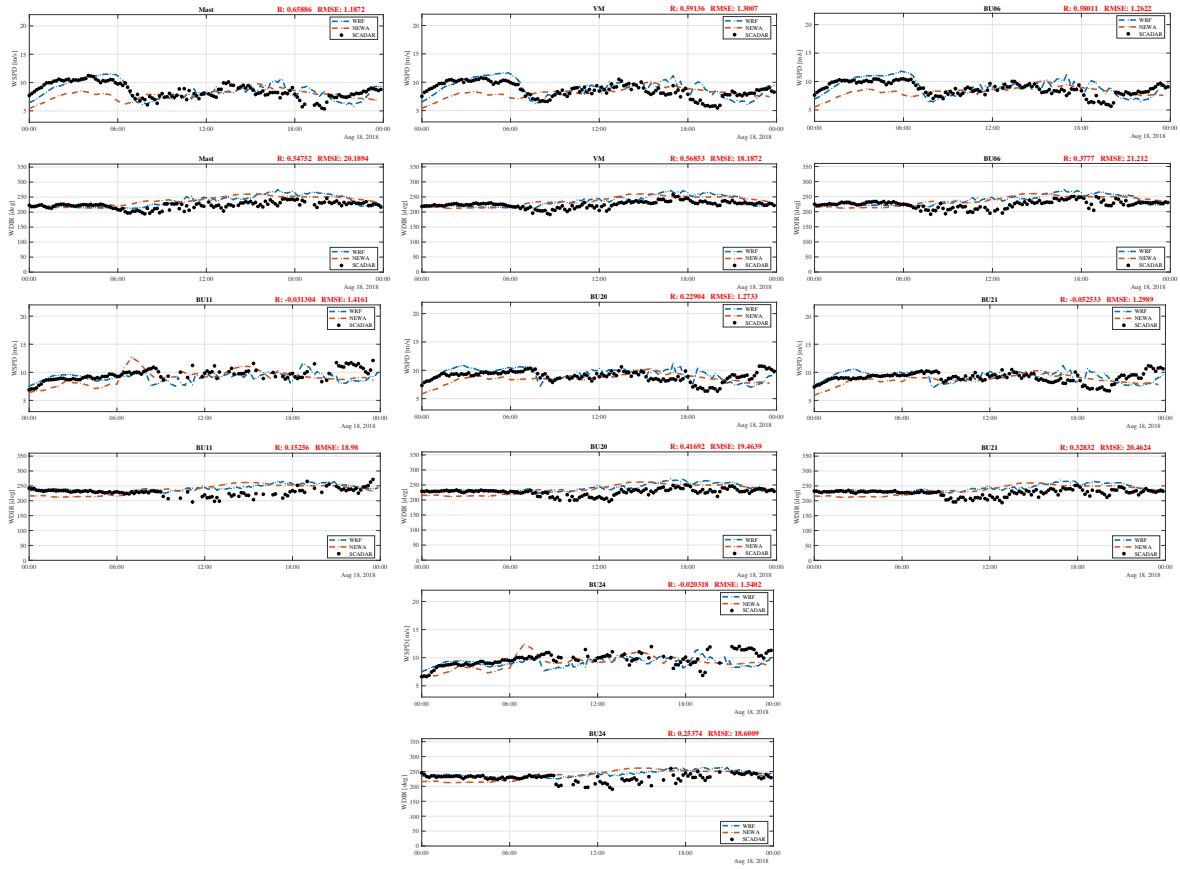

Figure 5.3: Wind speed & direction time series for 7 locations in case 2018-08-18.

Case study 2018-09-11

For the flow case 2018-09-11, WRF simulation results have shown a rapid shift of wind direction around 20:00 UTC, while this shift captured by SCADAR observations is a few hours delayed around 23:00 UTC compared with WRF prediction (fig 5.7). However, the magnitudes of them are comparable. Meanwhile, the wind speed dropped down to less than 4m/s, which is almost the minimum wind speed that can be observed by SCADAR. Surprisingly, in this flow case, NEWA have shown a better overlap with our observations, but it failed to predict the ramp down at the end of that day. Also, the wind direction shifting cannot be seen from the NEWA results. It seems a front is moving faster in the WRF simulation results than our SCADAR observations, while the NEWA did not realize the passage of the cold front. It is also uncommon to see that this flow case's highest wind speed took place at midday. Since the cold front just happened to pass the research domain at that time, the LLJ seen from the time height plot 5.4 is very likely to be a Frontal Low Level Jet (FLLJ) jet.

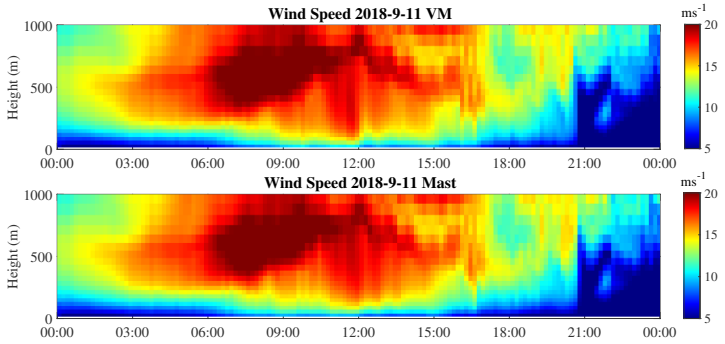

Figure 5.4: WRF prediction of wind speed during flow case 2018-09-11.

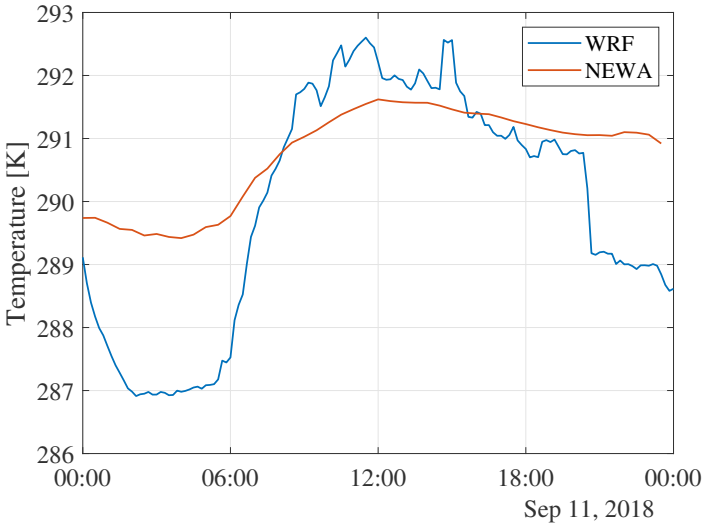

Figure 5.5: Temperature at 2m height for WRF and NEWA

In Fig 5.4, a stable stratification has lasted almost the whole day on the waterside, the reversed Obkhove length L reported in NEWA data is about 0.005 $1/m$. The passage of a front predicted by WRF occurs around 21:00 UTC. At the same time, the wind speed ramps down for approximately 5m/s in minutes. Hereafter, the wind speed remains low till the end of that simulation. Correspondingly, the sea surface temperature predicted by WRF drops simultaneously (Fig 5.5), which also proves that the shifting of wind direction and ramp down of wind speed could be triggered by passing by a cold front predicted in WRF. The historical weather recorded a mostly cloudy condition during the daytime. The synoptic maps also reflect a cold front has been covering the study area at the beginning of that day. Therefore it is consensus to conclude that the FLLJ is the cause of the high wind speed during the daytime and the ramp down in the evening.

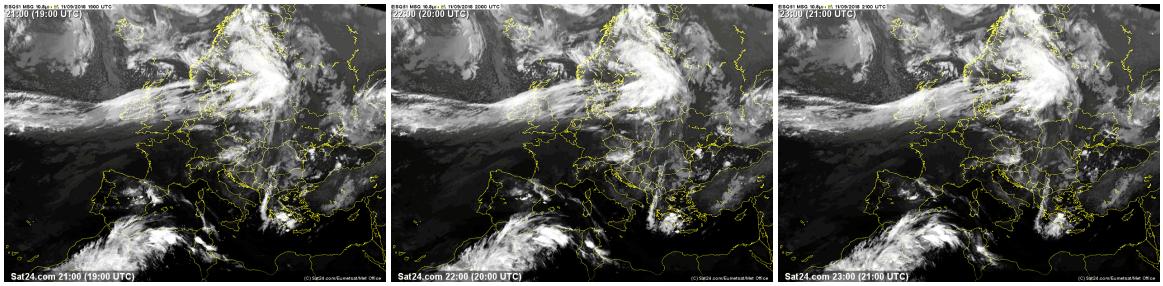

Figure 5.6: Satellite image for the passing cold front at Sep 11st evening.

If we check on the satellite image at that corresponded time (Fig 5.6), the white air mass appeared over our interested domain around 19:00 UTC, which is 2 hours earlier than the sea surface temperature observed dropping down. It was continuously moving eastward and dissipating till it fully reached Germany at 21:00 UTC. The adjustment of wind direction from 240 degrees to 300 degrees seeing from the traces Fig 5.7 happened to match the moving direction of the air mass.

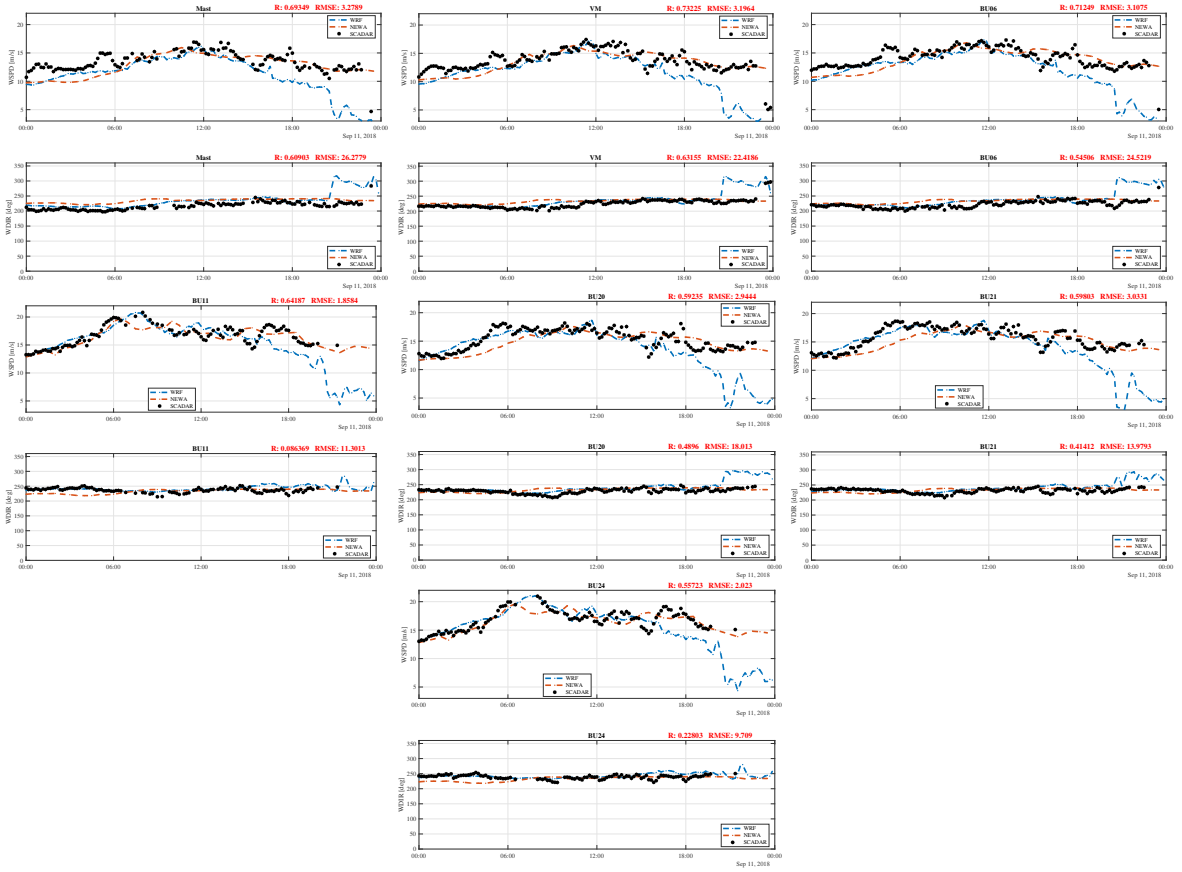

Figure 5.7: Wind speed & direction time series for 7 locations in case 2018-09-11.

Although the considerable shift of wind direction and ramp-down wind speed predicted by WRF occurred till 21:00 UTC, the deviation between the WRF and SCADAR observation had taken place three hours earlier. Seeing from Fig 5.7, the WRF simulated wind speed went down steeply and separated from the SCADAR observation, while the other two traces remain higher but declining slowly. As for earlier that day, both the WRF and NEWA prediction agrees with the observations very well.

Case study 2018-10-08

In the flow case 2018-10-08, a similar but less significant low-level jet can be noticed compared with the flow case 2018-08-18. They both developed during the nighttime and peaked in the early morning. As time passes by, the elevation of local maxima wind speed on the Mast location continuously rarised from 6:00 UTC to 12:00 UTC (Fig 5.8). On the other hand, the elevation of local maxima wind speed at the Virtual Mast location remained around the hub height, which denotes an approximate 2m/s wind speed gradients around the hub height taken place at that time.

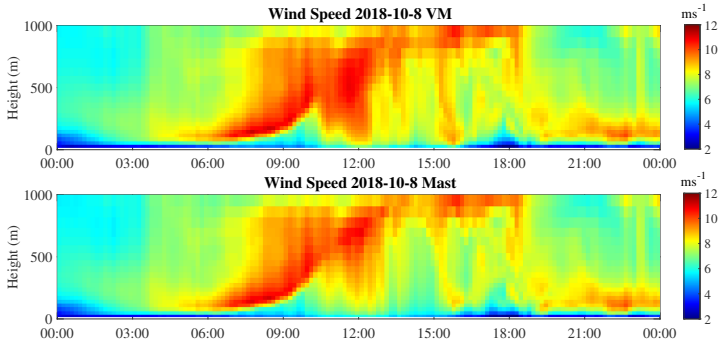

Figure 5.8: WRF prediction of wind speed during flow case 2018-10-08.

The wind trace for this case (Fig 5.9) is considerably similar to the flow case of 2018-08-18 with the wind speed peaked in the morning around 9:00 UTC, then it dropped down and tended to be flattened for the rest of the day. While the NEWA prediction failed to predict the peak time in the morning due to its coarser resolution, both the WRF and NEWA could not reproduce the uptick event around 17:00 UTC captured by SCADAR observation. The PBL parameterization for the WRF YSU scheme seems to have flaws with simulating evening transition time since the former three described cases are all showing that the most significant deviation between the model and the observation take place at evening transition time.

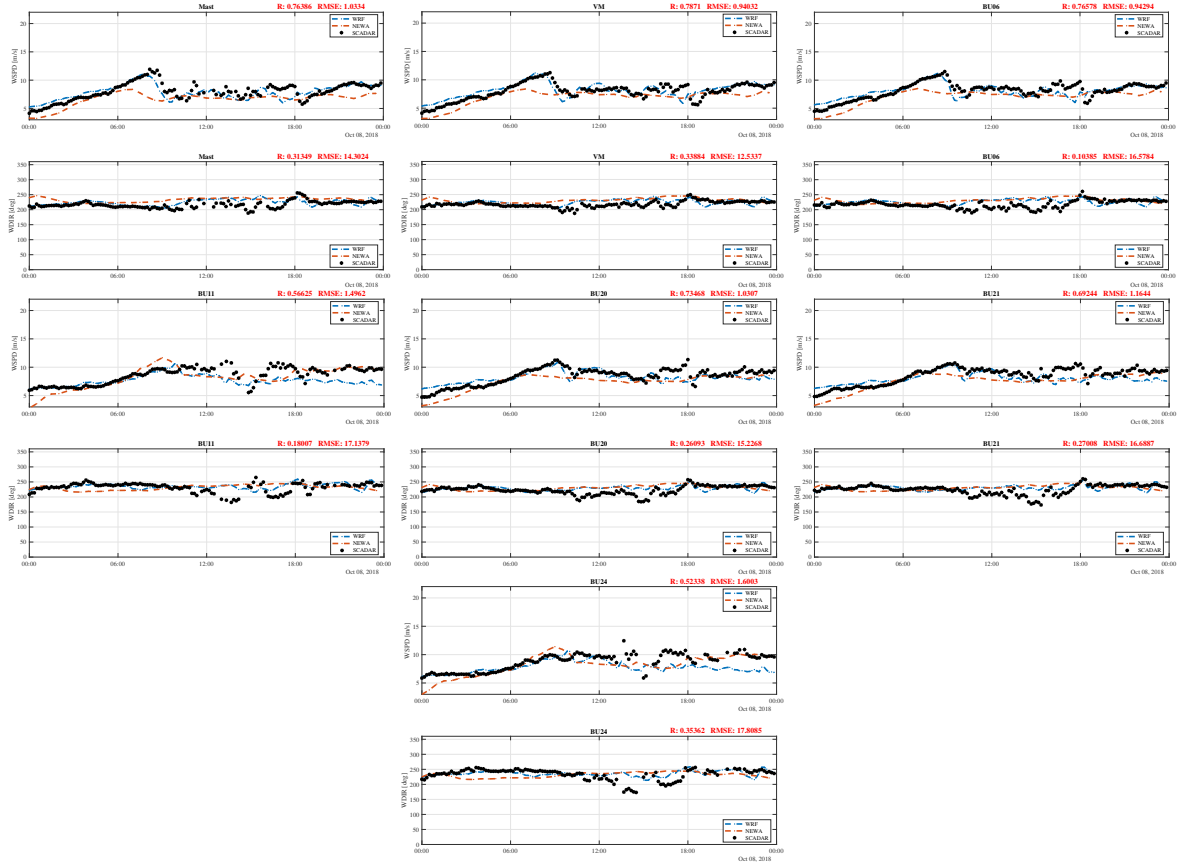

Figure 5.9: Wind speed & direction time series for 7 locations in case 2018-10-08.

Case study 2018-10-11

For the flow case 2018-10-11, the wind direction is roughly within 150 degrees to 180 degrees, which denotes the sector that flow condition moves from onshore to offshore. See from the time height plot Fig 5.10, the differences between the Mast location and the Virtual Mast location can barely be seen within this small fetch at around hub height. The effectiveness of the surface discontinuity seems to be weakened as a more significant difference is expected between two sites in this wind sector.

In general, the wind speed for flow case 2018-10-11 shows very substantial fluctuation if the whole day time series is investigated (Fig 5.11). Meanwhile, the site location effect is rather obvious than in other cases. Significant differences can be observed if different locations are compared during this case. For those grid points closer to the SCADAR location, a shorter acceleration is experienced during the morning peak time, i.e., for Mast, Virtual Mast, and BU06 reached a top wind speed at 14m/s. However, for BU20 and BU21, it reached 18m/s at the same time, as the peak wind speed predicted by WRF is about 2m/s slower than the observation. Moreover, the peak wind speed in the morning predicted by the WRF is about dozens of minutes delayed from the SCADAR observations. The WRF simulation did a better job in this case as usual since the NEWA did not predict the peak wind speed in the morning at all. As the site location went further at BU11 and BU24, we missed nearly one-third of our observations due to the limitation of data availability. Overall, the prediction of case 2018-10-11 is fairly reliable for both wind speed and wind direction. However, the results are not as well correlated with observation as the previous alongshore flow cases. The main imperfection

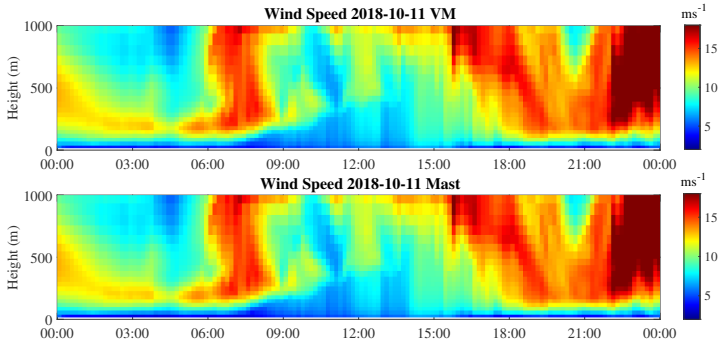

Figure 5.10: WRF prediction of wind speed during flow case 2018-10-11.

is that the peak time-shifting in the morning, setting a longer simulation time, and giving the WRF model a warm-up period might be a solution to this imprecision.

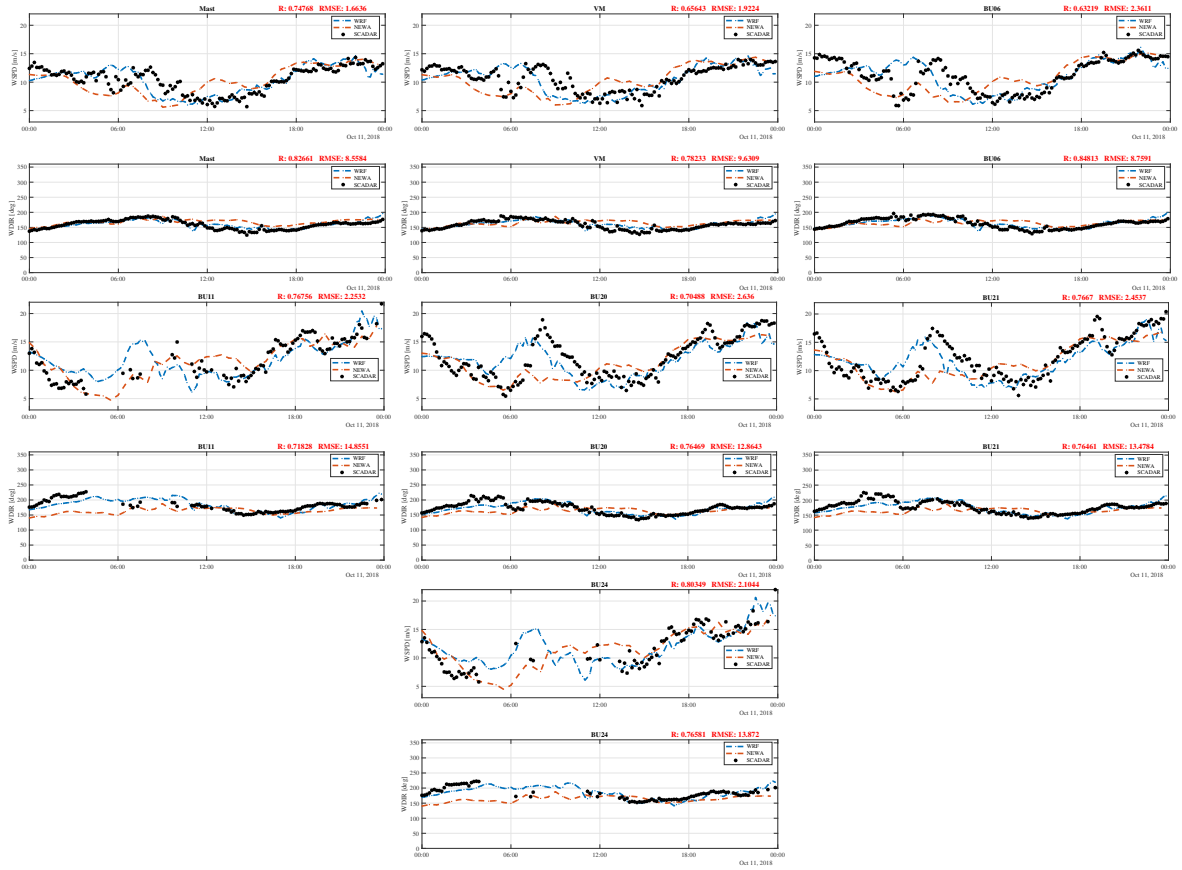

Figure 5.11: Wind speed & direction time series for 7 locations in case 2018-10-11.

Case study 2018-11-30

See from the time height plot Fig 5.12, a FLLJ developed before the start of the simulation. Comparing with the synoptic map Fig 4.7, a widespread cold front has already passed the study domain in the early morning, which corresponds with the occurring time of the LLJ predicted by WRF. It lasted until midday 12:00 UTC and almost entirely disappeared for the rest of that simulation. The synoptic map also reflects the supportive pattern as the cold front was moving fast, and eventually left our domain by that time.

In this flow case, both the WRF and NEWA did very well in predicting the time series, as there are barely very substantial fluctuations that appeared in the traces. Meanwhile, the wind speed remained high for almost the whole day due to the intense cold front passage. See from the top three kernels, which represents the closer sites to the SCADAR location. The most significant deviation occurs around 19:00 UTC. The observations are showing an uptick within this evening transition epoch. On the other hand, WRF are showing an

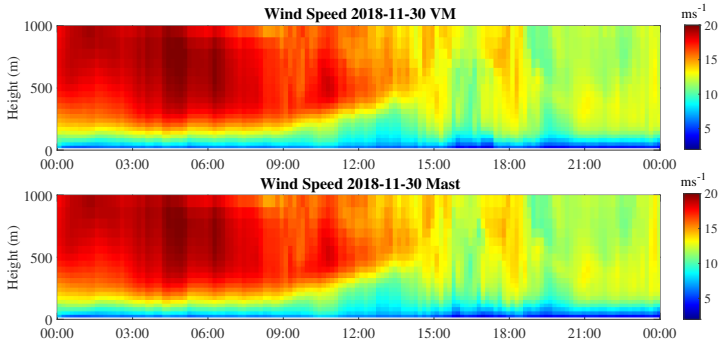

Figure 5.12: WRF prediction of wind speed during flow case 2018-11-30.

opposite downtick at that time. Since the temporal resolution of NEWA is 30-min, which is coarser than the other two sources, it did not catch any fluctuation within this period. Regard those distant sites, at site BU20 and BU21, WRF underestimated the wind speed for about 2m/s during the time from 16:00 UTC to 20:00 UTC. NEWA overestimated it for half of that day at site BU11 and BU24 while they are compared with the same gird point from NEWA as the spatial resolution of NEWA is 3 km.

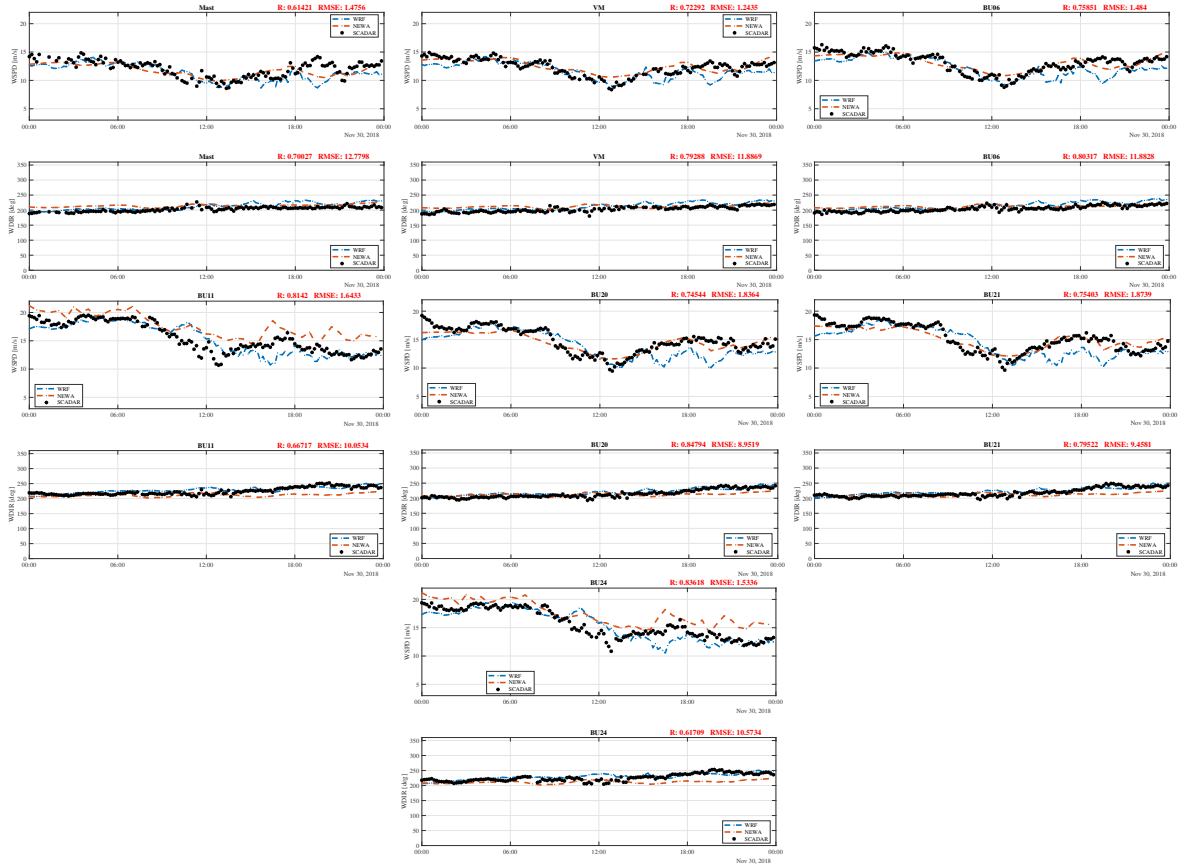

Figure 5.13: Wind speed & direction time series for 7 locations in case 2018-11-30.

Case study 2018-12-10

The wind direction for this flow case is around 330 degrees, which denotes a rare flow condition that forms in the winter at this latitude. It is common to have a sea breeze on the dutch coast during summertime between May and September. However, this flow condition triggered by a high-pressure zone at the Greenland Ocean provided an excellent case study opportunity. Relatively high wind speed lasted for the whole simulation, a monotonic vertical wind speed structure is showing on the time height plot Fig 5.14. Intense turbulences are expected as the minute fluctuations can be observed throughout the whole period.

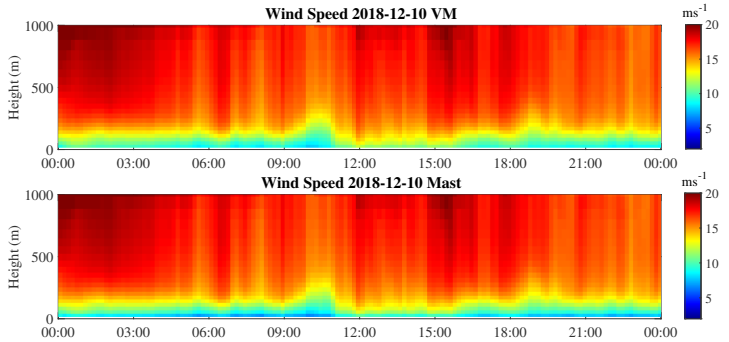

Figure 5.14: WRF prediction of wind speed during flow case 2018-12-10.

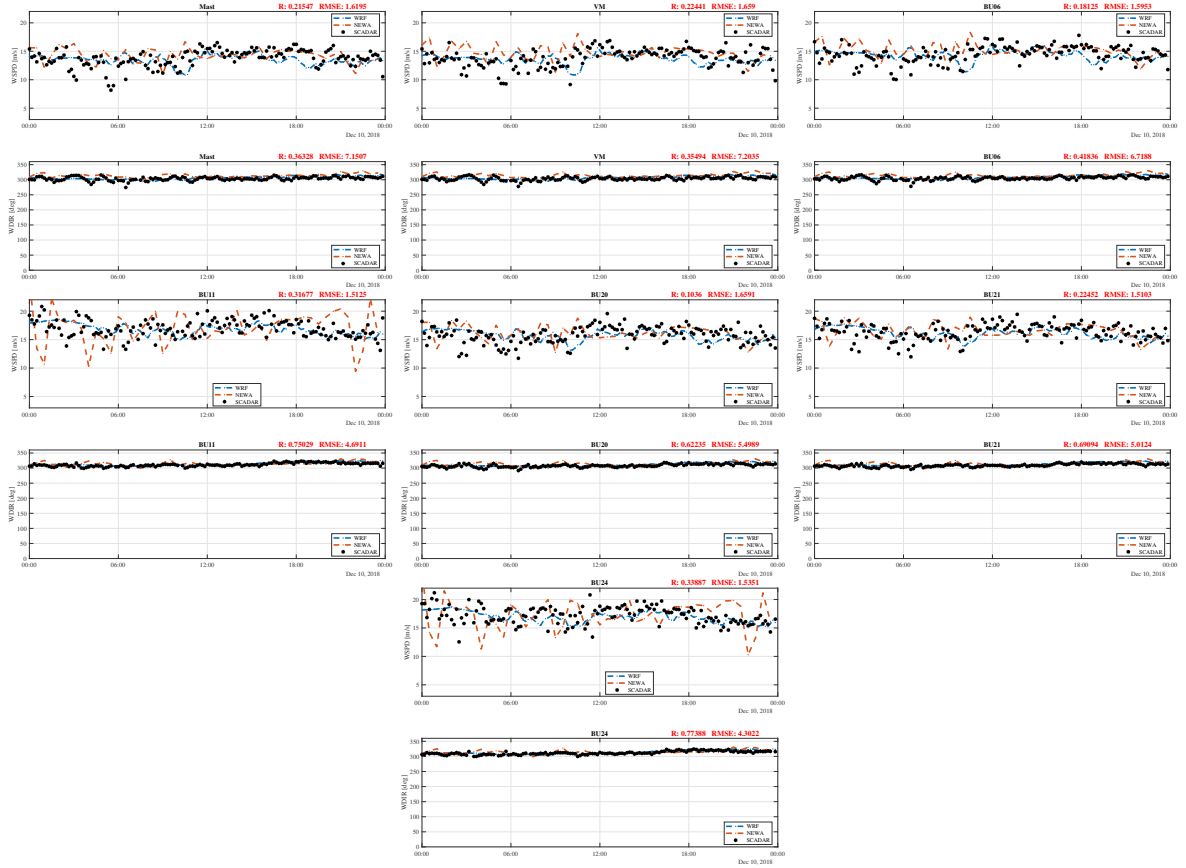

Figure 5.15: Wind speed & direction time series for 7 locations in case 2018-12-10.

See from the wind traces 5.15, both the WRF and the NEWA almost correctly predict the wind direction. However, as a tool of mesoscale modelling, they are not fully resolving all the fluctuations as the SCADAR observation does. It is safe to say that the simulation results from WRF are all distributed within the upper and lower limit drawn by the SCADAR observations. On the other hand, the results predicted by NEWA considerably exceeded the range intimated by the SCADAR observations. These should also be attributed to the improvement of the resolution within the possibilities of computational power. Unfortunately, the prediction of WRF almost lost all the correlation with the SCADAR observations, even the root mean square errors are not very significant but still within an acceptable range.

Case study 2018-12-26

Illustrated by the time height plot 5.16, a LLJ developed before the simulation started. It lasted a few hours then became weakened. Compared with the climatology of this region, the wind speed remained relatively low due to the passage of the warm front, even though it is a flow case selected in the winter. Additionally, a clear sign of the LLJ can be observed within the whole day despite its differences in magnitude.

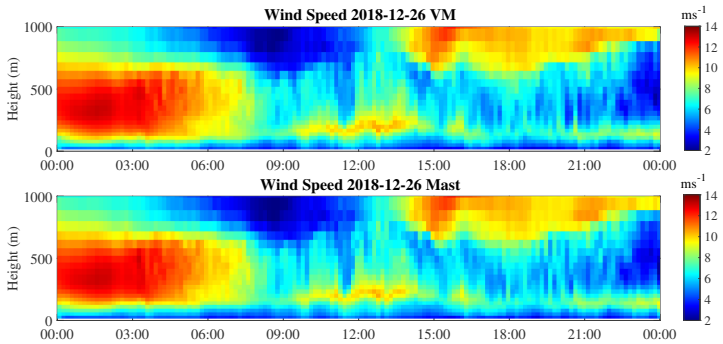

Figure 5.16: WRF prediction of wind speed during flow case 2018-12-26.

Since the data availability is inadequate for this flow case, nearly half of the predictions are lack of comparison with SCADAR observations. However, see from the existing patterns, the simulation results roughly agree with the observations except during the evening transition time. The SCADAR observed higher wind speeds during this period for those further sites, i.e., BU20 and BU21. As for the commonly gapped period from 6:00 UTC to 11:00 UTC, the WRF simulation shows a smaller magnitude than the NEWA prediction, which we can never confirm the decency from observed data. However, it does agree better with the WRF prediction seeing from the existing evidence at the margins of those time gaps.

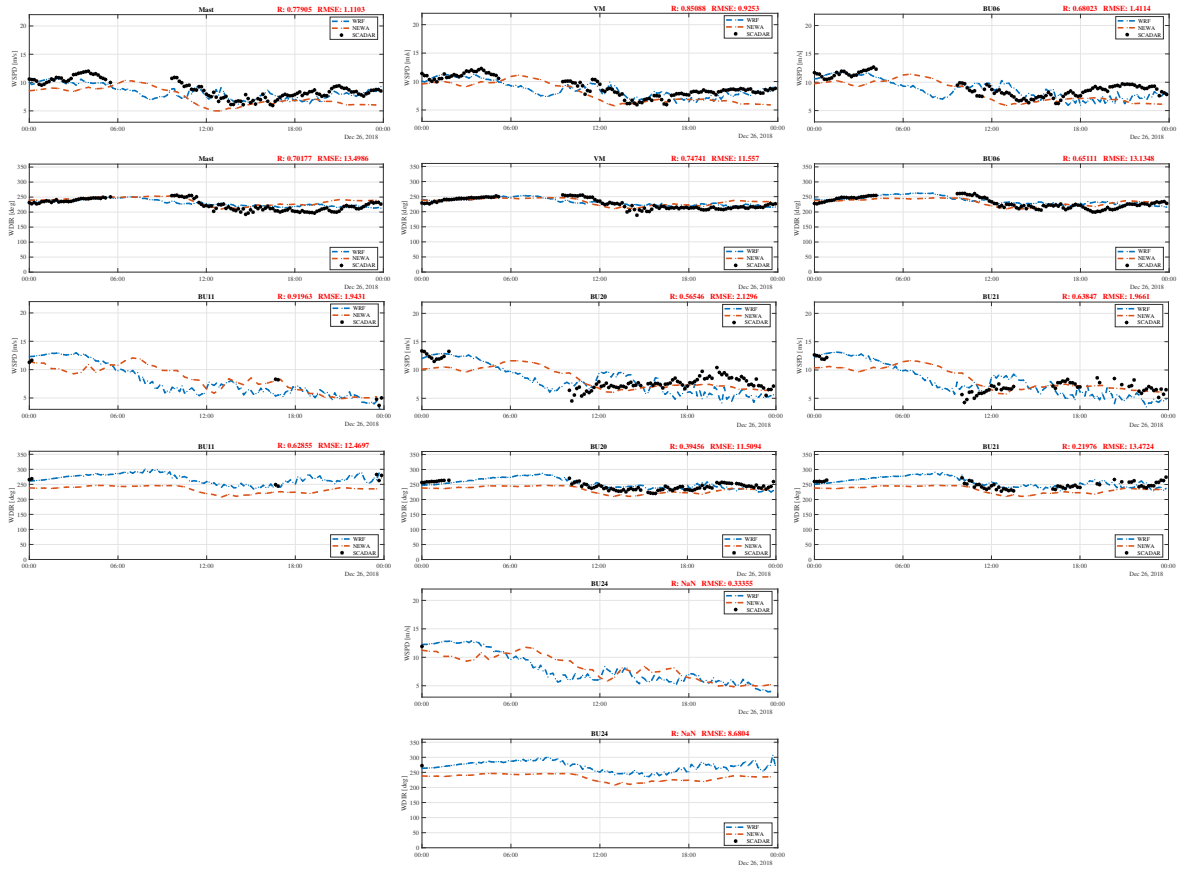

Figure 5.17: Wind speed & direction time series for 7 locations in case 2018-12-26.

5.1.3. Statistic & Errors

This section is showing the error of WRF and NEWA prediction in comparison to SCADAR. The normalization is done by dividing the values at Mast location for each time step, i.e., for the wind speed at Virtual Mast location, plot the normalized SCADAR observation at Virtual Mast $U_{VM}/U_{Mast}(SCADAR)$ against the WRF prediction at Virtual Mast $U_{VM}/U_{Mast}(WRF)$. Replicate it for each reconstruction point selected before and the same for the wind direction. Note that this normalization approach will not always applicable for the wind direction, since from a complete sample set, we will have wind direction of 0° which can not be used as the denominator. In our selected flow cases, there will be no samples with wind direction reaches 360°. The Root Mean Square Error (RMSE) for each reconstruction point is reported in the following table 5.2 for both wind speed and wind directions. The ratio is also further investigated to have an overview of the wind speed spatial gradient.

$$RMSE = \sqrt{\overline{\sum_{i=1}^{n}(m_i - o_i)^2}} \tag{5.1}$$

$$NRMSE = \frac{\sqrt{\overline{\sum_{i=1}^{n}(m_i - o_i)^2}}}{\bar{o}} \tag{5.2}$$

The RMSE for WRF predicted wind speed at reconstruction points are ranged between 1.7 m/s and 2.0 m/s, depends on the cup locations and sample sizes. On the other hand, the errors for the NEWA prediction is higher compared with WRF, the range for the absolute value of RMSE is 1.7 - 2.2m/s for wind speed and 15 - 20 deg for wind direction. It shows similar patterns for other types of RMSE analysis, as the WRF shows an overall smaller error compared with NEWA. In principle, the distant sites are expected to have more significant errors. However, the farthest sites BU11 and BU24 shows the smallest error, as many considerable deviations are lack of comparison due to the lower data availability. For the normalized wind speed, the Mast and Virtual mast ratio should approach 1, as they are measured at the same height. The SCADAR is scanning in a fixed elevation

Table 5.2: RMSE for wind speed and wind direction: The left panel is the RMSE calculated after each reconstruction point normalized with the Mast location. The right panel is the RMSE directly calculated on initial results.

		RMSE of ratio		RMSE		NRMSE
		WS [-]	WD [-]	WS [m/s]	WD [deg]	WS [-]
WRF	Mast	-	-	1.75	15.56	0.16
	Virtual Mast	0.0759	0.0338	1.77	14.23	0.16
	BU06	0.0931	0.0307	1.87	15.86	0.16
	BU20	0.1637	0.0523	2.02	13.91	0.16
	BU21	0.1714	0.0602	1.98	14.02	0.15
	BU11	0.1974	0.0724	1.70	13.41	0.12
	BU24	0.2009	0.0697	1.71	13.25	0.12
NEWA	Mast	-	-	1.85	16.70	0.17
	Virtual Mast	0.1213	0.0333	1.81	15.54	0.17
	BU06	0.1210	0.0349	1.82	15.80	0.16
	BU20	0.1794	0.0814	1.82	16.60	0.15
	BU21	0.2077	0.0894	1.78	17.62	0.14
	BU11	0.3191	0.1197	2.23	19.78	0.17
	BU24	0.3071	0.1241	2.11	20.39	0.16

back and forth. The measurements at farther reconstruction points are at higher levels. Therefore the ratio is growing with the distance between cup location and the mast location as the wind speed increases by height.

See from Fig 5.18, the wind speed ratio of U_{VM} and U_{Mast} are concentrated around 1. Those ratios are larger than one account for 66.65% non-null samples, which indicates a spatial gradient where the wind speed at the Virtual mast location is generally slightly larger than the mast location for at the same elevation, in this case, the hub height 140m. As it moves further from the mast location, the ratios will still rise. Unlike the ratio for Virtual Mast location caused by the spatial gradients over different surfaces, they are mainly triggered by the increasing measure heights as the wind speed generally growing logarithmically with height. Moreover, some of the flow cases, i.e., 2018-10-11 and 2018-12-26 show many samples spread below one at distant reconstruction points, which is a sharp indicator of existing LLJ around the hub height. As for the wind direction, see from Fig 5.19, ratios scattered around one is the common case for almost all the reconstruction points. As the measure heights increase, a maximum 35% shifting in the wind direction also presents in the offshore flow case 2018-10-11. It is also worth to mention that in the fig 5.21 the wind direction ratio for NEWA commonly gathered around 1 with less than 0.1 fluctuations. Unlike it is for the WRF and SCADAR, which are showing shifting in the wind direction as the site location changes. The reason is that for the NEWA data, all these six pairs compared gird points are from three grid points from the original dataset, except that they are interpolated at different height given by the level of the corresponding reconstruction points. It proves that the wind direction shifting within this study domain is mainly caused by the spatial distribution heterogeneity rather than the vertical adjusting of flow direction, which is on the contrary with the wind speed that more depends on the height instead of the grid location.

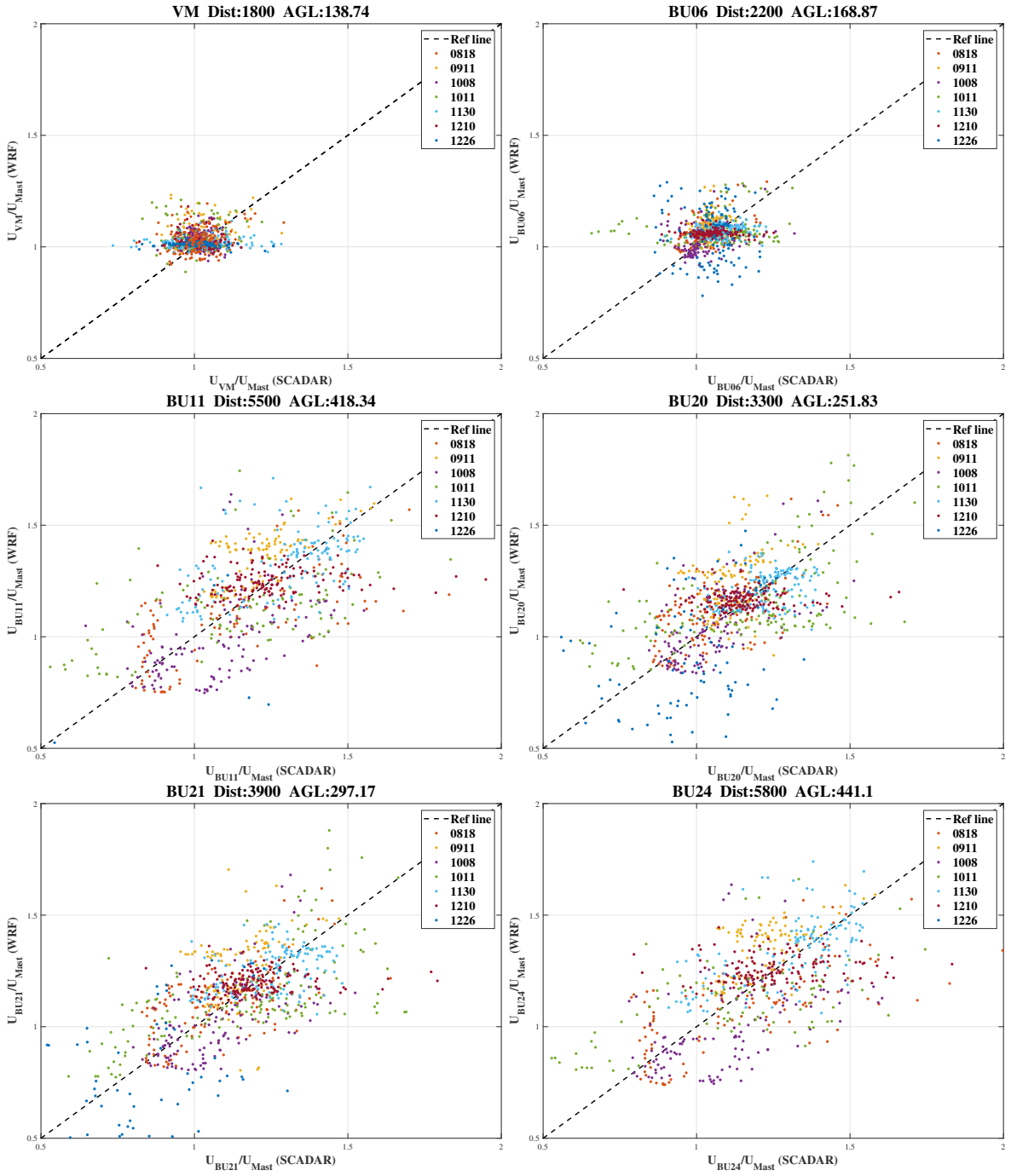

Figure 5.18: Scatter plot of normalized wind speed, WRF against SCADAR for each reconstruction point.

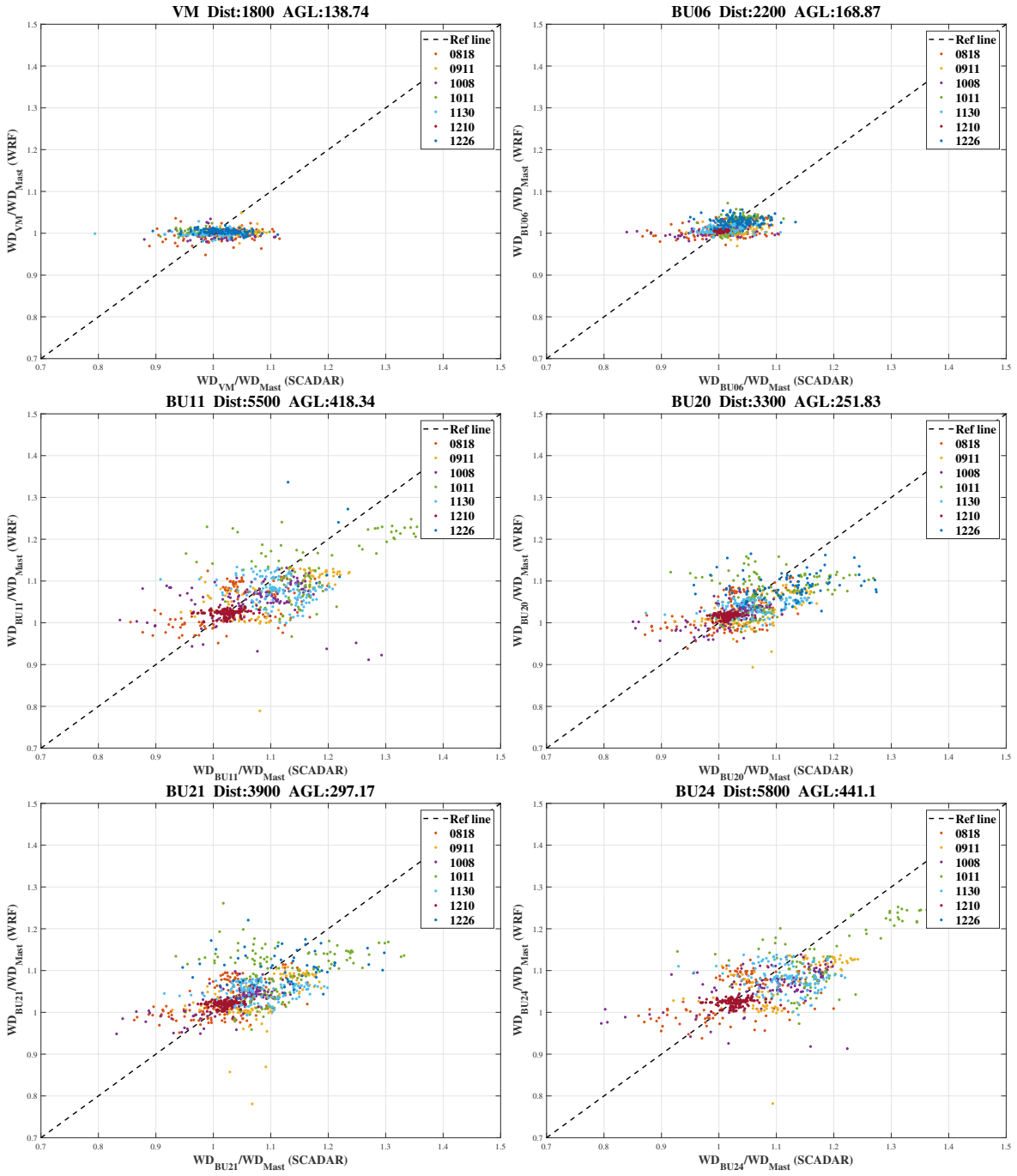

Figure 5.19: Scatter plot of normalized wind direction, WRF against SCADAR for each reconstruction point.

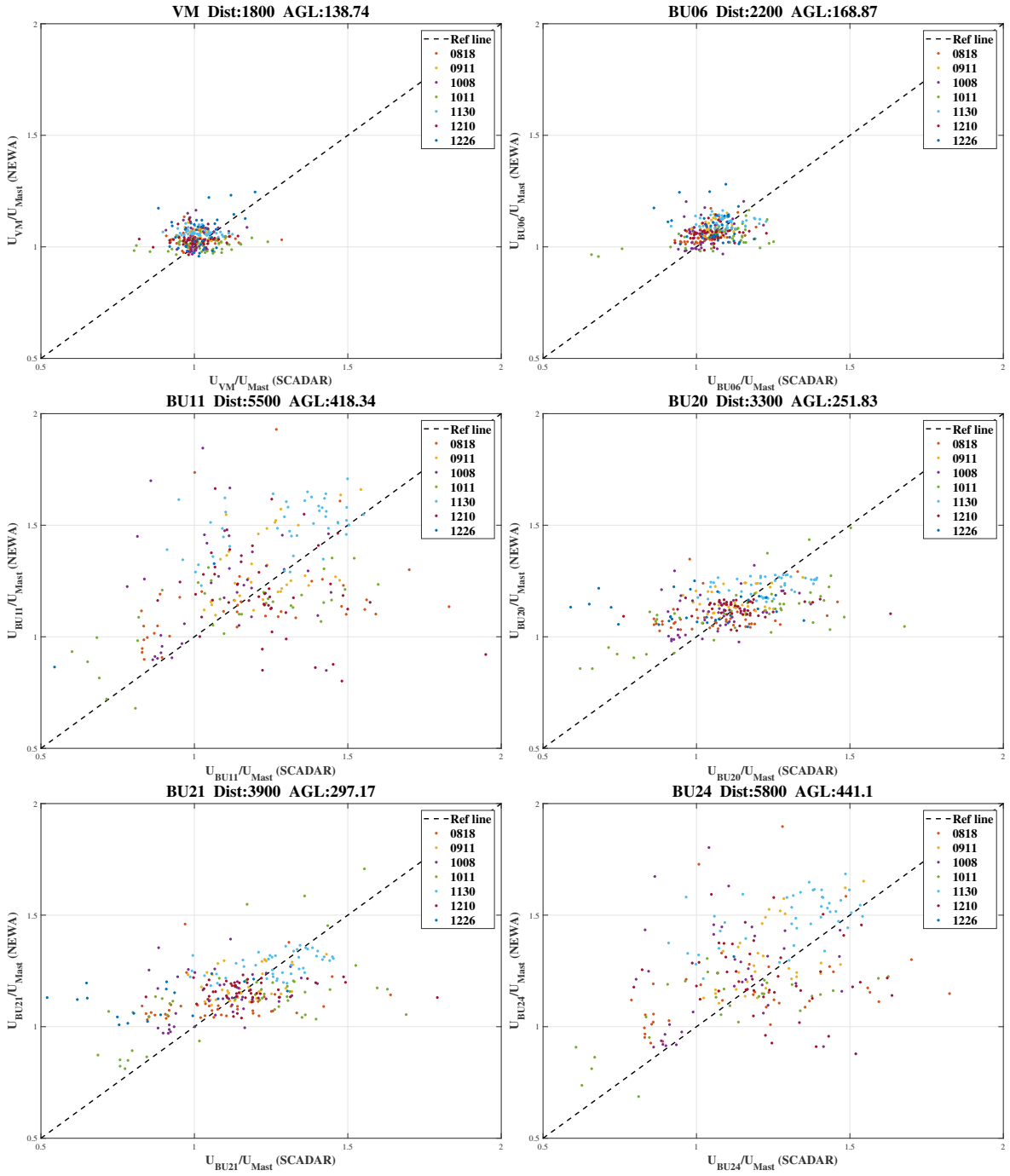

Figure 5.20: Scatter plot of normalized wind speed, NEWA against SCADAR for each reconstruction point.

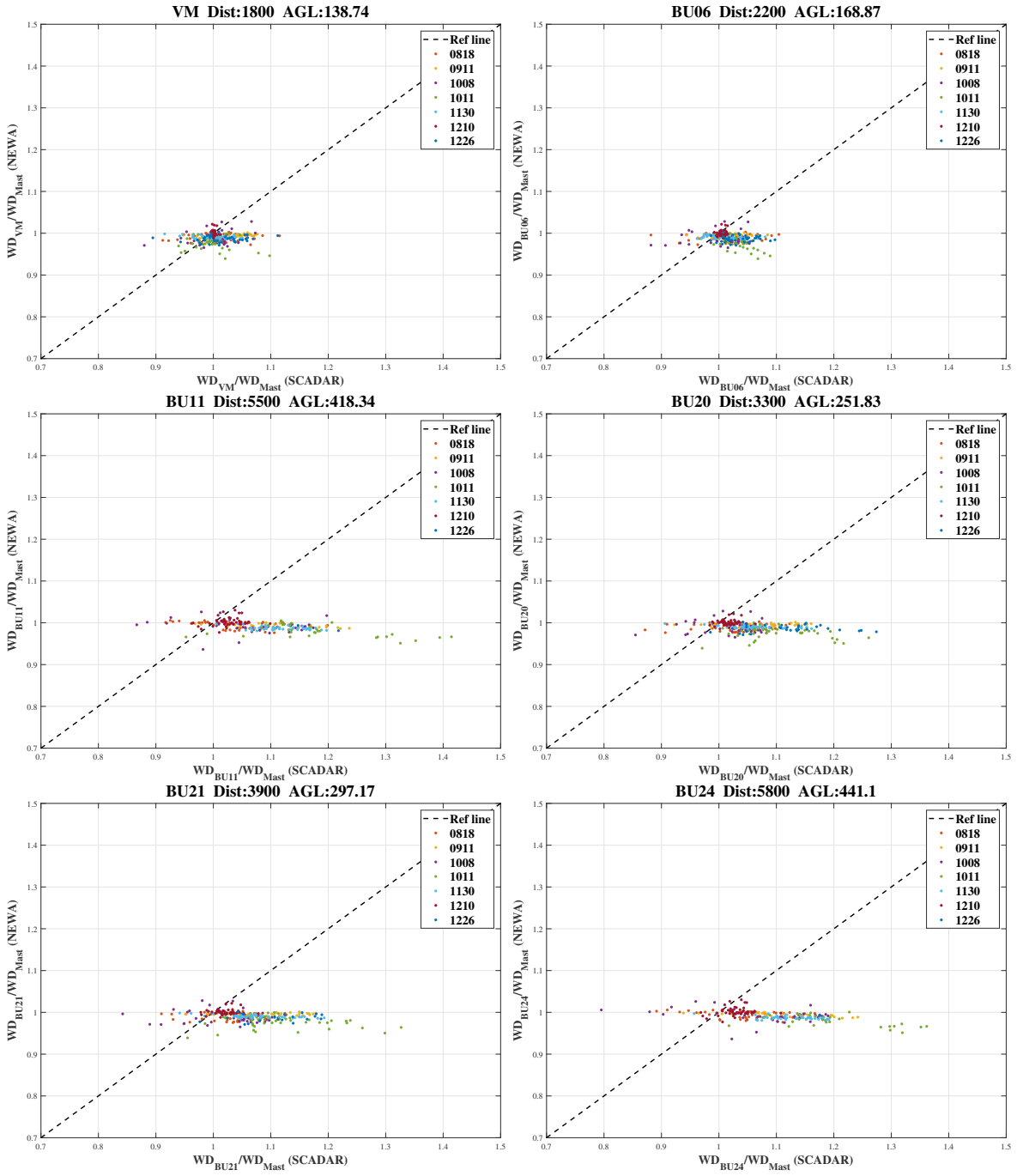

Figure 5.21: Scatter plot of normalized wind direction, NEWA against SCADAR for each reconstruction point.

5.2. Wind speed gradient

Fig 5.22 is showing below to obtain an overview of the horizontal wind speed gradient measured by SCADAR. The distance from Mast location to the Virtual Mast location is approximately 1400m. To avoid the biases on the model and SCADAR, the wind speed at the virtual mast location is normalized by dividing it to the wind speed at the mast location. A distribution of nondimensionalized wind speed at the Virtual mast location shows a preference of exceeding one within this small fetch. The red curve is the distribution fitted to a Laplace probability density function. It argues the same fact declared before that the ratio higher than one contributes to 65% of the entire dataset. However, based on the limited reconstruction points and the relatively small fetch, it is hard to define the wind speed gradients qualitatively. Hereafter, the WRF simulation results will be analyzed to extend the fetch further towards the offshore direction (northwest direction).

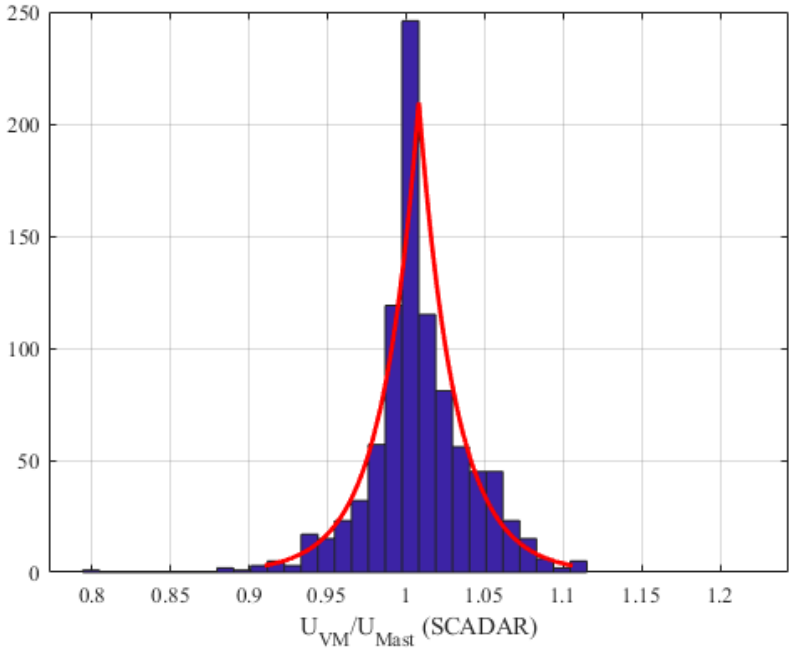

Figure 5.22: Histogram of wind speed ratio U_{VM}/U_{Mast} and fitted laplace distribution.

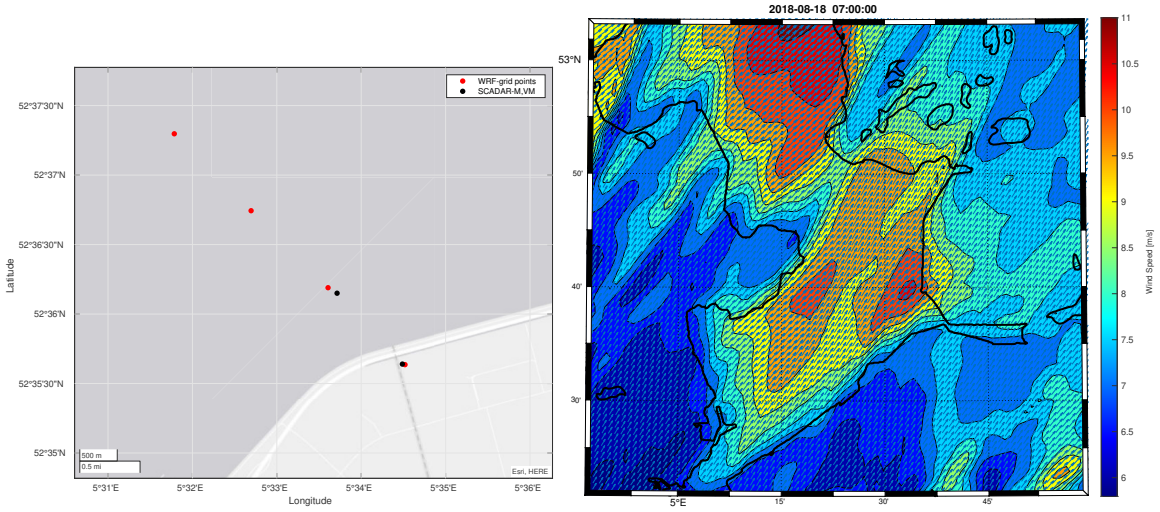

Figure 5.23: The left figure shows WRF grid points of 4 location for wind speed gradient analysis. The right figure is a snapshot example showing the wind speed gradient within study area at around hub height.

In order to get a qualitative estimate of how WRF are resolving the horizontal wind speed gradient, anal-

ysis is applied to investigate the wind speed gradient over the researching domain. Considering the Mast location and the Virtual mast location are the nearest two WRF grid points over a diagonal line, two extra grid points on this line are chosen to extend the grids further towards the waterside. See the following site layout map Fig 5.23, from bottom right to top left is in the order of Mast, Virtual mast, extended grid point 1, and extended grid point 2. The step size of WRF grids for domain 3 is 1km, hence the diagonal distance of two nearest locations is about 1.4 km. The wind speed gradient ratios are investigated given consideration of the flow direction sector (fig5.24), the atmospheric stability (fig 5.25), the time of the day (fig 5.27 as well as the fetch from the shoreline (fig 5.29, 5.28). An overall daily averaged wind speed profile for all the flow cases are also presented in flowing fig 5.26.

5.2.1. Gradient ratio by wind direction criteria

Fig 5.24 shows the bin-averaged wind speed ratios for different wind direction ranged from 120° to 320° covered within 7 simulated flow case. The sample size is larger at 200° and 260° as it is the predominant flow directions which are alongside the shoreline. The simulated wind speed ratios are also the largest (1.07) among this flow sector. The SCADAR observation shows the largest ratios (1.11) exist at 280° with very limited samples within this sector.

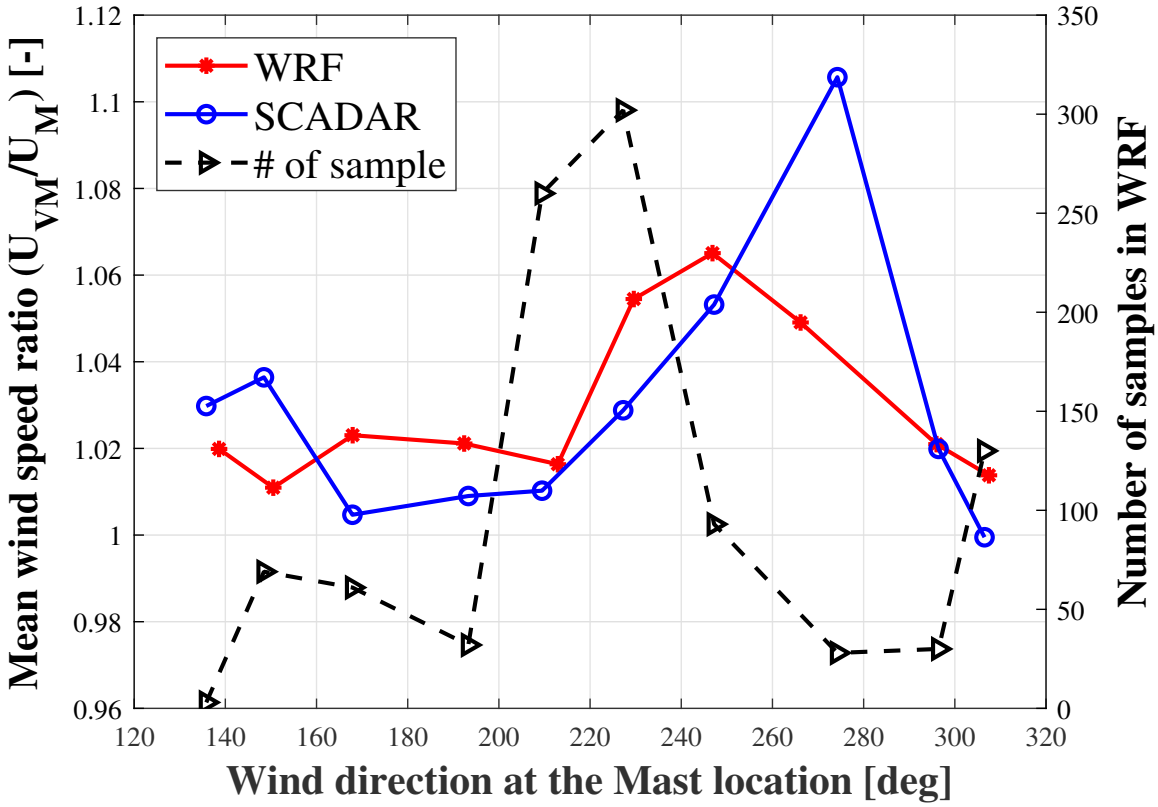

Figure 5.24: Bin-averaged wind speed ratios from the WRF and SCADAR observation versus the wind direction at the Mast location.

5.2.2. Gradient ratio by stability criteria

Fig 5.25 shows the wind speed ratio gradient averaged in each stability class. The WRF generally overestimate the ratio in the neutral cases. The standard deviation is largest for both WRF and SCADAR in the unstable condition, and relatively smaller in the stable condition and near-neutral condition. The stable set contains the largest number of samples as the stability indicator Ri_B is computed using variables at the Virtual Mast location. The WRF results generally show a higher average wind speed ratio but a smaller deviation compared with the SCADAR observations.

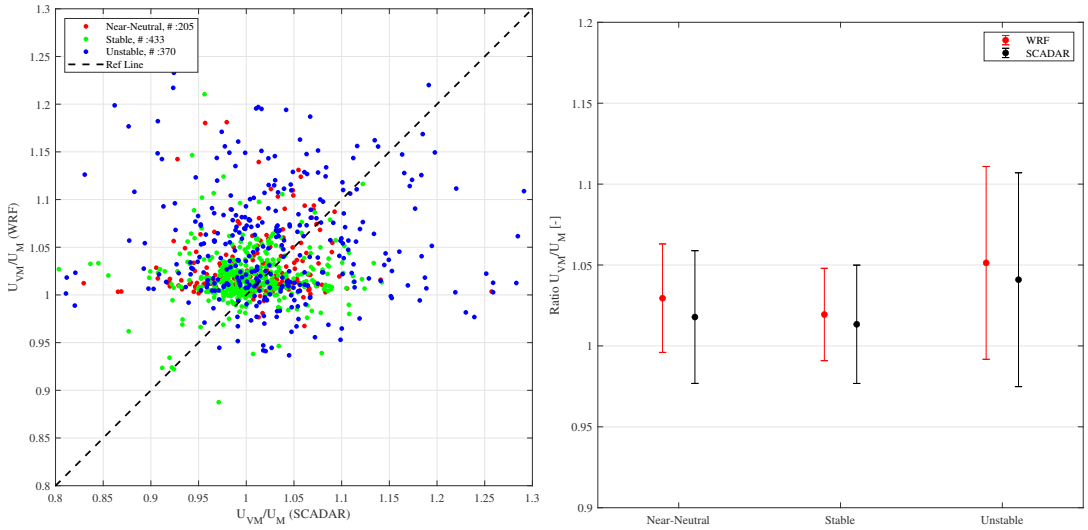

Figure 5.25: The wind speed gradient ratio grouped by atmospheric stability.

5.2.3. Wind speed vertical profile

Comparing the daily averaged profiles Fig 5.26, the first two flow cases are evaluated before the operation of the wind profiler 1 (ZP583), hence no observational data available for comparison, while the NEWA predicted profile seems corresponded well with the WRF prediction in these two cases. For the other cases, the daily averaged profile generally has a quite notable discrepancy between the observation and the mesoscale modelling. However, these differences are significantly reduced if the instantaneous profiles are investigated in the following section. For the wind speed gradient existing among four selected WRF grid points, as expected, all the flow cases are showing the profiles (Fig 5.26) shifting towards the higher wind speed when the grid points are furthering from the coastline. However, this gradient varies with height as well as different flow conditions. In general, the largest wind speed gradients are shown at the level close to the surface, which is the lowest level around 8m in the WRF vertical domain. These differences can be as significant as 2m/s since it is strongly affected by the surface roughness.

For the parallel flow cases, the most substantial wind speed difference over two nearest grid points around hub height can be as vast as 0.5m/s over a 1.4 km distance shown in flow case 2018-10-08. Since the figures are showing daily averaged wind speed profiles, the instantaneous wind speed gradients could be much more considerable. As discussed before, flow case 2018-08-18 and flow case 2018-10-08 has shown quite a similar pattern in both the wind trace and synoptic map. Similar wind speed profiles are also predicted by WRF for these two flow cases, except the flow case 2018-10-08 has a more significant wind speed gradient at the elevation where the low-level jet took place. For a distance of Mast location to extension grid points 2, the wind speed differences around the hub height for these two flow cases are about 1m/s versus 0.6m/s daily averaged.

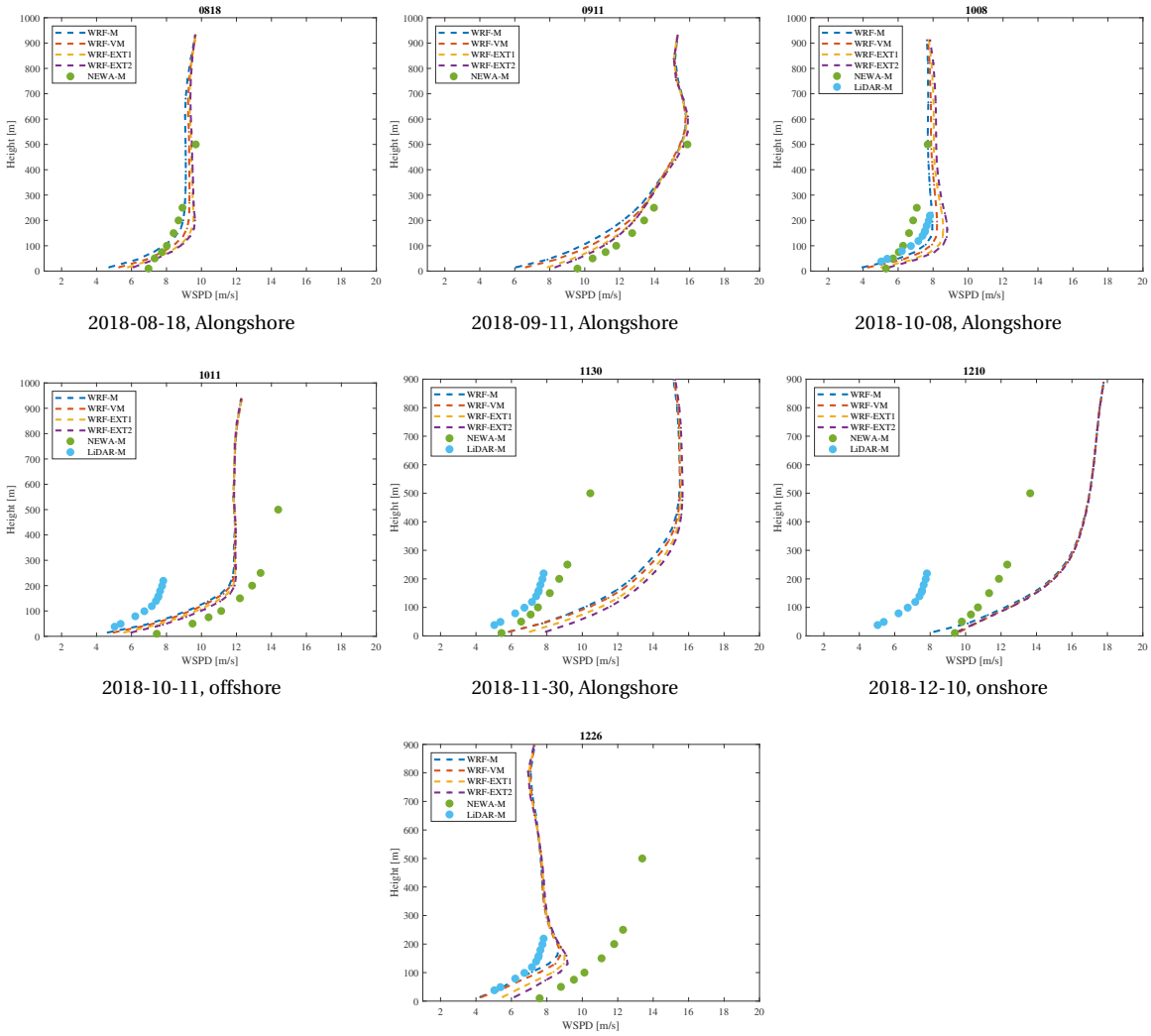

2018-08-18, Alongshore

2018-09-11, Alongshore

2018-10-08, Alongshore

2018-10-11, offshore

2018-11-30, Alongshore

2018-12-10, onshore

2018-12-26, Alongshore

Figure 5.26: Daily averaged wind speed profile for 4 locations.

The instantaneous wind profiles for selected four sites at 6:00, 12:00, 18:00, 24:00 UTC during the flow case 2018-11-30 are shown in the following Fig 5.27. It shows the WRF prediction at the four timesteps selected within these flow cases matches with the observation very well. The spatial gradient is not remarkable in the early morning at 6:00 UTC, while the inertial nighttime high wind speed remains. After sunrise, the boundary layer started growing and mixing. As a result, the vertical shear decreases, and it reaches the second-panel stage at noon. The profiles of 4 locations further segregated as they are experiencing different surface properties such as fluxes and roughness. In this flow case, the most substantial gradient shown at 18:00 UTC indicates a 3 m/s difference at the hub height between the Mast location and the extended grid point 2. Thus a $0.714 m/s$ per kilometre spatial gradient exists perpendicularly to the flow direction.

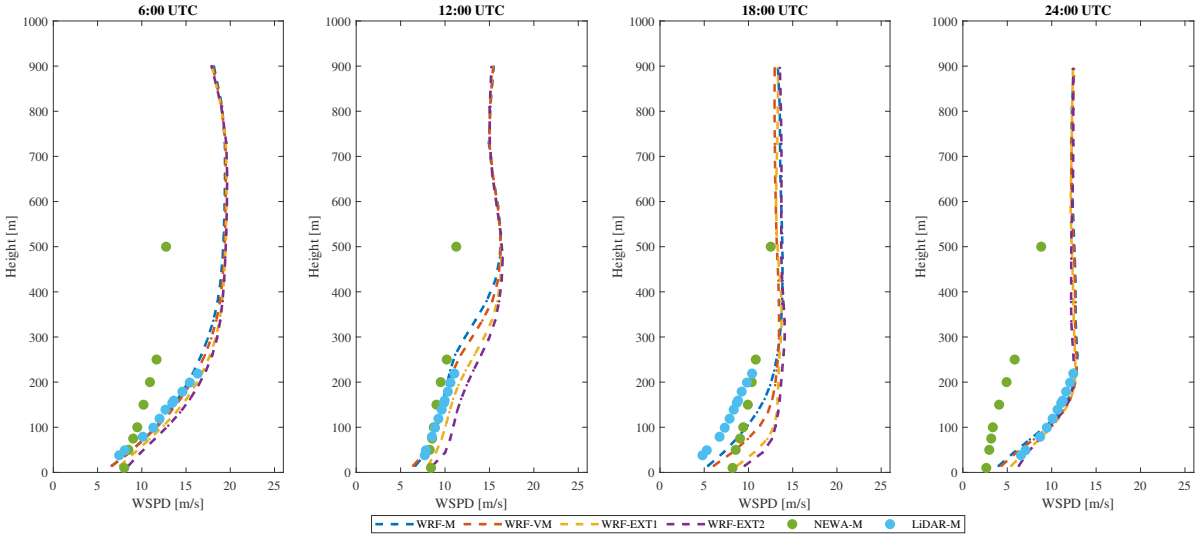

Figure 5.27: Instantaneous wind profile for 6:00, 12:00, 18:00, 24:00 UTC during the flow case 2018-11-30.

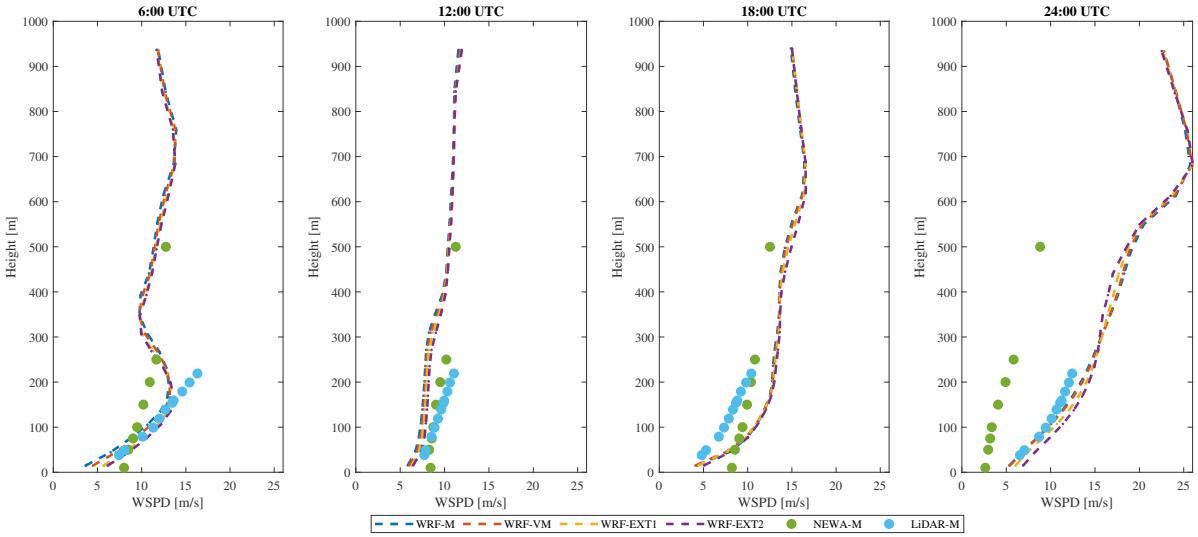

Figure 5.28: Instantaneous wind profile for 6:00, 12:00, 18:00, 24:00 UTC during the flow case 2018-10-11.

Alongside the flow direction, for the case 2018-10-11 (Fig 5.28), the spatial gradient is less evident than the previous parallel to the coast flow case. Given the view of the fact that the flow coming from the southwest direction (240 deg) has been forced under two different accelerations for a long fetch. As we are considering the spatial gradients from the nearest coast, it is conscious of seeing that the parallel to the coast flow cases will generally have more significant spatial gradients. If the real fetch along the downwind direction is restricted, the maximum wind speed gradient at the hub height is reduced to nearly half of the former status. Since the largest difference can be observed from the first panel for 6:00 UTC is only 1.5 m/s from the site mast to the extended site 2.

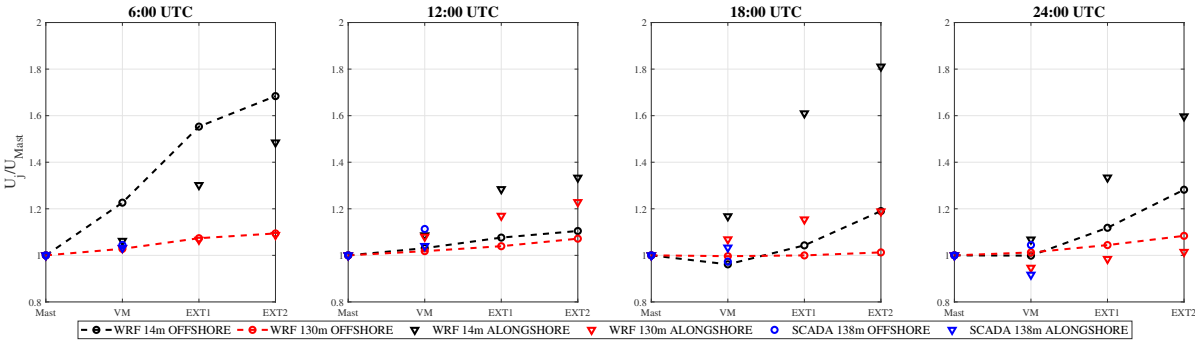

Figure 5.29: Wind speed of three extended sites normalized by the U_{Mast} at 6:00, 12:00, 18:00, and 24:00 UTC, for both the offshore and the alongshore flow.

See from Fig 5.29, a quantitive interpretation of wind speed gradient along the offshore direction is presented, while the flow is covering a surface discontinuity at the boundary of lake Ijsselmeer. The surface level 14m and the hub height 130m indicated by black and red color are selected to examine the ratio of U_j/U_{Mast}. The triangle and circle markers denote the alongshore flow case and the offshore flow case, respectively. Since the case study has covered 5 cases of alongshore flow cases, the ratio investigated here is calculated by averaging the ratio of all the alongshore flow cases. At the 14m height, the spatial gradient of the offshore flow case only surpasses the alongshore flow case at 6:00 UTC. For other timesteps, the alongshore cases generally have more considerable spatial gradients at the surface level 14m. As for the height of 130m, differences can barely be seen from two flow sectors at 6:00 UTC. At noon, the ratios at both two heights from alongshore cases exceed the ratio of offshore flow cases. The maximum ratio occurs at the evening transition time at 18:00 UTC. The predicted maximum ratio reaches 1.8 for the alongshore case, which is nearly doubled wind speed compared with it at mast location. At midnight, the offshore sector shows a higher gradient at the hub height as the gradient for alongshore cases somehow inversed during this period.

6

Discussion

In this study, the SCADAR observations are already processed data. Thus only the time-series at reconstruction points are provided, which means the comparison of the spatial image from WRF and SCADAR is not available. Meanwhile, due to the lack of observation on the water, there are no measured profiles that allow deriving the wind speed gradient directly from the observations. Hence, the observational data is mainly used as a validation of WRF simulation, rather than a direct data source of the learning object. The NEWA reanalysis data is also introduced to obtain the overview flow condition as its resolution is much coarser in temporal and spatial resolution, which significantly diminishes the quality of results for this study purpose. It seems the NEWA datasets are off compared to the observations in most of the flow cases, while the WRF simulation only fails in few timesteps of each flow case. Performing mesoscale modelling like WRF to compare with the SCADAR observation within such a small domain can be problematic. Firstly, the reconstruction point cannot precisely match the WRF grid points. Filtering must be applied to avoid considerable distances between them. Besides, the SCADAR is measuring inclined planes. Thus the observations are not at the same level depends on the distance from the anchor location. As a result, the time-series comparison at different sites is also at different elevations. Moreover, there are some gaps in the measurements as the data availability is decreasing along with the scanning distance. However, the performance of WRF simulation validated by SCADAR is valuable as it confirms the reliability of WRF to produce reasonable predictions for research purposes.

Glance through time-series for all the cases, the flow case 2018-10-08, with 240° alongshore direction, shows the most well-predicted wind speed from WRF. The performance of the model has quite an amount of uncertainty that originates from e.g. forcing data, PBL scheme, physical parameterization etc. As an instance, the atmospheric stability might contribute to the model performance to some extent. In this study, the atmospheric stability indicator is the Bulk Richardson number Ri_B formulated by

$$Ri_B = (g/T_0)(T_1 - T_0)Z_1/(U_1^2) \tag{6.1}$$

Where Z_1 is assumed to be $HH + D/2$ with HH is the hub-height and D is the rotor diameter. U_1 and T_1 are the wind speed and potential temperature at Z_1 respectively. T_0 is the skin temperature (TSK). For the neural condition, Ri_B will approach to 0, and Ri_b is larger than 0 for stable condition. See from fig 6.1, the stability for summer and autumn (early winter) generally has a clear diurnal cycle. For the winter cases, the dominant atmospheric stability is near-neutral condition. As for our best-predicted flow case 2018-10-08, it shows the largest possibility and magnitude of the stable condition. Moreover, the wind direction of the flow case also affects the accuracy of prediction significantly. From the right panel of 6.2, the WRF results lost its reliability within the sector $280 \pm 20°$, this might be due to the forming of IBL while the flow advecting across the coastline. The bin-averaged wind speed criteria by the stability show lesser differences between the model and the observation, WRF generally underestimate the wind speed for less than $0.5 m/s$ observed from the right panel of fig 6.2.

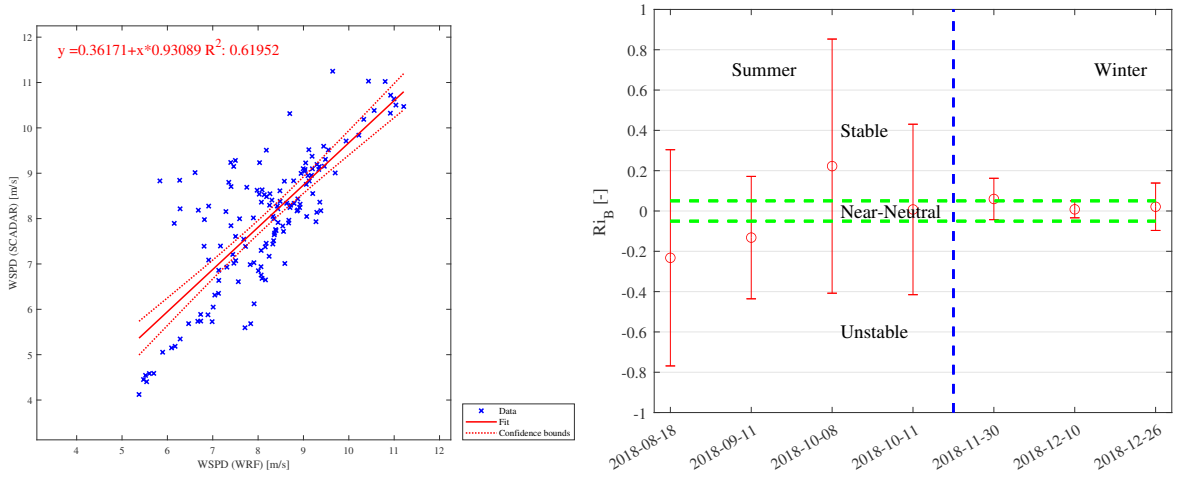

Figure 6.1: Right:The regression results for promoted flow case 2018-10-08. Left: Overall stability condition for all selected flow cases.

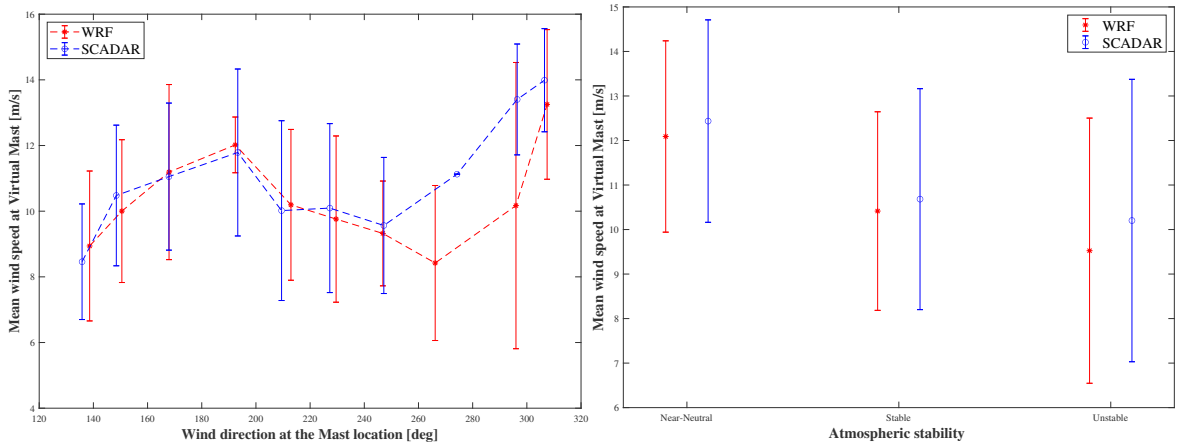

Figure 6.2: Right: Error analysis bin-averaged by wind direction sectors. Left: Error analysis bin-averaged by stability classes.

Regarding the wind speed gradient issues, WRF simulates the coastal wind gradients reasonably well at the hub height. It is a bit out of the expectation that the predicted wind speed gradients are more significant in those parallel to shoreline flow cases. The reason is considered to be that the fetches are not examined from its upstream direction. Looking at an example from Fig 6.3, both spatial images display notable spatial wind speed gradients. From the left panel, the upstream direction is the southwest direction, which is the bottom left corner of the lake IJsselmeer. Therefore, it indicates the flow has been accelerating differently along the shore for a long fetch. Thus, the spatial gradients are substantial when it reached our study domain. As for the offshore flow direction, the shear is still adjusting while it just passed surface discontinuity. The fetch from the Mast to Virtual mast is too short of producing a remarkable spatial gradient. Although the wind speed differences at the mast and virtual mast locations are less obvious, the distance between them is only approximately one-third of the range of wind plant Blauw if the onshore turbines that cannot be covered by SCADAR are also considered. Thus the gradient issue is still essential to be counted as the measurement at the mast cannot represent the overall energy production among the whole wind farm. Since the alongshore flow direction is the dominant cases according to the lake IJsselmeer climatology, the ratio of 1.2 reported in Fig 5.29 will account for insufficient monitoring if a single observation device is deployed to represent the flow condition of the whole wind farm at the mast location.

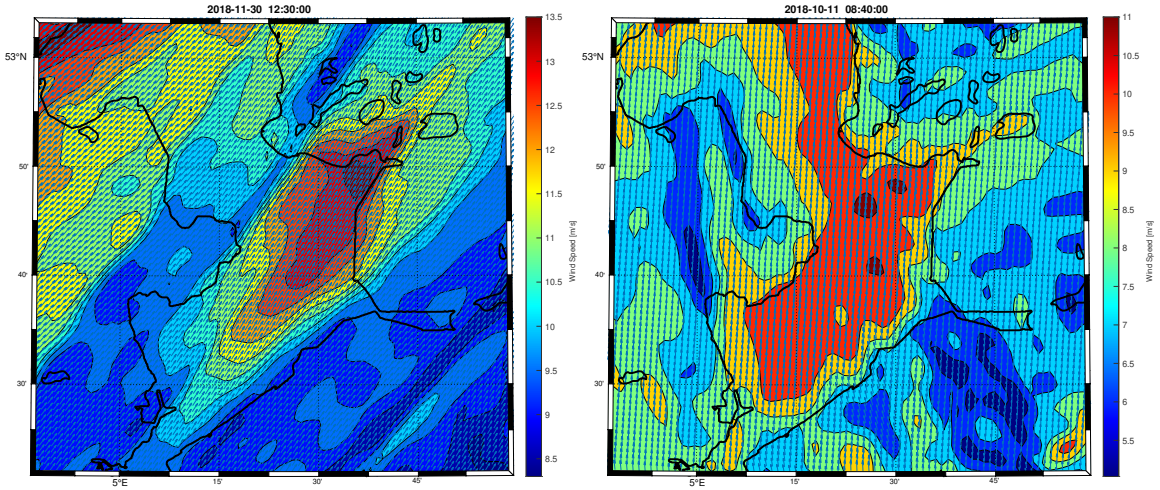

Figure 6.3: snapshots reflect the spatial gradients predicted by WRF for alongshore (2018-11-30) and offshore (2018-10-11) flow direction.

Further recommendation for a better understanding of the coastal wind speed gradient issues is to examine the topography effect within the study domain. Considering the lake IJsselmeer is an inland-lake located at the semi-closed region, and land-water interfaces surround it in many other sides, this makes it difficult to define its real flow direction as 'alongshore' or 'cross-shore'. Another possibility is to conduct similar research on domains outside the continent to reduce the possible topography effect. Moreover, it is also worth to performing WRF simulation with a longer time span to include all the wind direction sectors and seasonal effect while investigating the wind speed gradient issues, as the current experiment set-up only covered limited wind direction sector (from 120° to 320°) and the cases are not adequate to be representative of each season.

7

Conclusion

This research is focusing on flow cases in the coastal region. Cases with different flow directions, including perpendicular and parallel to the shoreline directions, are selected by analyzing the NEWA reanalysis data. After the cases are determined, high-resolution WRF simulations are performed under YSU PBL scheme with ERA5 forcing data. The simulation results are validated against the measurements from long-range wind scanner WindCube 400S. The validated data is analyzed for quantifying the horizontal wind speed gradient over the study domain. Some conclusions will be presented below.

Compared with SCADAR observations, WRF simulation is examined at a few selected grid points and vertical levels. Firstly, from the time-series and error statistic table 5.2, WRF simulation agrees better with the SCADAR observations than the NEWA did. WRF as a mesoscale modelling tool, it can capture the heterogeneity within the 6km range of SCADAR as higher resolutions are prescribed in the case set up. Secondly, WRF did a better prediction for those alongshore flow cases (1,2,3,5,7 Tab 3.3) with the wind direction around 240°. Most of the fluctuations in wind speed are precisely predicted both in time and magnitude in these cases. Some of the variations are correctly predicted in quantity but with shifting in time. More concretely, for the flow case 2018-09-11, a significant time lag between the model and observation exists, the predicted wind speed ramp down and the direction shifting took place three hours earlier in the WRF than the SCADAR observation. The error for the offshore (2018-10-11, 160°) and onshore flow case (2018-12-10, 340°) are more obvious than alongshore cases, directly seen from the time series, the peak wind speed in the morning of 2018-10-11 simulated by WRF is slightly lower in magnitude and earlier in time compared with the SCADAR observation. Moreover, the WRF with current setup cannot precisely predict the wind speed with small fluctuations throughout the whole flow case in 2018-12-10, the flow sector in which the wind is moving onshore and encounter the land boundaries leads to a very chaotic traces. In this case, the WRF almost lost all the correlation with the observational data despite that the $RMSE$ value was not that significant. In general, the statistic errors are acceptable compared with other lately published research [Ahsbahs et al., 2017].

For the wind speed gradient issues, the overall predicted wind speed differences around the typical hub height can reach 0.5 m/s daily averaged in absolute value over a 1.4 km distance. When the LLJs take place, it could be higher than 1m/s. This reflects a ratio of U_{loc2}/U_{loc1} (loc 1 and 2 represents the Mast location and the Virtual Mast location in this case) ranged between 1.05 to 1.2 commonly exists among most of the flow cases. Although the absolute value of wind speed for WRF model and SCADAR observation differs in many timesteps, the wind speed ratios of U_{VM}/U_M averaged among flow sectors is very close. WRF generally overestimates the wind speed ratios while bin-averaging the ratios by wind direction sectors or the atmospheric stabilities, but the standard deviations are smaller for WRF compared with the SCADAR

In summary, the long-range wind scanning LiDAR provides a great possibility for observing the flow condition over a wind farm sized domain. Especially for the nearshore wind farm, it compensates for lack of observations on the water. It is also a proper validation for the high-resolution mesoscale modelling study. The high-resolution WRF simulation carried in this study properly predicted the real flow condition compared to SCADAR observation. Thus the predicted wind speed gradient is considered to be reliable. It is also worth performing WRF simulation in longer period instead of selecting a few cases to obtain a more general horizontal wind speed gradient ratio. In principle, the WRF-only operation is not adequate to fully substitute the SCADAR as the errors remain significant in many specific cases according to the industry standard. Meanwhile, performing WRF with a temporal and spatial resolution comparable to the SCADAR observation

could be computationally expensive given current hardware support. Using WRF simulation as a supplement for the observation gaps due to the limited data availability or device maintenance would be the most proper option for supervising the wind farm operation.

Bibliography

[1] T. Ahsbahs, M. Badger, I. Karagali, and X. G. Larsén. Validation of sentinel-1a sar coastal wind speeds against scanning lidar. *Remote Sensing*, 9(6):552, 2017.

[2] M. L. Aitken and J. K. Lundquist. Utility-scale wind turbine wake characterization using nacelle-based long-range scanning lidar. *Journal of Atmospheric and Oceanic Technology*, 31(7):1529–1539, 2014.

[3] R. Barthelmie, J. Badger, S. Pryor, C. B. Hasager, M. B. Christiansen, and B. Jørgensen. Offshore coastal wind speed gradients: Issues for the design and development of large offshore windfarms. *Wind Engineering*, 31(6):369–382, 2007.

[4] M. Bilgili, A. Yasar, and E. Simsek. Offshore wind power development in europe and its comparison with onshore counterpart. *Renewable and Sustainable Energy Reviews*, 15(2):905–915, 2011.

[5] J. Blunden, D. S. Arndt, G. Hartfield, G. A. Weyhenmeyer, and M. G. Ziese. State of the climate in 2017. *Bulletin of The American Meteorological Society-(BAMS)*, 99(8):S1–S310, 2018.

[6] G. Brunet, S. Jones, P. M. Ruti, et al. *Seamless prediction of the Earth System: from minutes to months*. World Meteorological Organization, 2015.

[7] L. Cameron. Remote wind measurements offshore using scanning lidar systems offshore wind accelerator – wakes 2014. 2016.

[8] H. Charnock. Wind stress on a water surface. *Quarterly Journal of the Royal Meteorological Society*, 81 (350):639–640, 1955.

[9] A. E. Cohen, S. M. Cavallo, M. C. Coniglio, and H. E. Brooks. A review of planetary boundary layer parameterization schemes and their sensitivity in simulating southeastern us cold season severe weather environments. *Weather and forecasting*, 30(3):591–612, 2015.

[10] P. Enevoldsen and G. Xydis. Examining the trends of 35 years growth of key wind turbine components. *Energy for sustainable development*, 50:18–26, 2019.

[11] R. Floors, C. L. Vincent, S.-E. Gryning, A. Peña, and E. Batchvarova. The wind profile in the coastal boundary layer: Wind lidar measurements and numerical modelling. *Boundary-layer meteorology*, 147 (3):469–491, 2013.

[12] R. Floors, A. Peña, G. Lea, N. Vasiljević, E. Simon, and M. Courtney. The rune experiment—a database of remote-sensing observations of near-shore winds. *Remote Sensing*, 8(11):884, 2016.

[13] N. N. C. for Environmental Information. Global climate report for annual 2019, 2019. URL https://www.ncdc.noaa.gov/sotc/global/201913.

[14] S. Gallagher, R. Tiron, E. Whelan, E. Gleeson, F. Dias, and R. McGrath. The nearshore wind and wave energy potential of ireland: a high resolution assessment of availability and accessibility. *Renewable Energy*, 88:494–516, 2016.

[15] J. Garratt. The internal boundary layer—a review. *Boundary-Layer Meteorology*, 50(1-4):171–203, 1990.

[16] T. Glickman. *Glossary of meteorology*. American Meteorological Society, 2000. ISBN 9781878220349.

[17] J. P. Goit, A. Yamaguchi, and T. Ishihara. Measurement and prediction of wind fields at an offshore site by scanning doppler lidar and wrf. *Atmosphere*, 11(5):442, 2020.

[18] J. Gottschall, B. Gribben, D. Stein, and I. Würth. Floating lidar as an advanced offshore wind speed measurement technique: Current technology status and gap analysis in regard to full maturity. *Wiley Interdisciplinary Reviews: Energy and Environment*, 6(5):e250, 2017.

[19] T. Holt and S. Raman. A review and comparative evaluation of multilevel boundary layer parameterizations for first-order and turbulent kinetic energy closure schemes. *Reviews of geophysics*, 26(4):761–780, 1988.

[20] J. Holton. An introduction to dynamic meteorology, int. *Geophys. Ser*, 88:313–369, 2004.

[21] S.-Y. Hong, Y. Noh, and J. Dudhia. A new vertical diffusion package with an explicit treatment of entrainment processes. *Monthly weather review*, 134(9):2318–2341, 2006.

[22] H. K. Jacobsen, P. Hevia-Koch, and C. Wolter. Nearshore and offshore wind development: Costs and competitive advantage exemplified by nearshore wind in denmark. *Energy for Sustainable Development*, 50:91–100, 2019.

[23] M. Junginger, A. Louwen, N. G. Tuya, D. de Jager, E. van Zuijlen, and M. Taylor. Offshore wind energy. In *Technological Learning in the Transition to a Low-Carbon Energy System*, pages 103–117. Elsevier, 2020.

[24] J. K. Kaldellis and D. Zafirakis. The wind energy (r) evolution: A short review of a long history. *Renewable energy*, 36(7):1887–1901, 2011.

[25] D. Kim, T. Kim, G. Oh, J. Huh, and K. Ko. A comparison of ground-based lidar and met mast wind measurements for wind resource assessment over various terrain conditions. *Journal of Wind Engineering and Industrial Aerodynamics*, 158:109–121, 2016.

[26] B. Lange, H. Johnson, S. E. Larsen, and J. Højstrup. The dependence of sea surface roughness on windwaves. *EAEJA*, page 8639, 2003.

[27] B. Lange, S. E. Larsen, J. Hojstrup, and R. Barthelmie. The wind speed profile at offshore wind farm sites. In *Proc. of the OWEMES 2003 Conference, Naples (Italy)*, 2003.

[28] A. Lee. Offshore wind power price plunges by a third in a year: Bnef, 2019. URL https://www.rechargenews.com/transition/offshore-wind-power-price-plunges-by-a-third-in-a-year-bnef/2-1-692944.

[29] J. Li and X. B. Yu. Lidar technology for wind energy potential assessment: Demonstration and validation at a site around lake erie. *Energy Conversion and Management*, 144:252–261, 2017.

[30] R. Lindsey and L. Dahlman, 2020.

[31] J. Mann, N. Angelou, J. Arnqvist, D. Callies, E. Cantero, R. C. Arroyo, M. Courtney, J. Cuxart, E. Dellwik, J. Gottschall, et al. Complex terrain experiments in the new european wind atlas. *Philosophical Transactions of the Royal Society A: Mathematical, Physical and Engineering Sciences*, 375(2091):20160101, 2017.

[32] G. L. Mellor and T. Yamada. Development of a turbulence closure model for geophysical fluid problems. *Reviews of Geophysics*, 20(4):851–875, 1982.

[33] R. Menke, N. Vasiljević, K. S. Hansen, A. N. Hahmann, and J. Mann. Does the wind turbine wake follow the topography? a multi-lidar study in complex terrain. *Wind Energy Science*, 3(2):681–691, 2018.

[34] T. Mikkelsen, M. Sjöholm, N. Angelou, and J. Mann. 3d windscanner lidar measurements of wind and turbulence around wind turbines, buildings and bridges. In *First Conference of Computational Methods in Offshore Technology*, volume 276, 2017.

[35] T. Misaki, T. Ohsawa, M. Konagaya, H. Kato, T. Mito, and S. Eguchi. Investigation of wrf simulated horizontal wind speed gradient using scanning lidar measurement. In *Grand Renewable Energy proceedings Japan council for Renewable Energy (2018)*, page 184. Japan Council for Renewable Energy, 2018.

[36] M. Nakanishi and H. Niino. An improved mellor–yamada level-3 model with condensation physics: Its design and verification. *Boundary-layer meteorology*, 112(1):1–31, 2004.

[37] E. J. Plate. Aerodynamic characteristics of atmospheric boundary layers. Technical report, Argonne National Lab., Ill. Karlsruhe Univ.(West Germany), 1971.

[38] S. Pryor and R. Barthelmie. Analysis of the effect of the coastal discontinuity on near-surface flow. In *Annales Geophysicae*, volume 16, pages 882–888. Springer, 1998.

[39] Z. Pu and E. Kalnay. Numerical weather prediction basics: Models, numerical methods, and data assimilation. 2018.

[40] O. Reitebuch. Wind lidar for atmospheric research. In *Atmospheric Physics*, pages 487–507. Springer, 2012.

[41] J. S. Ryan Wiser, Maureen Hand and B. Paulos. The future of wind energy, part 3: Reducing wind energy costs through increased turbine size: Is the sky the limit?, 2016. URL https://emp.lbl.gov/news/future-wind-energy-part-3-reducing-wind.

[42] S. A. Savelyev and P. A. Taylor. Internal boundary layers: I. height formulae for neutral and diabatic flows. *Boundary-Layer Meteorology*, 115(1):1–25, 2005.

[43] D. A. Smith, M. Harris, A. S. Coffey, T. Mikkelsen, H. E. Jørgensen, J. Mann, and R. Danielian. Wind lidar evaluation at the danish wind test site in høvsøre. *Wind Energy: An International Journal for Progress and Applications in Wind Power Conversion Technology*, 9(1-2):87–93, 2006.

[44] D. A. Spera. Wind turbine technology. 1994.

[45] D. J. Stensrud. *Parameterization schemes: keys to understanding numerical weather prediction models*. Cambridge University Press, 2009.

[46] D. Sun, Z. Zhong, J. Zhou, H. Hu, and T. Kobayashi. Accuracy analysis of the fabry–perot etalon based doppler wind lidar. *Optical review*, 12(5):409–414, 2005.

[47] N. Svensson, H. Bergström, A. Rutgersson, and E. Sahlée. Modification of the baltic sea wind field by land-sea interaction. *Wind Energy*, 22(6):764–779, 2019.

[48] P. K. Taylor and M. J. Yelland. The dependence of sea surface roughness on the height and steepness of the waves. *Journal of physical oceanography*, 31(2):572–590, 2001.

[49] A. Van Wijk, A. Beljaars, A. Holtslag, and W. Turkenburg. Evaluation of stability corrections in wind speed profiles over the north sea. *Journal of Wind Engineering and Industrial Aerodynamics*, 33(3):551–566, 1990.

[50] J. M. Wallace and P. V. Hobbs. *Atmospheric science: an introductory survey*, volume 92. Elsevier, 2006.

[51] WindEurope. Wind energy in europe in 2018—trends and statistics. *Wind Europe: Brussels, Belgium*, 2019.

[52] M. Wolsink. Near-shore wind power—protected seascapes, environmentalists' attitudes, and the technocratic planning perspective. *Land use policy*, 27(2):195–203, 2010.

[53] Y. Zuo and H. Liu. Evaluation on comprehensive benefit of wind power generation and utilization of wind energy. In *2012 IEEE International Conference on Computer Science and Automation Engineering*, pages 635–638. IEEE, 2012.

A

Appendix

A.1. PDF of NEWA & DOWA

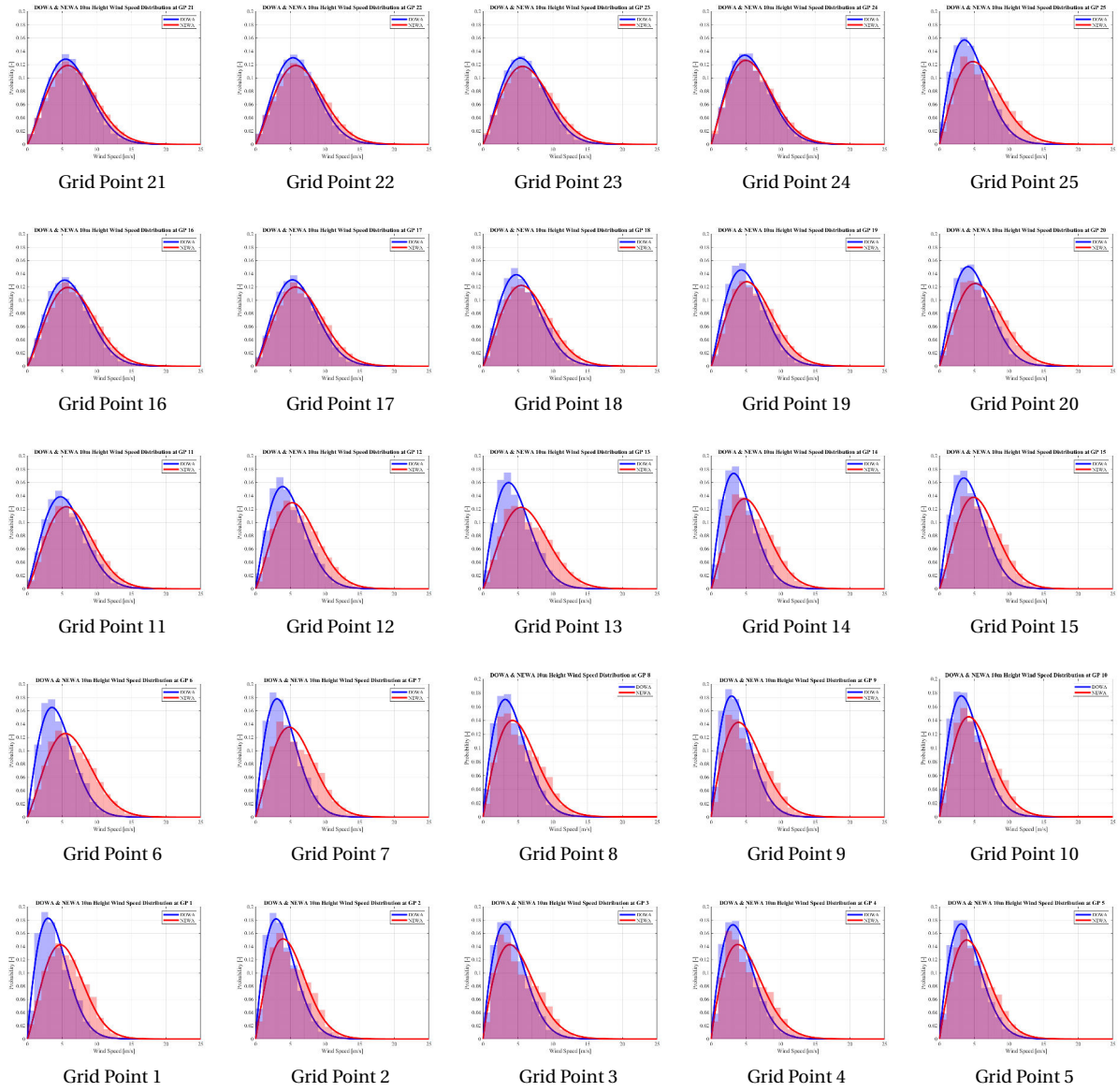

Figure A.1: PDF plots of DOWA & NEWA data for 25 grid points at 10m height.

PDF at 100m.

Figure A.2: PDF plots of DOWA & NEWA data for 25 grid points at 100m height.

Figure A.3: PDF plots of DOWA & NEWA data for 25 grid points at 150m height.

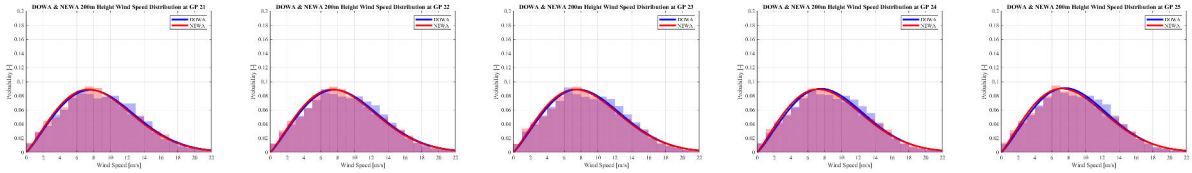

Grid Point 21 Grid Point 22 Grid Point 23 Grid Point 24 Grid Point 25

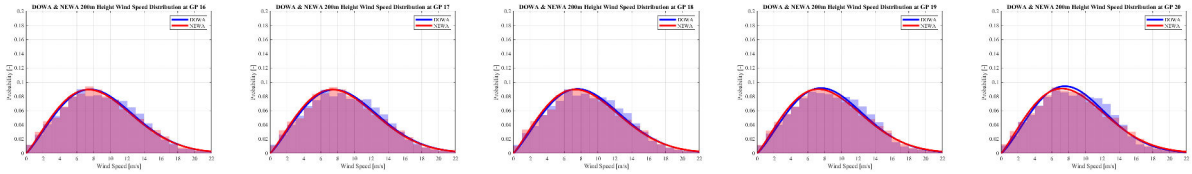

Grid Point 16 Grid Point 17 Grid Point 18 Grid Point 19 Grid Point 20

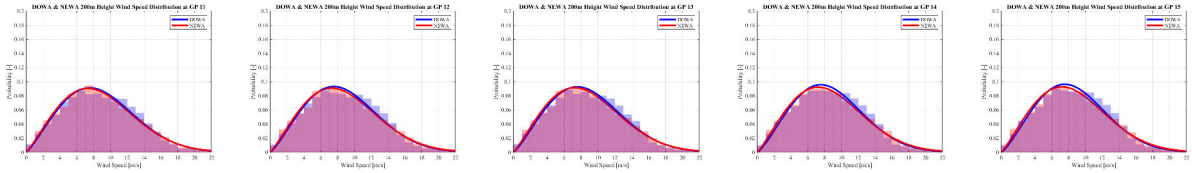

Grid Point 11 Grid Point 12 Grid Point 13 Grid Point 14 Grid Point 15

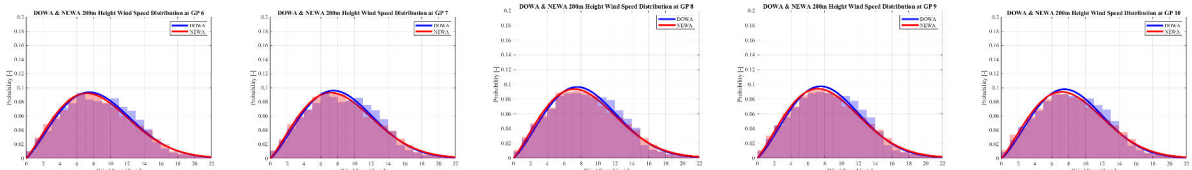

Grid Point 6 Grid Point 7 Grid Point 8 Grid Point 9 Grid Point 10

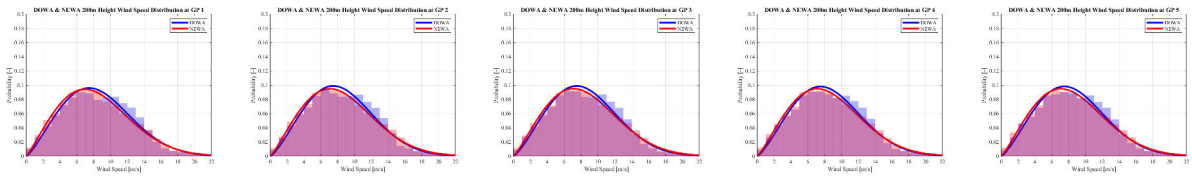

Grid Point 1 Grid Point 2 Grid Point 3 Grid Point 4 Grid Point 5

Figure A.4: PDF plots of DOWA & NEWA data for 25 grid points at 200m height.

Grid Point 21 Grid Point 22 Grid Point 23 Grid Point 24 Grid Point 25

Grid Point 16 Grid Point 17 Grid Point 18 Grid Point 19 Grid Point 20

Grid Point 11 Grid Point 12 Grid Point 13 Grid Point 14 Grid Point 15

Grid Point 6 Grid Point 7 Grid Point 8 Grid Point 9 Grid Point 10

Grid Point 1 Grid Point 2 Grid Point 3 Grid Point 4 Grid Point 5

Figure A.5: PDF plots of DOWA & NEWA data for 25 grid points at 500m height.

A.2. Vertical Profiles at 0Z, 6Z, 12Z, 18Z

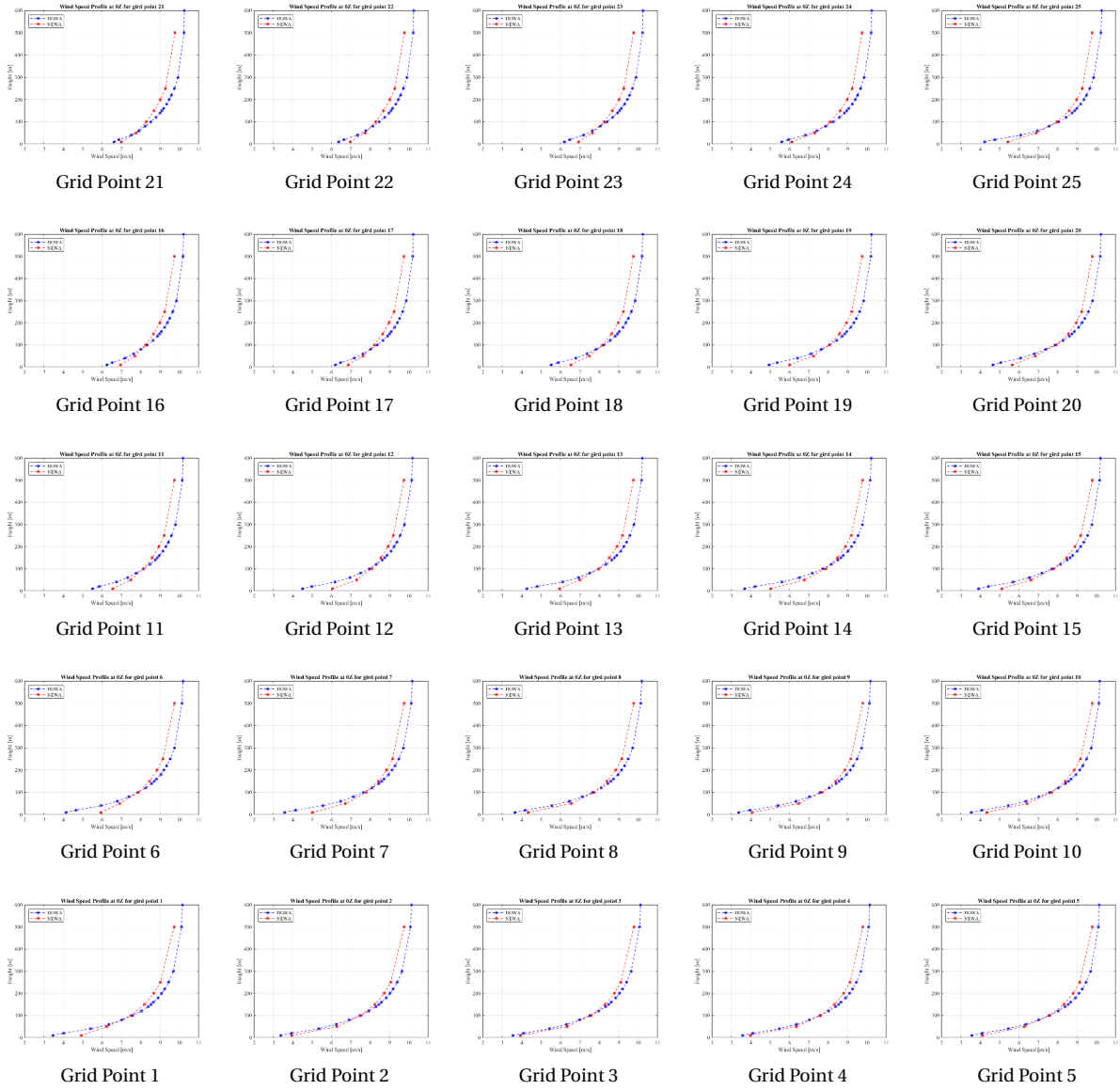

Grid Point 21 Grid Point 22 Grid Point 23 Grid Point 24 Grid Point 25

Grid Point 16 Grid Point 17 Grid Point 18 Grid Point 19 Grid Point 20

Grid Point 11 Grid Point 12 Grid Point 13 Grid Point 14 Grid Point 15

Grid Point 6 Grid Point 7 Grid Point 8 Grid Point 9 Grid Point 10

Grid Point 1 Grid Point 2 Grid Point 3 Grid Point 4 Grid Point 5

Figure A.6: Vertical profiles of NEWA & DOWA dataset at 0Z time.

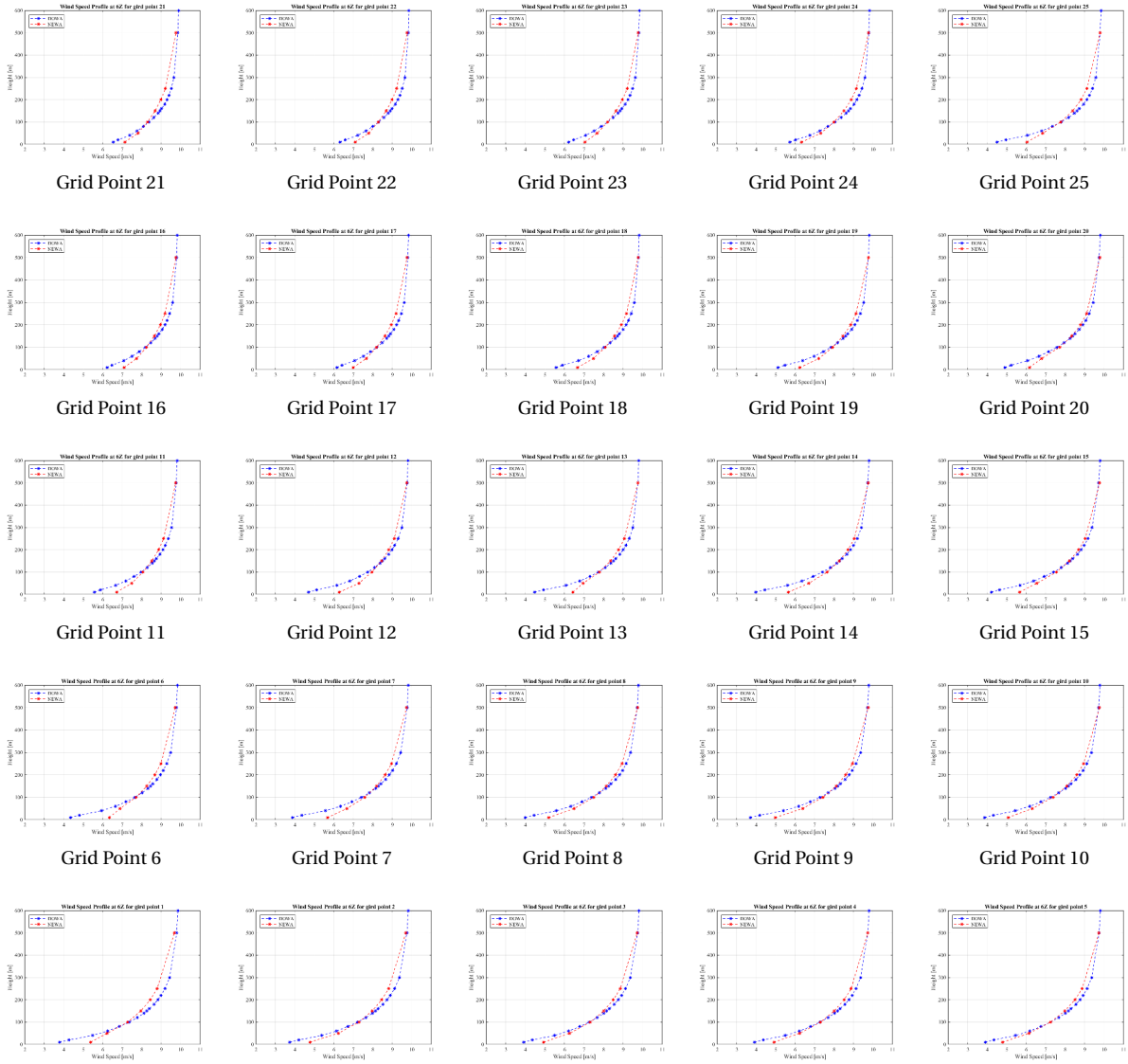

Grid Point 21 Grid Point 22 Grid Point 23 Grid Point 24 Grid Point 25

Grid Point 16 Grid Point 17 Grid Point 18 Grid Point 19 Grid Point 20

Grid Point 11 Grid Point 12 Grid Point 13 Grid Point 14 Grid Point 15

Grid Point 6 Grid Point 7 Grid Point 8 Grid Point 9 Grid Point 10

Grid Point 1 Grid Point 2 Grid Point 3 Grid Point 4 Grid Point 5

Figure A.7: Vertical profiles of NEWA & DOWA dataset at 6Z time.

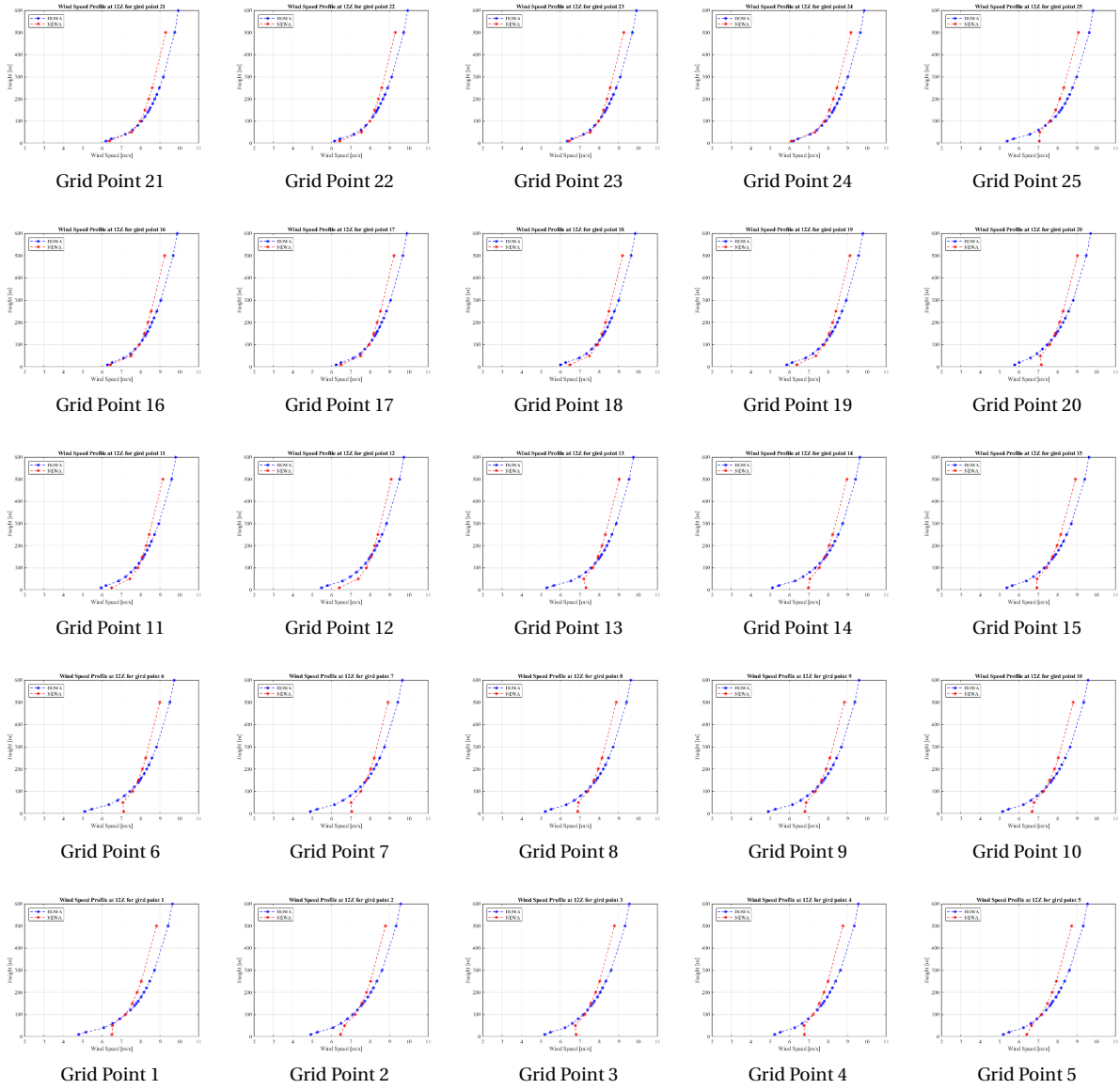

Grid Point 21 Grid Point 22 Grid Point 23 Grid Point 24 Grid Point 25

Grid Point 16 Grid Point 17 Grid Point 18 Grid Point 19 Grid Point 20

Grid Point 11 Grid Point 12 Grid Point 13 Grid Point 14 Grid Point 15

Grid Point 6 Grid Point 7 Grid Point 8 Grid Point 9 Grid Point 10

Grid Point 1 Grid Point 2 Grid Point 3 Grid Point 4 Grid Point 5

Figure A.8: Vertical profiles of NEWA & DOWA dataset at 12Z time.

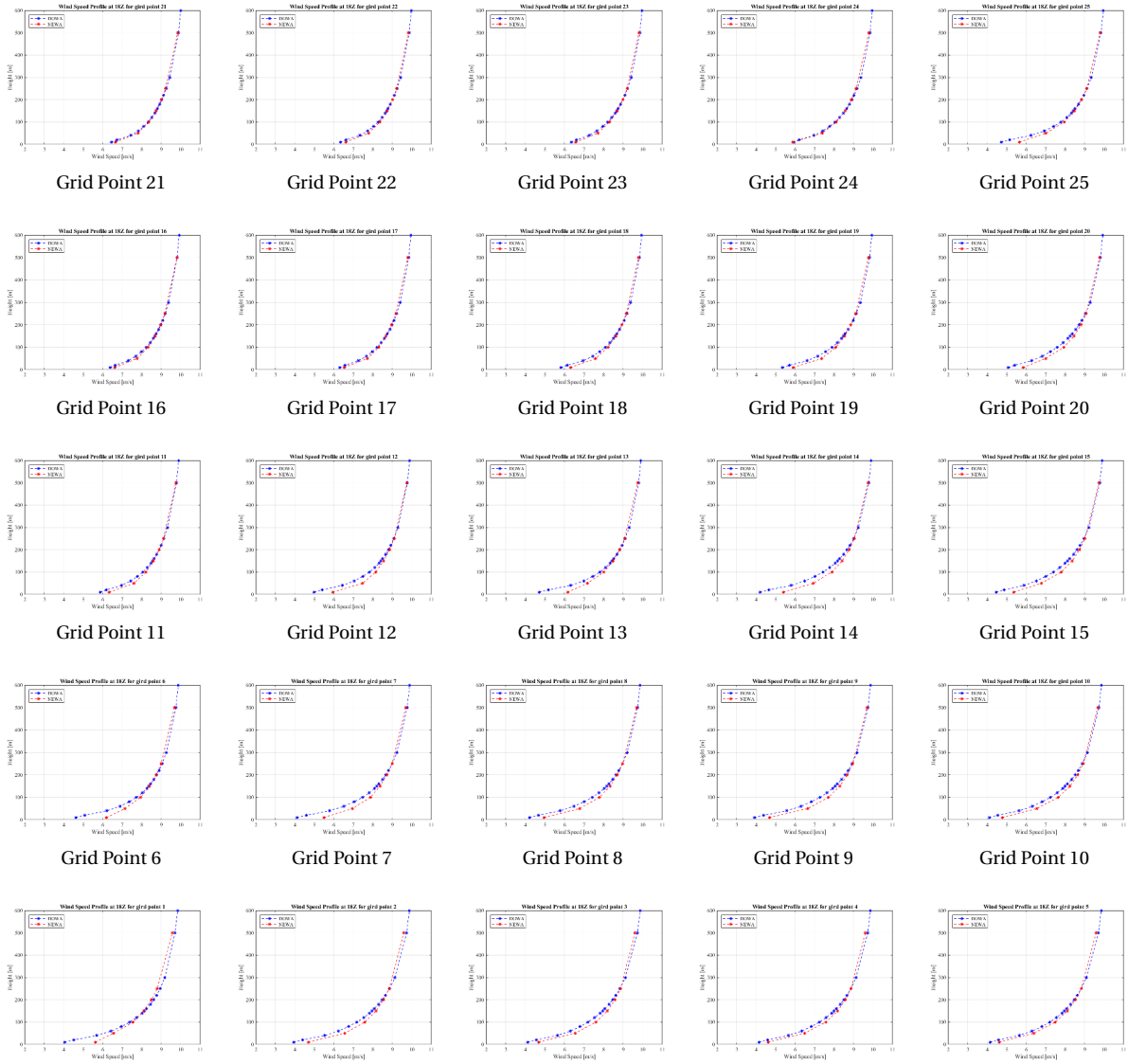

Grid Point 21 Grid Point 22 Grid Point 23 Grid Point 24 Grid Point 25

Grid Point 16 Grid Point 17 Grid Point 18 Grid Point 19 Grid Point 20

Grid Point 11 Grid Point 12 Grid Point 13 Grid Point 14 Grid Point 15

Grid Point 6 Grid Point 7 Grid Point 8 Grid Point 9 Grid Point 10

Grid Point 1 Grid Point 2 Grid Point 3 Grid Point 4 Grid Point 5

Figure A.9: Vertical profiles of NEWA & DOWA dataset at 18Z time.

A.3. NEWA Wind Frequency Rose for 10m and 100m at 0Z,6Z,12Z,18Z

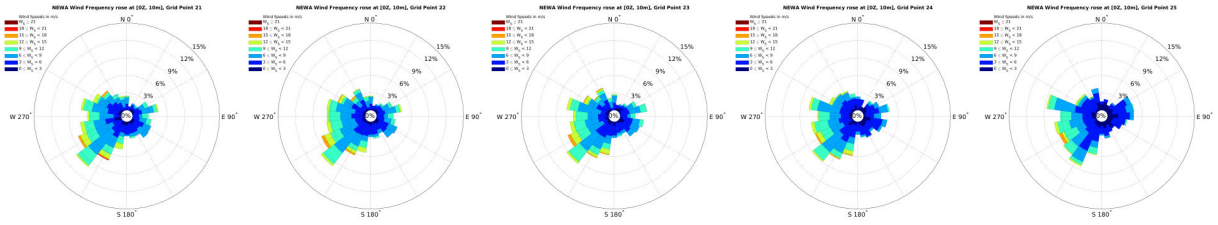

Grid Point 21 Grid Point 22 Grid Point 23 Grid Point 24 Grid Point 25

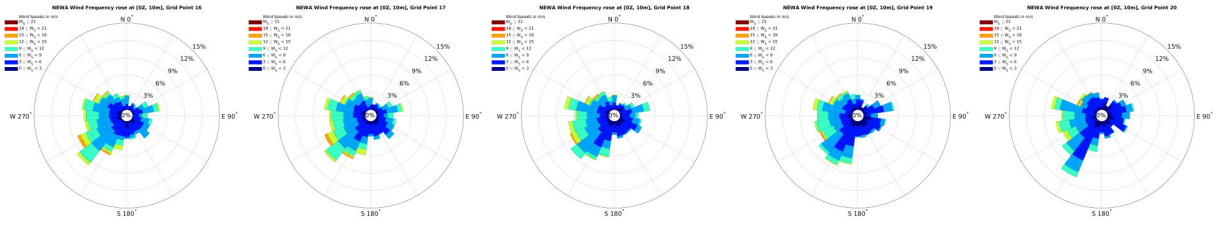

Grid Point 16 Grid Point 17 Grid Point 18 Grid Point 19 Grid Point 20

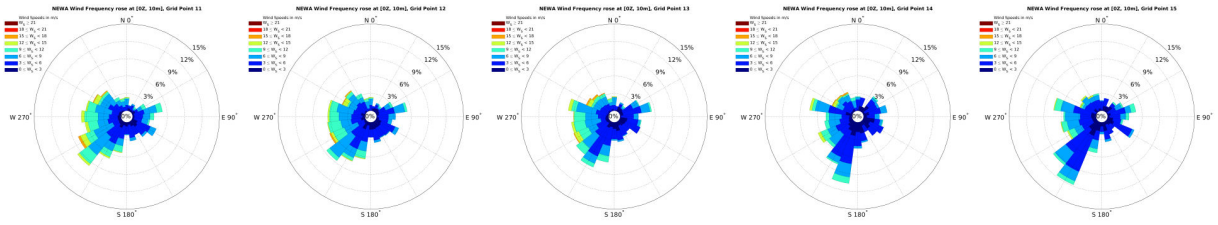

Grid Point 11 Grid Point 12 Grid Point 13 Grid Point 14 Grid Point 15

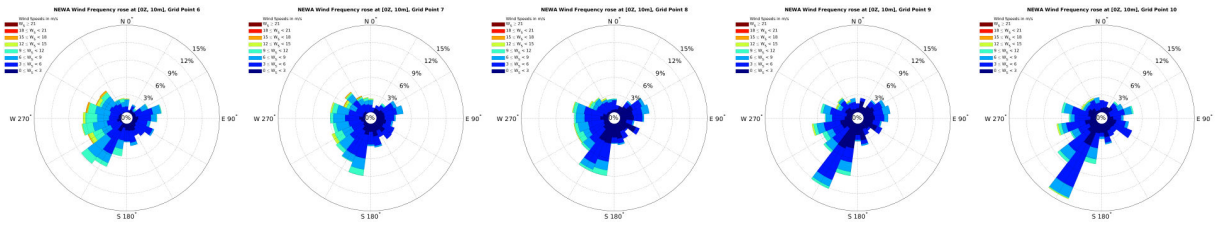

Grid Point 6 Grid Point 7 Grid Point 8 Grid Point 9 Grid Point 10

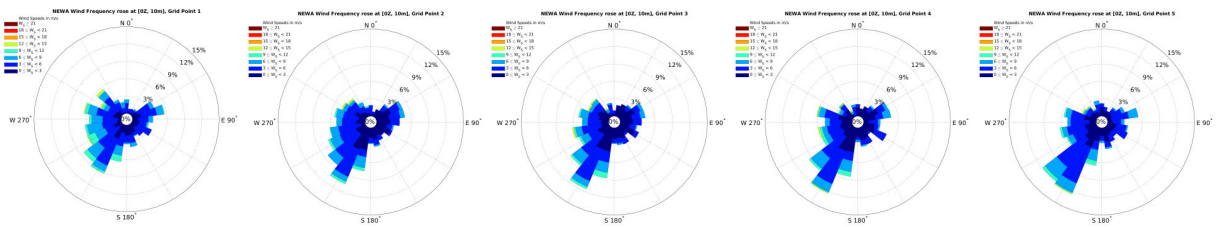

Grid Point 1 Grid Point 2 Grid Point 3 Grid Point 4 Grid Point 5

Figure A.10: NEWA wind frequency rose for 0Z time, 10m height.

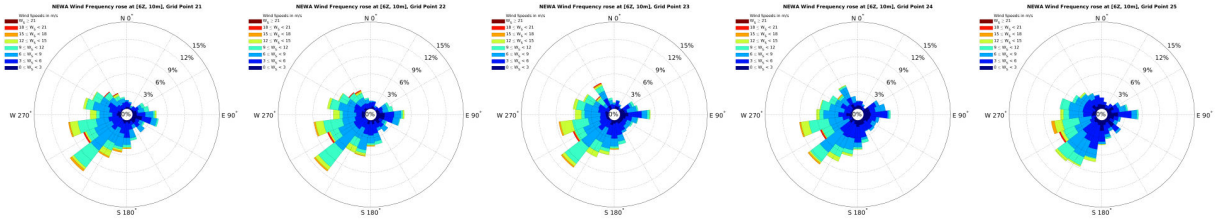

Grid Point 21 Grid Point 22 Grid Point 23 Grid Point 24 Grid Point 25

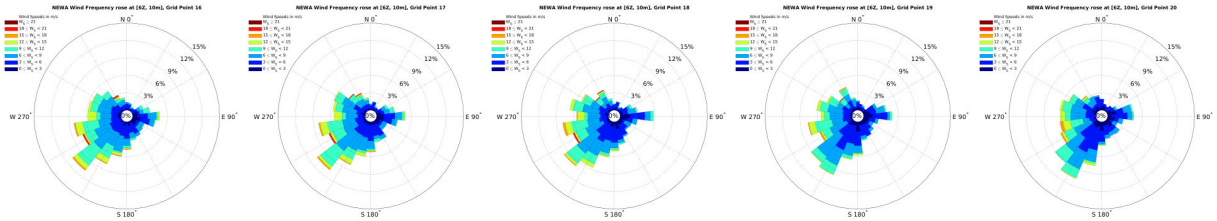

Grid Point 16 Grid Point 17 Grid Point 18 Grid Point 19 Grid Point 20

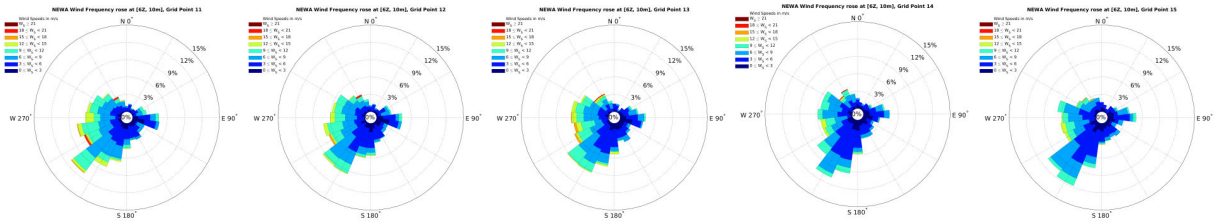

Grid Point 11 Grid Point 12 Grid Point 13 Grid Point 14 Grid Point 15

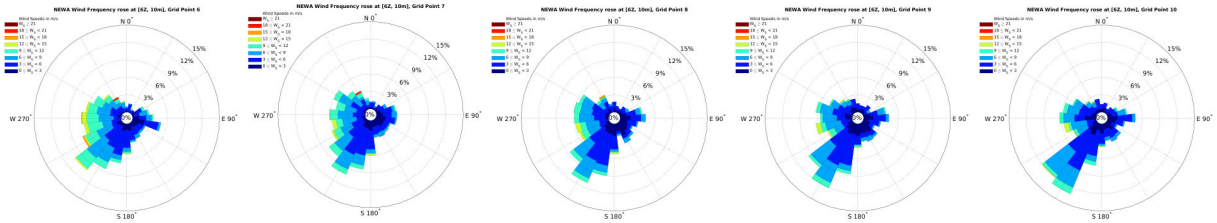

Grid Point 6 Grid Point 7 Grid Point 8 Grid Point 9 Grid Point 10

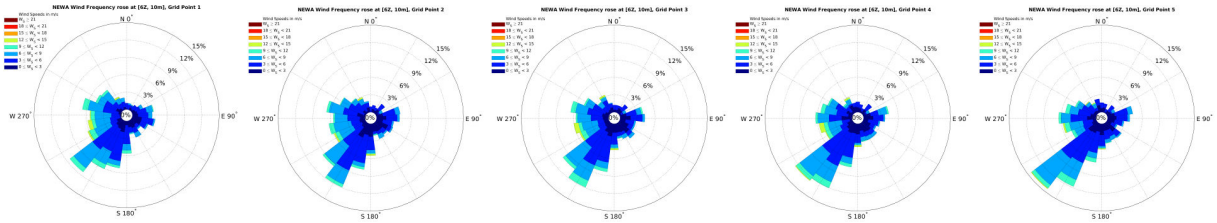

Grid Point 1 Grid Point 2 Grid Point 3 Grid Point 4 Grid Point 5

Figure A.11: NEWA wind frequency rose for 6Z time, 10m height.

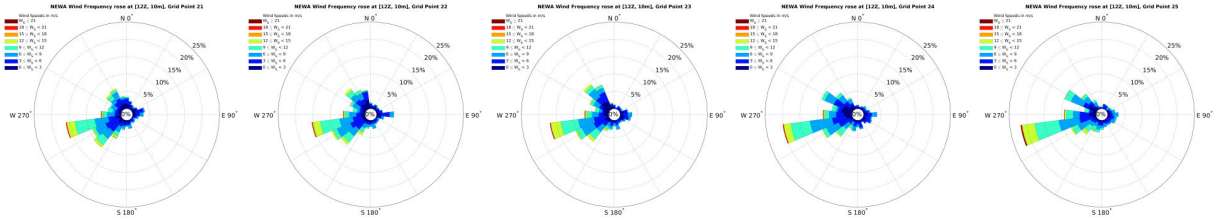

Grid Point 21 Grid Point 22 Grid Point 23 Grid Point 24 Grid Point 25

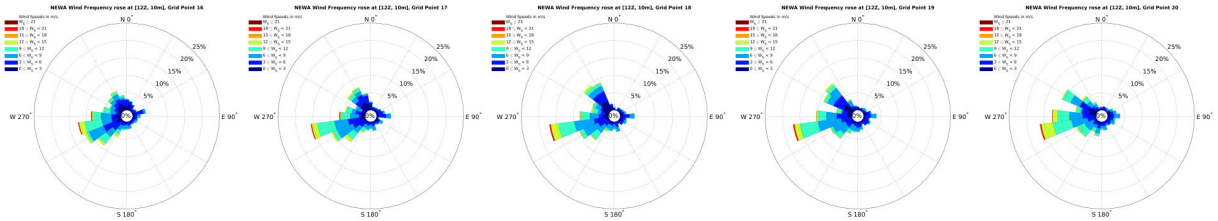

Grid Point 16 Grid Point 17 Grid Point 18 Grid Point 19 Grid Point 20

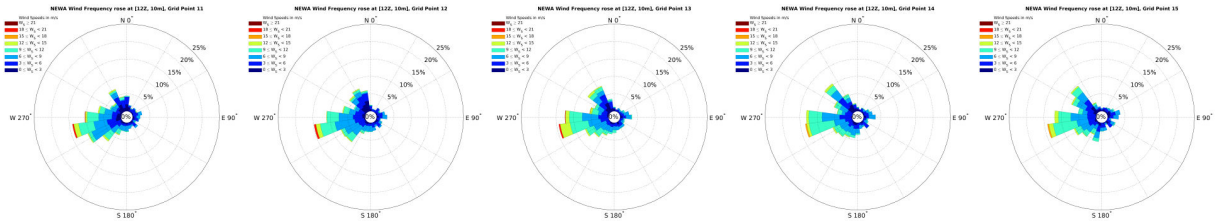

Grid Point 11 Grid Point 12 Grid Point 13 Grid Point 14 Grid Point 15

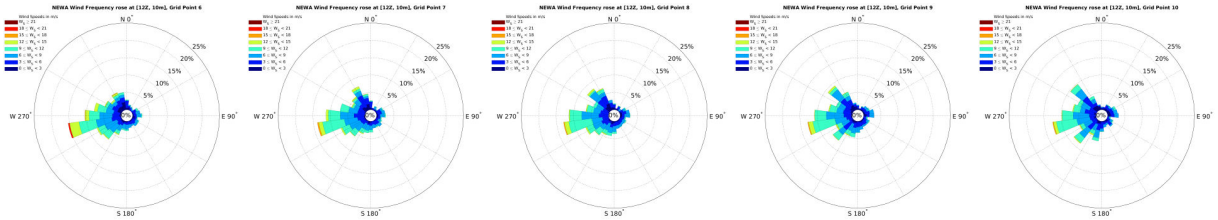

Grid Point 6 Grid Point 7 Grid Point 8 Grid Point 9 Grid Point 10

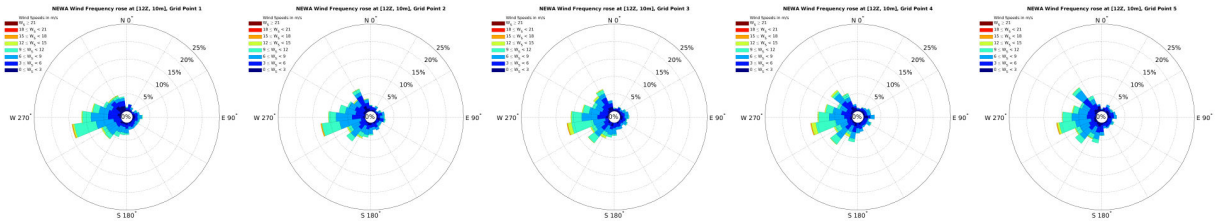

Grid Point 1 Grid Point 2 Grid Point 3 Grid Point 4 Grid Point 5

Figure A.12: NEWA wind frequency rose for 12Z time, 10m height.

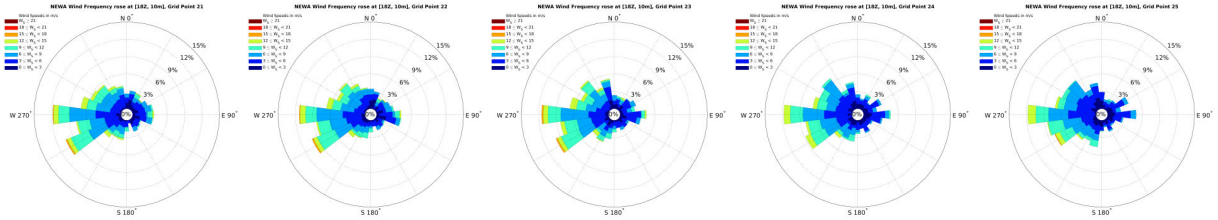

Grid Point 21 Grid Point 22 Grid Point 23 Grid Point 24 Grid Point 25

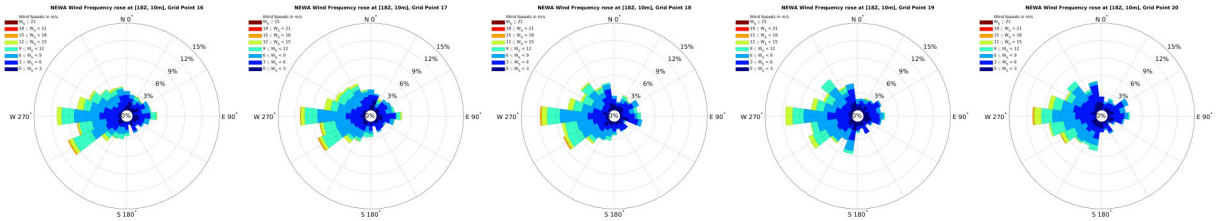

Grid Point 16 Grid Point 17 Grid Point 18 Grid Point 19 Grid Point 20

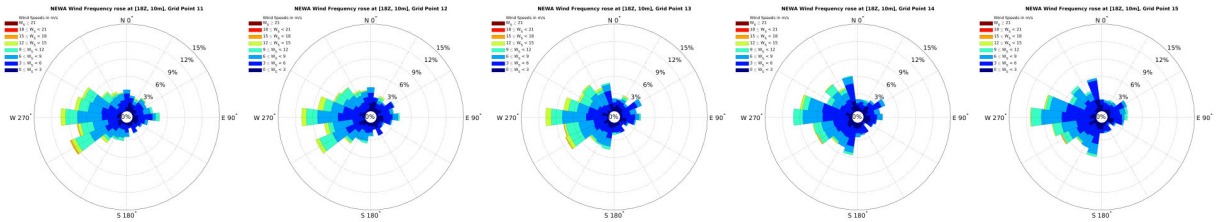

Grid Point 11 Grid Point 12 Grid Point 13 Grid Point 14 Grid Point 15

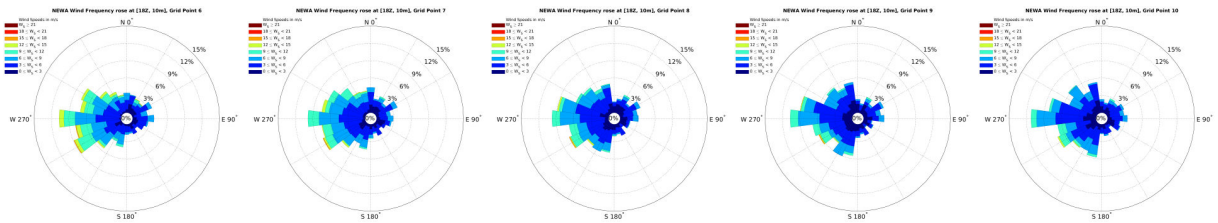

Grid Point 6 Grid Point 7 Grid Point 8 Grid Point 9 Grid Point 10

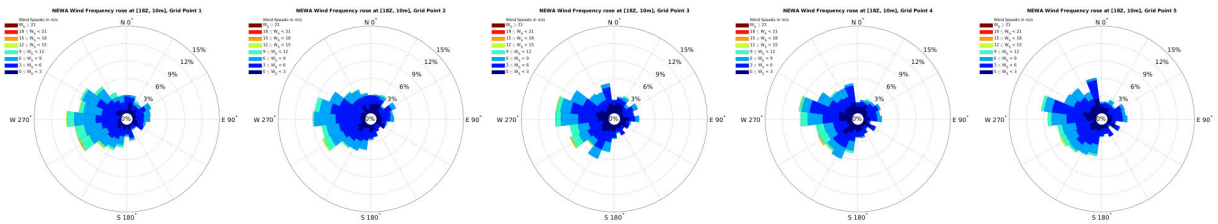

Grid Point 1 Grid Point 2 Grid Point 3 Grid Point 4 Grid Point 5

Figure A.13: NEWA wind frequency rose for 18Z time, 10m height.

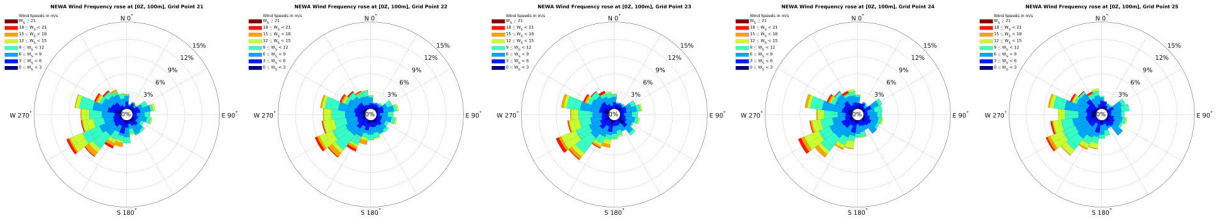

Grid Point 21 Grid Point 22 Grid Point 23 Grid Point 24 Grid Point 25

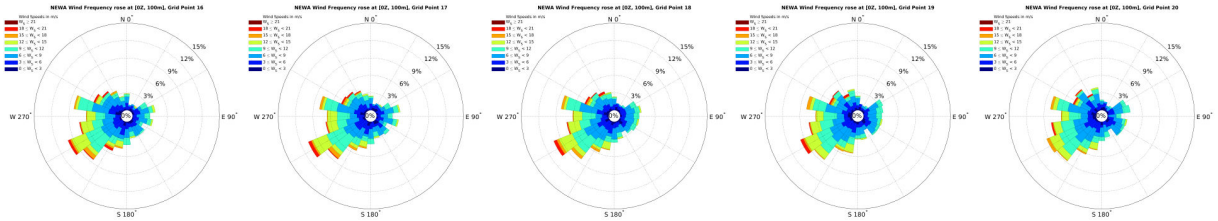

Grid Point 16 Grid Point 17 Grid Point 18 Grid Point 19 Grid Point 20

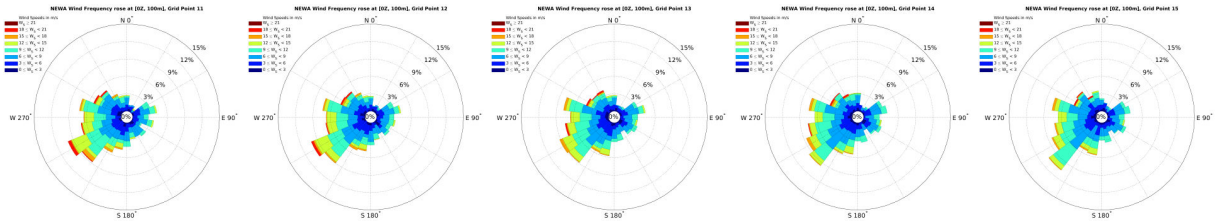

Grid Point 11 Grid Point 12 Grid Point 13 Grid Point 14 Grid Point 15

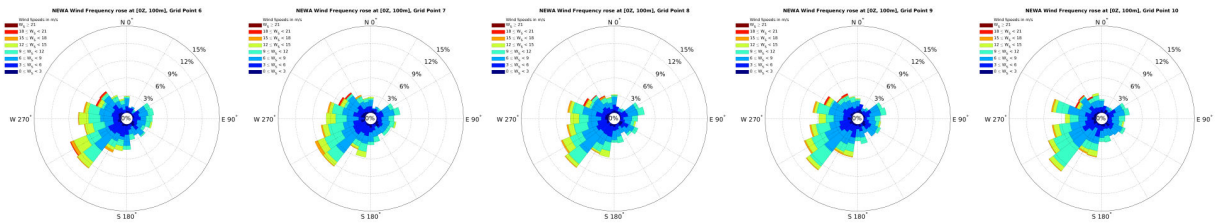

Grid Point 6 Grid Point 7 Grid Point 8 Grid Point 9 Grid Point 10

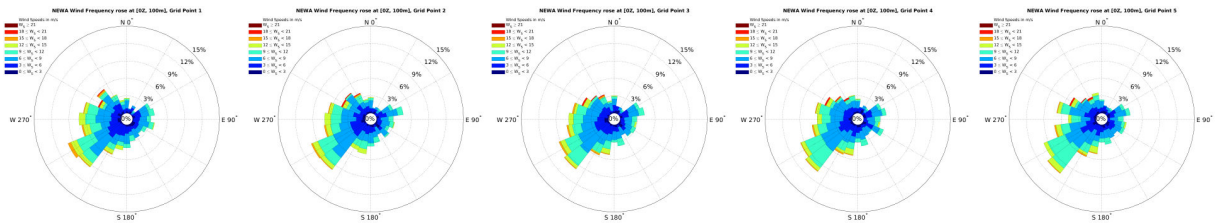

Grid Point 1 Grid Point 2 Grid Point 3 Grid Point 4 Grid Point 5

Figure A.14: NEWA wind frequency rose for 0Z time, 100m height.

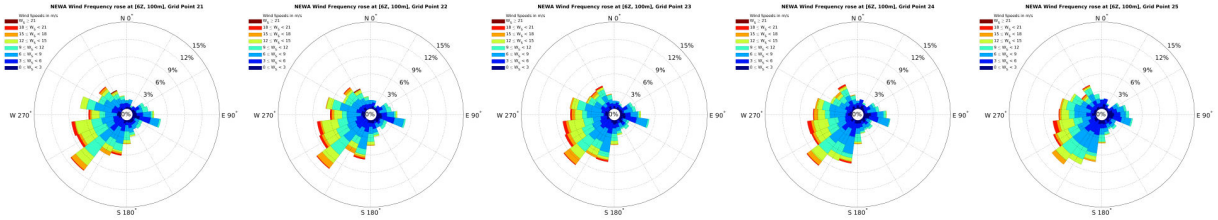

Grid Point 21 Grid Point 22 Grid Point 23 Grid Point 24 Grid Point 25

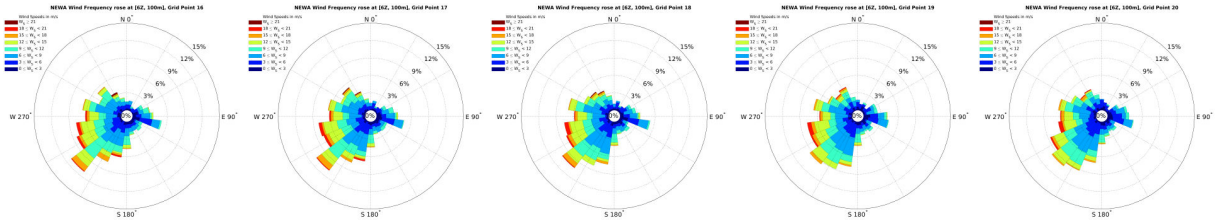

Grid Point 16 Grid Point 17 Grid Point 18 Grid Point 19 Grid Point 20

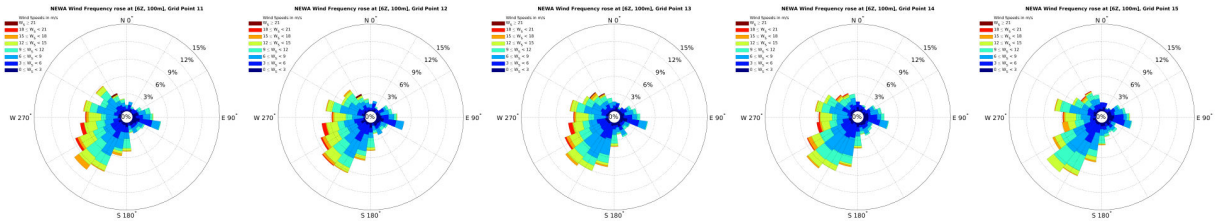

Grid Point 11 Grid Point 12 Grid Point 13 Grid Point 14 Grid Point 15

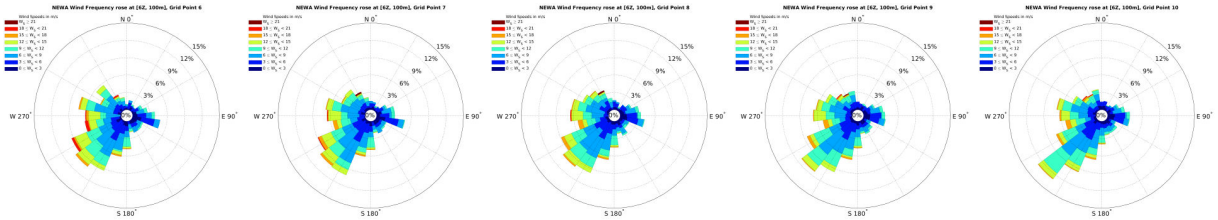

Grid Point 6 Grid Point 7 Grid Point 8 Grid Point 9 Grid Point 10

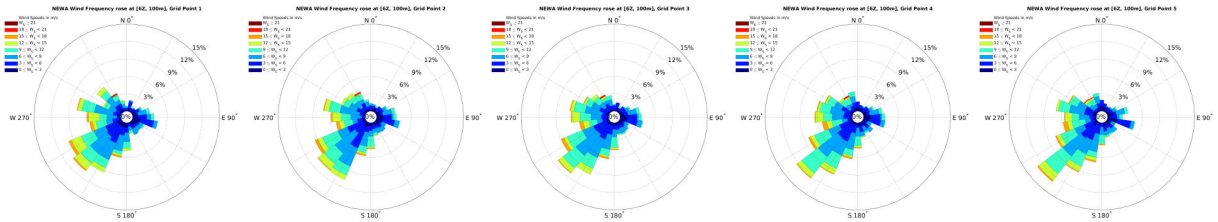

Grid Point 1 Grid Point 2 Grid Point 3 Grid Point 4 Grid Point 5

Figure A.15: NEWA wind frequency rose for 6Z time, 100m height.

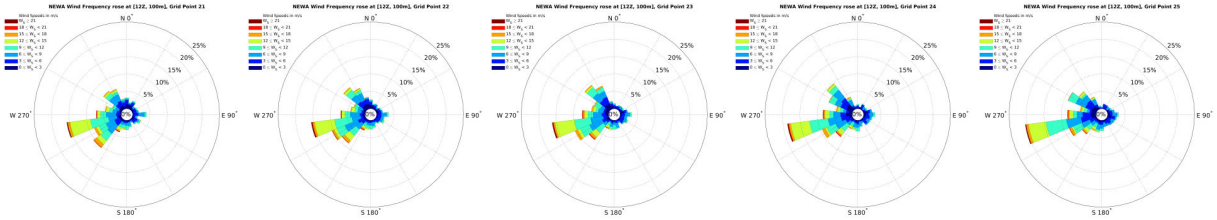

Grid Point 21 Grid Point 22 Grid Point 23 Grid Point 24 Grid Point 25

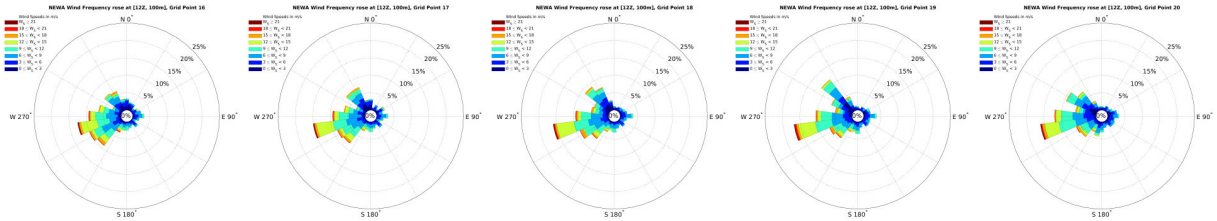

Grid Point 16 Grid Point 17 Grid Point 18 Grid Point 19 Grid Point 20

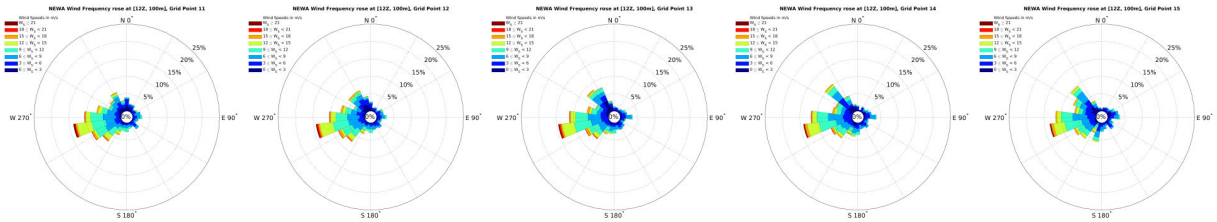

Grid Point 11 Grid Point 12 Grid Point 13 Grid Point 14 Grid Point 15

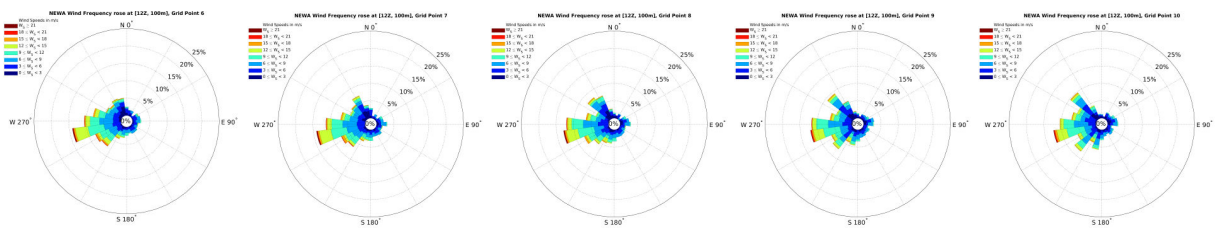

Grid Point 6 Grid Point 7 Grid Point 8 Grid Point 9 Grid Point 10

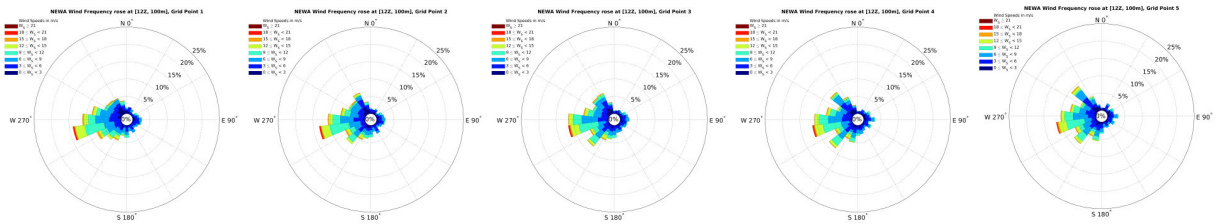

Grid Point 1 Grid Point 2 Grid Point 3 Grid Point 4 Grid Point 5

Figure A.16: NEWA wind frequency rose for 12Z time, 100m height.

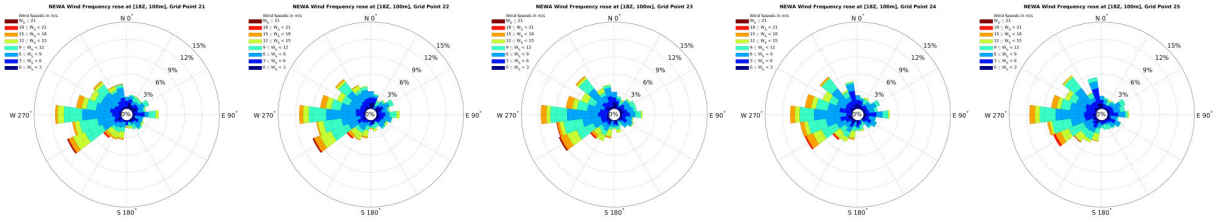

Grid Point 21 Grid Point 22 Grid Point 23 Grid Point 24 Grid Point 25

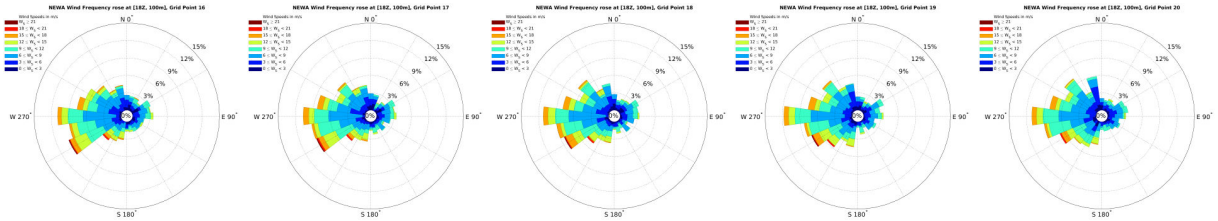

Grid Point 16 Grid Point 17 Grid Point 18 Grid Point 19 Grid Point 20

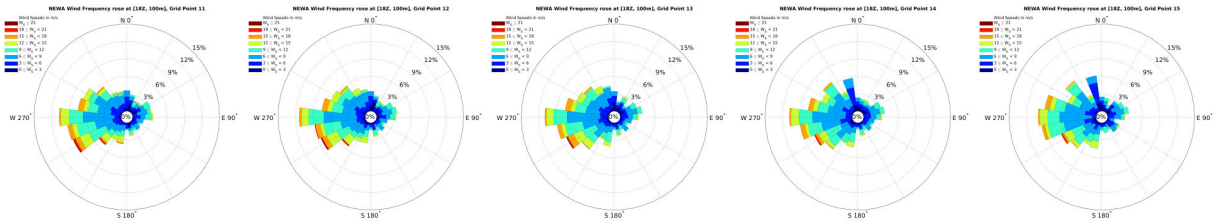

Grid Point 11 Grid Point 12 Grid Point 13 Grid Point 14 Grid Point 15

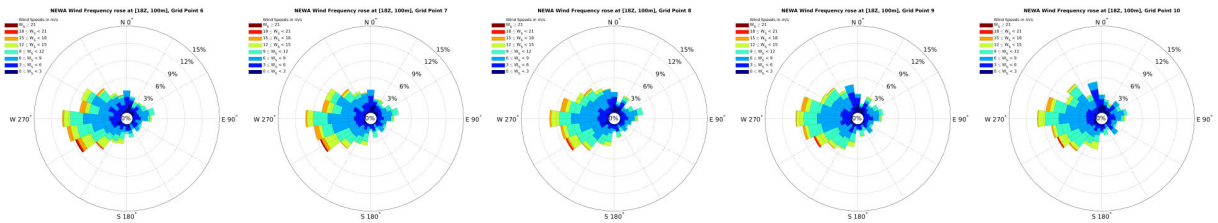

Grid Point 6 Grid Point 7 Grid Point 8 Grid Point 9 Grid Point 10

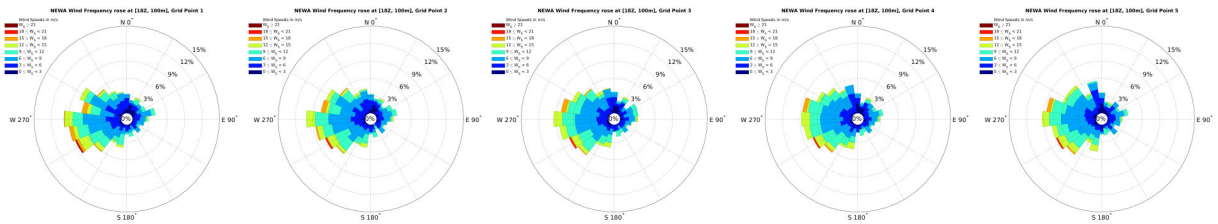

Grid Point 1 Grid Point 2 Grid Point 3 Grid Point 4 Grid Point 5

Figure A.17: NEWA wind frequency rose for 18Z time, 100m height.

A.4. Wind speed at around hub height

A.4.1. Flow case 2018-08-18

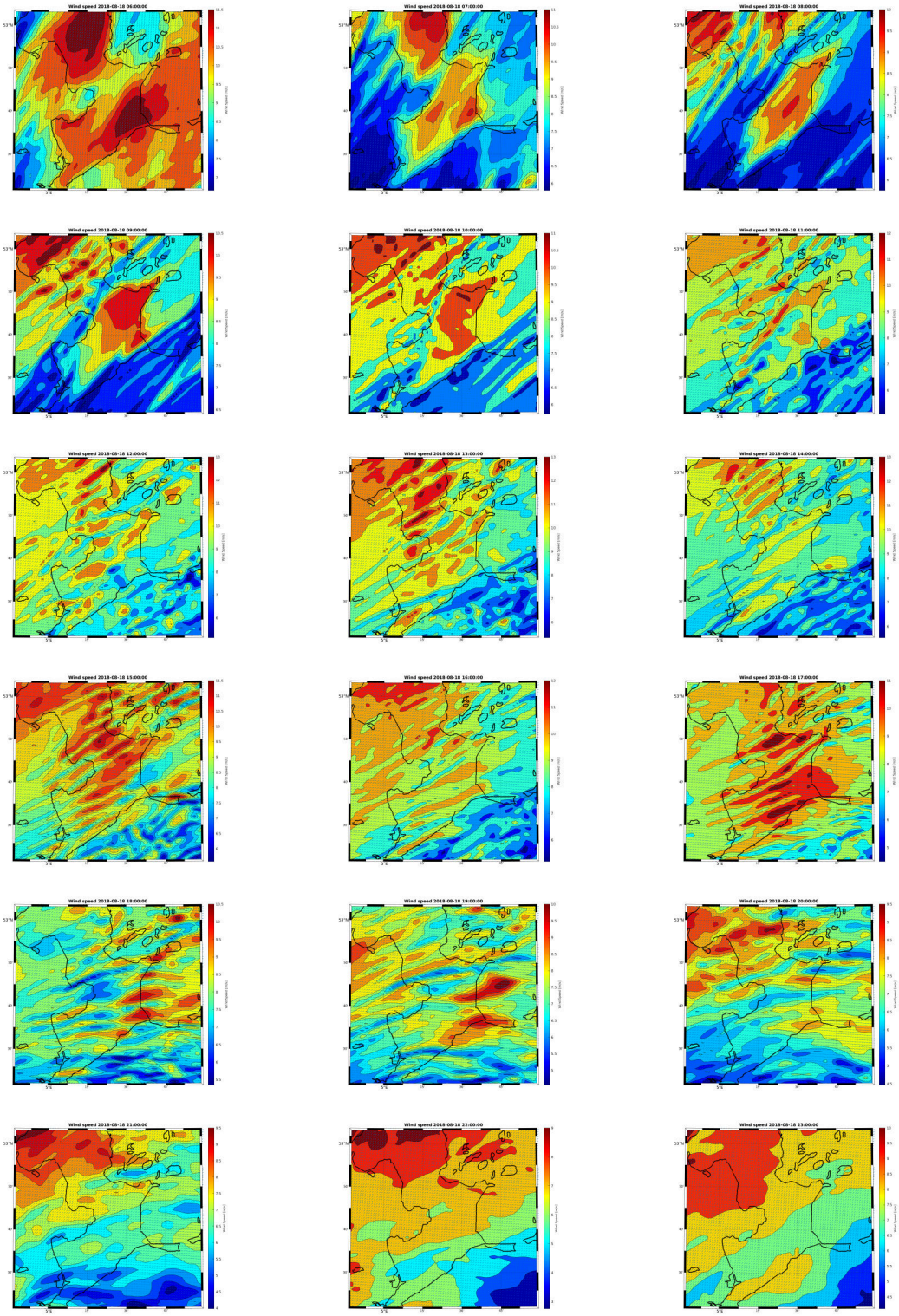

Figure A.18: WRF simulated wind speed around the hub height for flow case 2018-08-18 from 6:00 UTC to 23:00 UTC

A.4.2. Flow case 2018-09-11

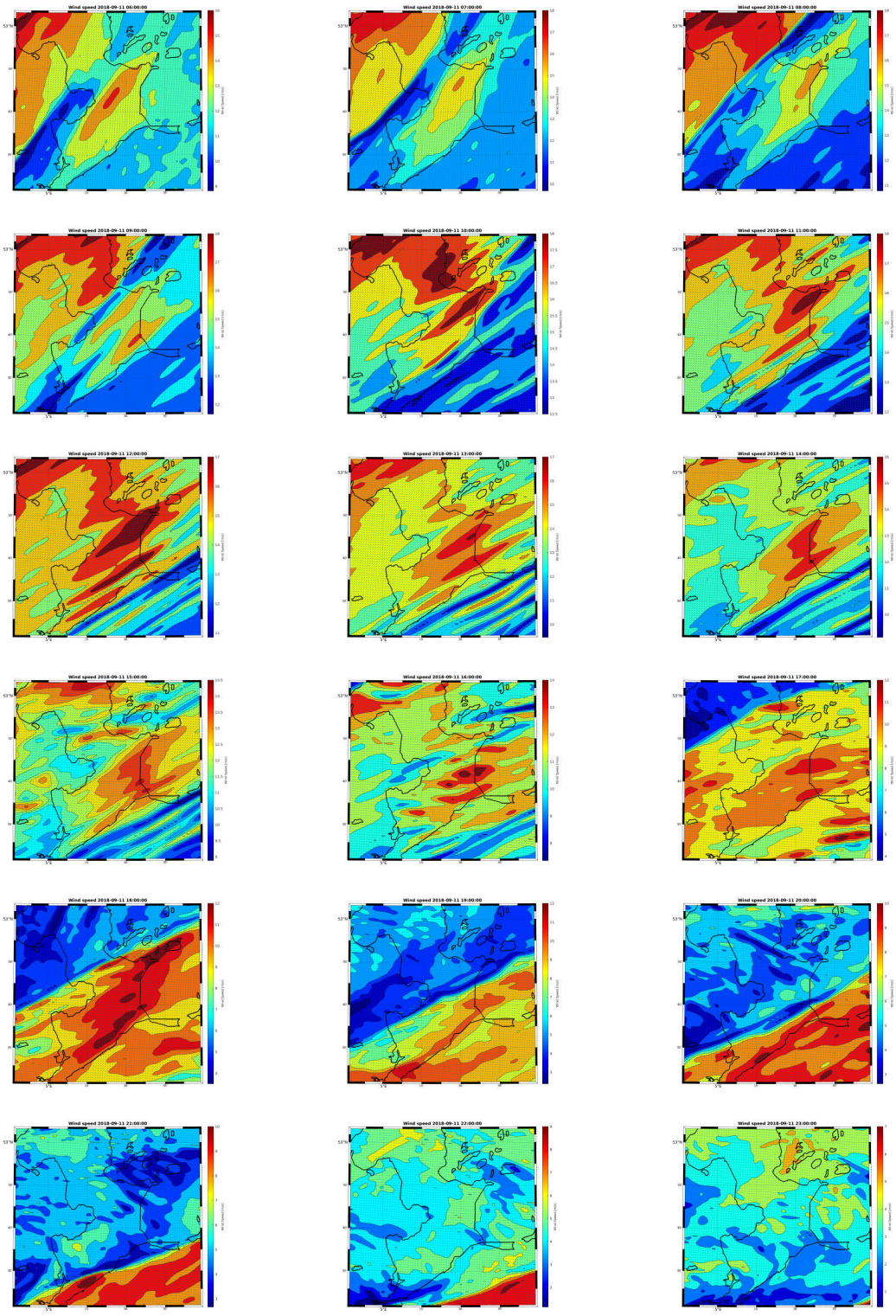

Figure A.19: WRF simulated wind speed around the hub height for flow case 2018-09-11 from 6:00 UTC to 23:00 UTC

A.4.3. Flow case 2018-10-11

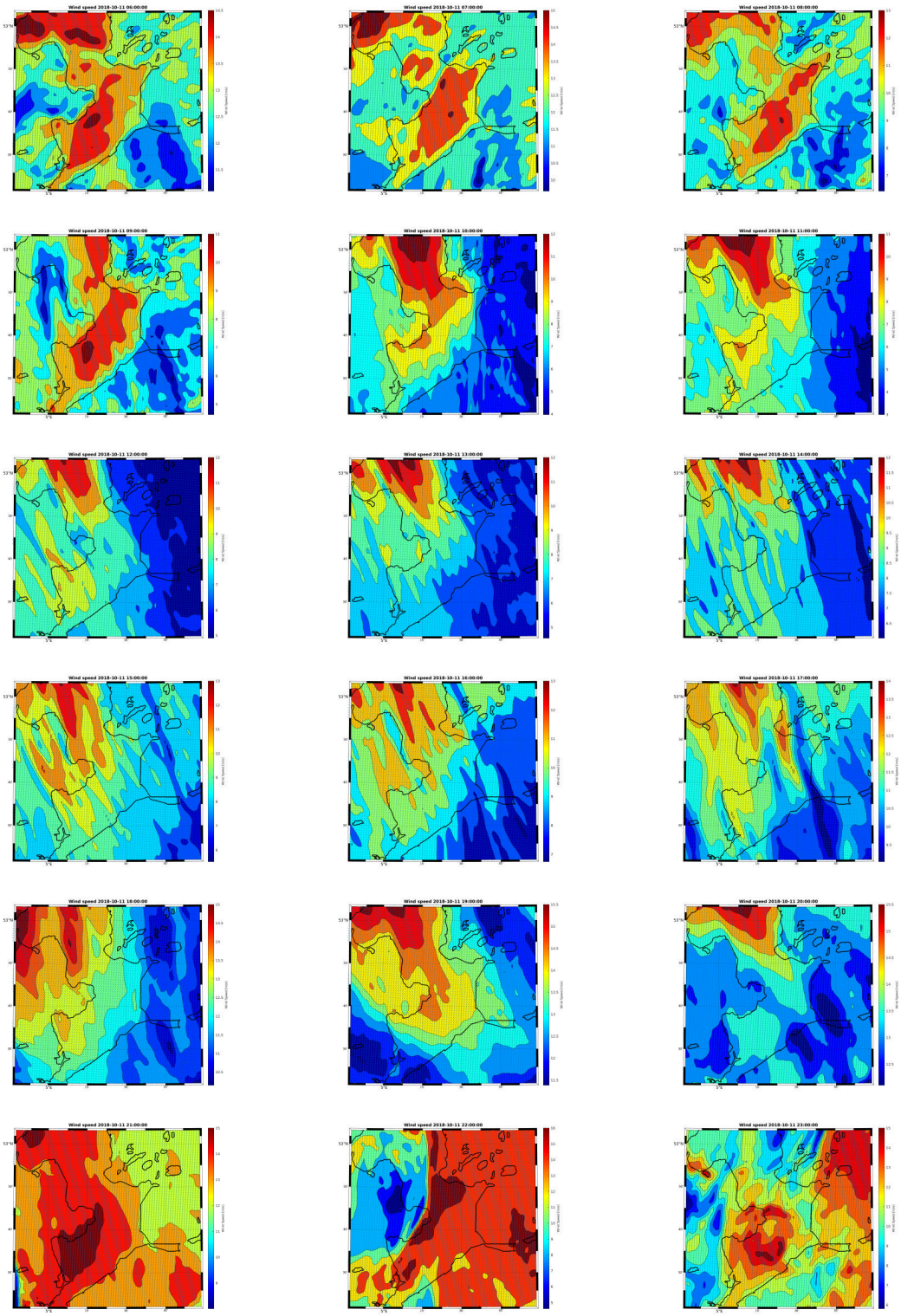

Figure A.20: WRF simulated wind speed around the hub height for flow case 2018-10-11 from 6:00 UTC to 23:00 UTC

A.4.4. Flow case 2018-11-30

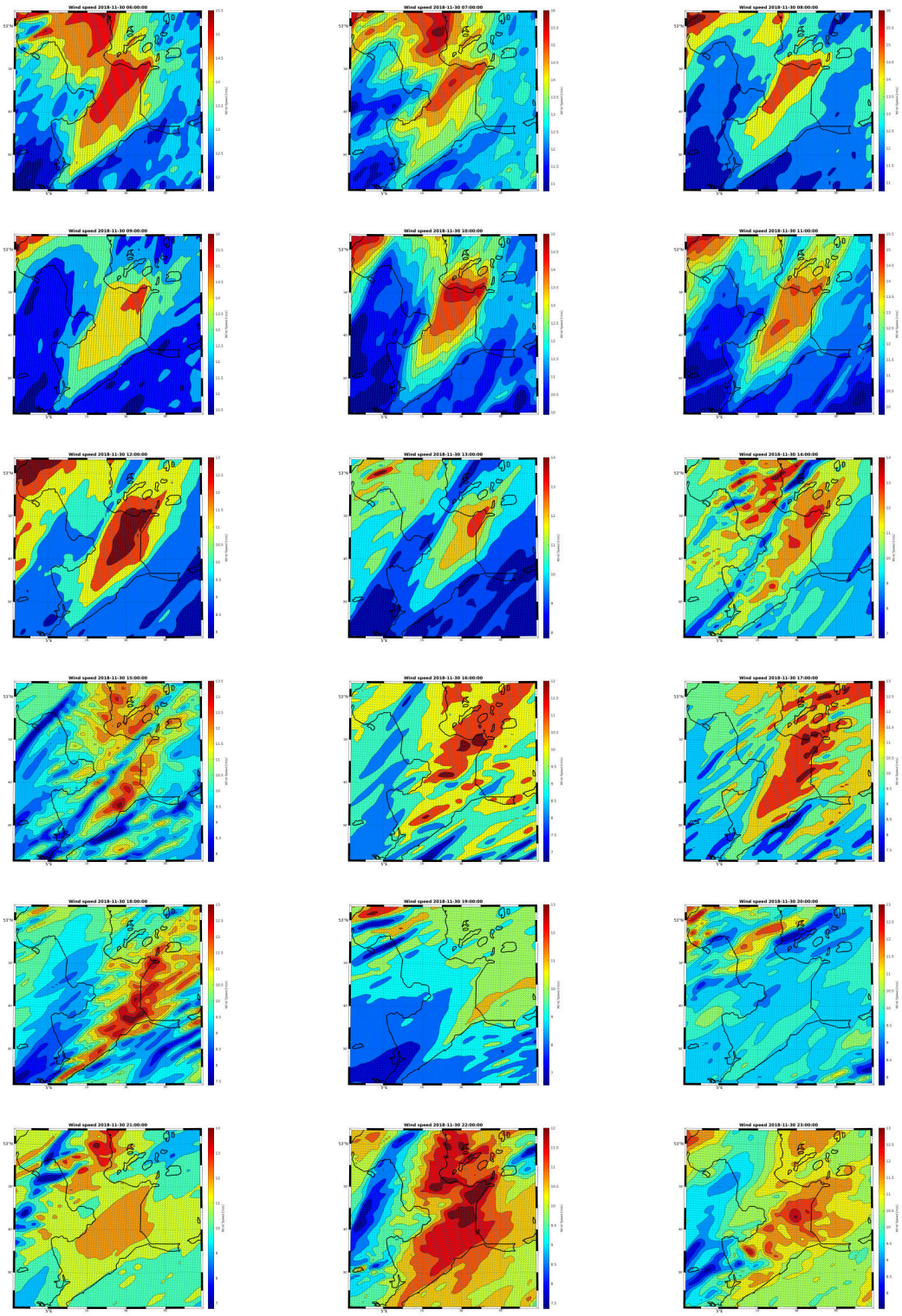

Figure A.21: WRF simulated wind speed around the hub height for flow case 2018-11-30 from 6:00 UTC to 23:00 UTC

A.4.5. Flow case 2018-12-10

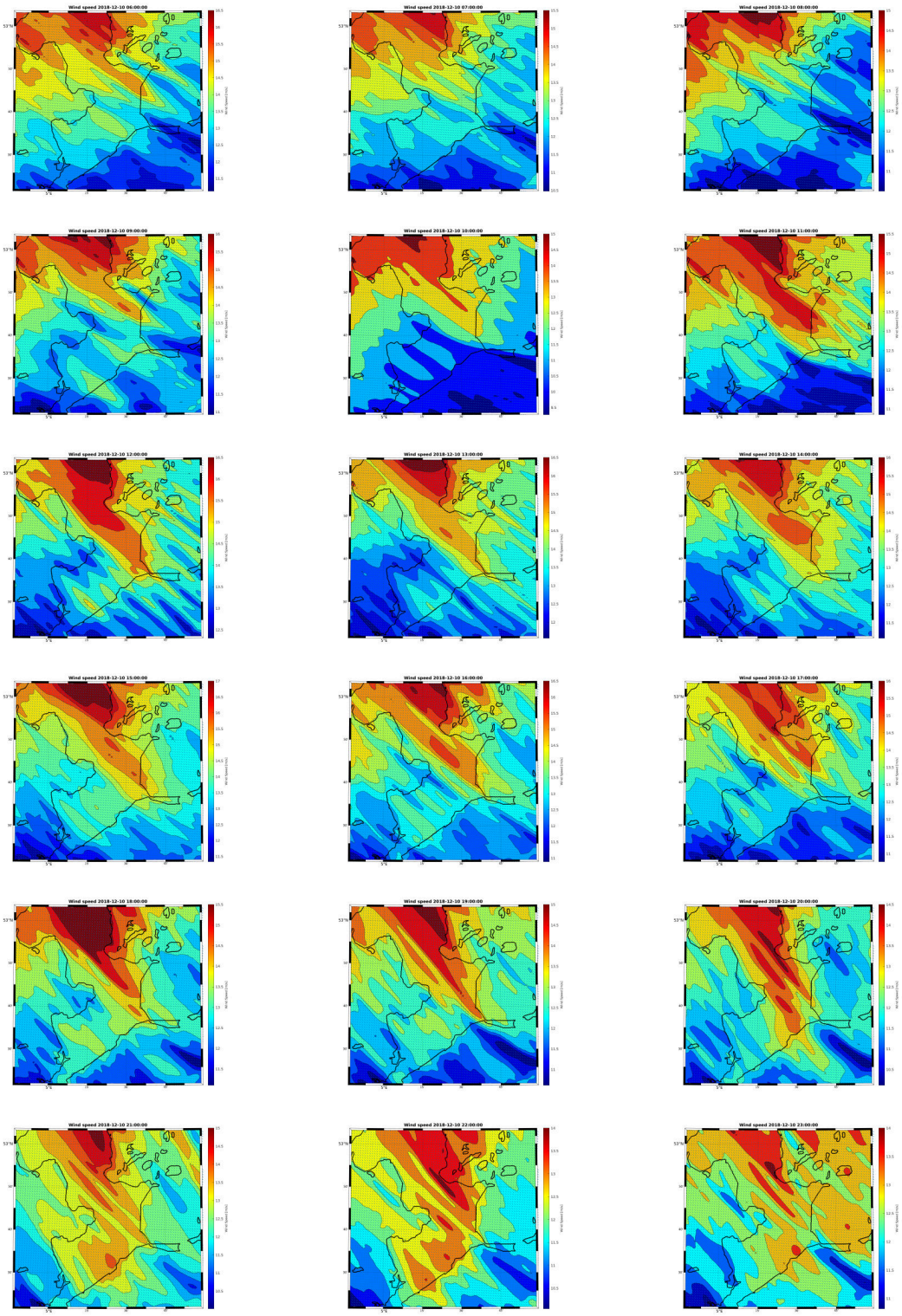

Figure A.22: WRF simulated wind speed around the hub height for flow case 2018-12-10 from 6:00 UTC to 23:00 UTC

A.4.6. Flow case 2018-12-26

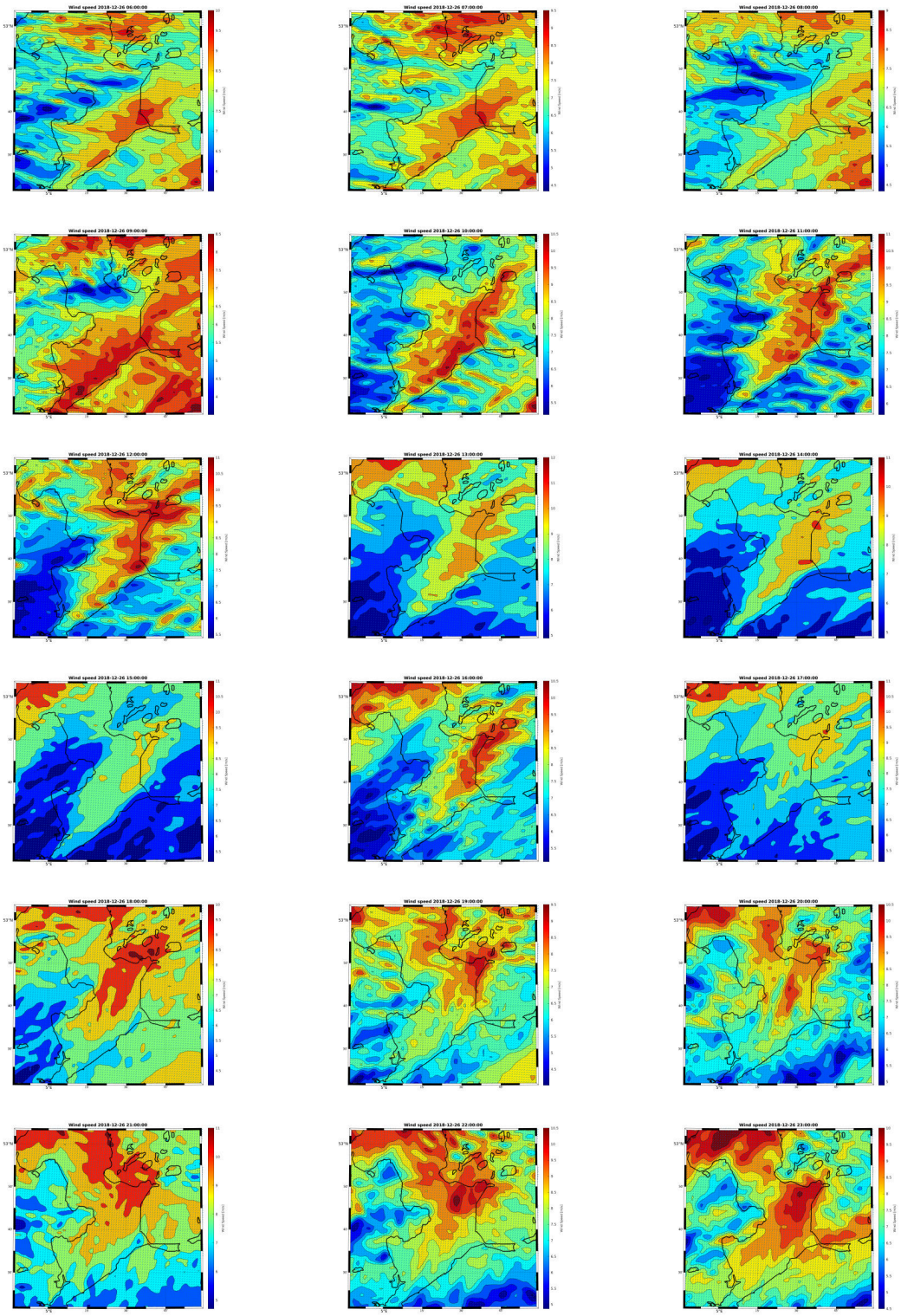

Figure A.23: WRF simulated wind speed around the hub height for flow case 2018-12-26 from 6:00 UTC to 23:00 UTC